Advanced Take-off and Flight Control Algorithms for Fixed Wing Unmanned Aerial Vehicles

by

Ruan Dirk de Hart

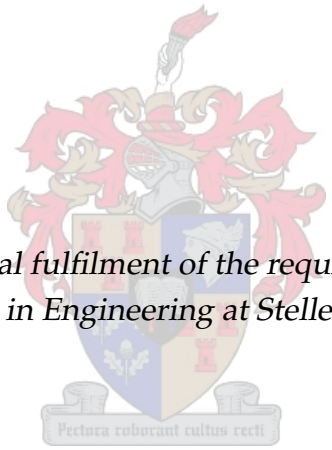

Thesis presented in partial fulfilment of the requirements for the degree of Master of Science in Engineering at Stellenbosch University

Supervisor: Dr. Iain K. Peddle

Department of Electrical and Electronic Engineering

March 2010

Declaration

By submitting this thesis electronically, I declare that the entirety of the work contained therein is my own, original work, that I am the owner of the copyright thereof (unless to the extent explicitly otherwise stated) and that I have not previously in its entirety or in part submitted it for obtaining any qualification.

March 2010

Abstract

This thesis presents the development and implementation of a position based kinematic guidance system, the derivation and testing of a Dynamic Pursuit Navigation algorithm and a thorough analysis of an aircraft's runway interactions, which is used to implement automated take-off of a fixed wing UAV.

The analysis of the runway is focussed on the aircraft's lateral modes. Undercarriage and aerodynamic effects are first analysed individually, after which the combined system is analysed. The various types of feedback control are investigated and the best solution suggested. Supporting controllers are designed and combined to successfully implement autonomous take-off, with acceleration based guidance.

A computationally efficient position based kinematic guidance architecture is designed and implemented that allows a large percentage of the flight envelope to be utilised. An airspeed controller that allows for aggressive flight is designed and implemented by applying Feedback Linearisation techniques.

A Dynamic Pursuit Navigation algorithm is derived that allows following of a moving ground based object at a constant distance (radius). This algorithm is implemented and verified through non-linear simulation.

Opsomming

Hierdie tesis handel oor die ontwikkeling en toepassing van posisie-afhanklike, kinematiese leidings-algoritmes, die ontwikkeling van 'n Dinamiese Volgings-navigasie-algoritme en 'n deeglike analise van die interaksie van 'n lugraam met 'n aanloopbaan sodat outonome opstygprosedure van 'n vastevlerk vliegtuig bewerkstellig kan word.

Die bogenoemde analise het gefokus op die laterale modus van 'n vastevlerk vliegtuig en is tweeledig behartig. Die eerste gedeelte het gefokus op die analise van die onderstel, terwyl die lugraam en die aerodinamiese effekte in die tweede gedeelte ondersoek is. Verskillende tipes terugvoerbeheer vir die outonome opstygprosedure is ondersoek om die mees geskikte tegniek te bepaal. Addisionele beheerders, wat deur die versnellingsbeheer gebaseerde opstygprosedure benodig word, is ontwerp.

'n Posisie gebaseerde kinematiese leidingsbeheerstruktuur om 'n groot persentasie van die vlugvermoë te benut, is ontwikkel. Terugvoer linearisering is toegepas om 'n lugspoedbeheerder , wat in staat is tot aggressiewe vlug, te ontwerp.

'n Dinamiese Volgingsnavigasie-algoritme wat in staat is om 'n bewegende grondvoorwerp te volg, is ontwikkel. Hierdie algoritme is geïmplementeer en bevestig deur nie-lineêre simulasie.

Acknowledgements

The author would like to thank the following people for their contribution towards this project.

- The Lord for His inspiration and guidance during this research.
- My parents for their love and support.
- Dr. Iain Peddle for his guidance, support during this research and always being available. Without his insights, this research would not have progressed to this level.
- Armscor for funding the project.
- Deon Blaauw for his support, insights and friendship.
- Bernard Visser for his work ethic that made our collaboration an enjoyable experience.
- AM "Abel" de Jager for his help during testing, proof reading of this document and his friendship.
- Chris "Kree" Jaquet for being a great sounding board and friend.
- Marcel "Muscle-man" Basson and Wihan "Conan" Pietersen for their help during testing.
- Michael Basson being available as a test pilot.

Contents

Nomenclature

Physical:

b	Wing Span
c	Mean Aerodynamic Chord
S	Surface Area
A	Aspect Ratio
e	Efficiency
m	Mass
I_{xx}	Moment of Inertia around roll axis
I_{yy}	Moment of Inertia around pitch axis
I_{zz}	Moment of Inertia around yaw axis
l_L	Undercarriage total length
l_w	Undercarriage total width
l_s	Axial distance from CG to steering wheel
l_m	Axial distance from CG to centre of main wheels
l_l	Lateral distance from CG to left wheel
l_r	Lateral distance from CG to right wheel

Natural Constants:

ρ	Air Pressure
g	Gravitational Acceleration

Aerodynamic:

q	Dynamic Pressure
C_L	Aerodynamic Lift Coefficient
C_D	Aerodynamic Drag Coefficient
C_l	Aerodynamic Roll Coefficient
C_m	Aerodynamic Pitch Coefficient
C_n	Aerodynamic Yaw Coefficient
C_x	Aerodynamic Axial Force Coefficient

C_y	Aerodynamic Lateral Force Coefficient
C_z	Aerodynamic Normal Force Coefficient

Position and Orientation:

N	North Position
E	East Position
D	Down Position
x	x-axis displacement
y	y-axis displacement
z	z-axis displacement
ϕ,θ,ψ	Euler Angles
$\boldsymbol{i}$,$\boldsymbol{j}$,$\boldsymbol{k}$	Basis Vectors

Velocity and Rotation:

$\overline{V}$	Velocity Vector
U	Axial Velocity
V	Lateral Velocity
W	Normal Velocity
ω	Angular Velocity
P	Roll Rate
Q	Pitch Rate
R	Yaw Rate

Forces, Moments and Accelerations:

L	Roll Moment
M	Pitch Moment
N	Yaw Moment
X	Axial Force
Y	Lateral Force
Z	Normal Force
A	Axial Specific Acceleration
B	Lateral Specific Acceleration
C	Normal Specific Acceleration
a_x	Axial Acceleration along the x-axis
a_y	Lateral Acceleration along the y-axis
a_z	Normal Acceleration along the z-axis

Actuation:

T_C	Thrust Command
T	Thrust State
τ_T	Thrust Time Constant
δ_E	Elevator Deflection
δ_A	Aileron Deflection
δ_R	Rudder Deflection
δ_S	Steering wheel Deflection
δ_{Run}	Runway Virtual Actuator Deflection

System:

A	Continuous System Matrix
B	Continuous Input Matrix
C	Output Matrix
D	Feedforward Matrix
ω	System frequency
ζ	System damping

Subscripts:

B	Coordinated in Body Axes
E	Coordinated in Earth Axes
W	Coordinated in Wind Axes
S	Coordinated in Stability Axes
G	Gravitational force or acceleration
g	Measurement relative to ground
T	Coordinated in Trajectory Axes
t	Related to the tyre
s	Related to the steering wheel
m	Related to the main wheels
l	Related to the left wheel
r	Related to the right wheel

Superscripts:

BI	Body relative to Inertial
WI	Wind relative to Inertial

Take-off related:

α	Wheel Side Slip
γ	Wheel Camber
μ_f	Coefficient of kinetic friction
$\overline{V}_g$	Groundspeed
N	Normal Force
N'	Aligning Moment

Flight related:

α	Angle of Attack
β	Angle of Side slip
$\overline{V}_a$	Airspeed

Dynamic Pursuit Navigation:

N_a	Aircraft North Displacement on the Tracking axis
E_a	Aircraft East Displacement on the Tracking axis
N_t	Desired Aircraft North Displacement on the Tracking axis
E_t	Desired Aircraft East Displacement on the Tracking axis
ψ_a	Heading from the aircraft to the desired point on the Tracking axis
ψ_A	Heading of the required acceleration vector
ψ_t	Heading from the object to the desired point on the Tracking axis
$\overline{V}_O$	Object's velocity

Acronyms:

CG	Aircraft Centre of Gravity
DCM	Direction Cosine Matrix
ESL	Electronic Systems Laboratory
UAV	Unmanned Aerial Vehicle
ATOL	Automatic Take-Off and Landing
VTOL	Vertical Take-Off and Landing
IMU	Inertial Measurement Unit
GPS	Global Positioning System
OBC	OnBoard Computer
CG	Centre of Gravity
DOF	Degree Of Freedom
EOM	Equations Of Motion
PI	Proportional Integral
MIMO	Multi Input Multi Output
SIMO	Single Input Multi Output
2D	Two Dimensional
3D	Three Dimensional
TSS	Time-Scale Separation
PKG	Position based Kinematic Guidance

List of Figures

List of Tables

Chapter 1

Introduction

Unmanned Aerial Vehicles (UAVs) are currently one of the main research fields in aeronautics, as they have certain advantages above piloted- or remotely controlled vehicles. UAVs are able to achieve precision flight for long periods of time without being affected by factors such as pilot fatigue and visibility. The costs of UAVs are also much less than piloted aircraft.

However, the human element cannot yet by excluded as humans have the ability to make split second decisions while taking a multitude of factors into consideration. Unlike UAVs, humans also have the ability to determine the correct course of action by analysing factors that are not necessarily related to the specific flight mission.

The future goal for UAVs is to form part of a larger system. The flight control and guidance would be autonomous and humans would only interact by making mission critical decisions. This would eliminate the use of pilots for all missions. These would include transport, air combat and commercial applications. Since UAVs cannot yet accomplish all these goals, they are currently best suited to surveillance missions.

The aim of the UAV group in the Electronic Systems Laboratory (ESL) at Stellenbosch University is to further UAV research to push the boundaries of unmanned flight. Before that could be accomplished, a foundation of basic flight controllers for fixed wing aircraft had to be laid down. Previous research such as autonomous Take-off and landing (ATOL) [11, 12], basic flight control with Waypoint navigation [13], aerobatic flight [18] and hover control for vertical Take-off and landing (VTOL) [26] have succeeded in creating this foundation. This has led to more advanced flight control which include the expansion of the flight envelope of UAVs [19], allowing the aerodynamic optimisation of airframes by eliminating stability criteria [24], precision landing [25] and improving flight safety through stall prevention [27].

This thesis has two main objectives that are largely unrelated, but both are aimed at expanding the UAV knowledge base at the ESL. These are autonomous Take-off and Waypoint- and Dynamic Pursuit Navigation of a fixed wing UAV with a tricycle undercarriage.

1.1 Focus of this research

1.1.1 Take-off

In order to further UAV research into a fully autonomous system, Take-off and landing must be automated. ATOL of an UAV is not new to the ESL and basic groundwork has been laid by [11] and [12]. The aim of that research was a practical, low cost solution to the ATOL problem. The motion of the aircraft while on the runway (including both aerodynamic and undercarriage interactions) was not analysed in detail, but rather a simple and robust solution was sought.

It was felt that more insight was required into the dynamics of fixed wing aircraft while on the ground. This insight could be used to determine the most suitable type of control for Take-off. This is thus the main focus of the Take-off part of this thesis.

1.1.2 Waypoint- and Dynamic Pursuit Navigation

At the time of this research, the guidance controllers that have been developed at the ESL to allow for basic guidance (limiting the flight envelope) or complicated 3D aggressive manoeuvres (full use of the flight envelope, but computationally inefficient). An intermediate level of guidance control is desired that allows for computational efficient guidance while utilising more of the flight envelope (large bank angles and high g manoeuvres). This guidance control should be capable of being used for Waypoint navigation and the application of more complicated algorithms, such as Dynamic Pursuit Navigation.

As UAVs are well suited for use as surveillance platforms, they are usually fitted with a camera which allows a remote user to gain visual information about the surrounding environment and increase situational awareness. Such UAVs are currently being used to perform a variety of surveillance tasks, which include land surveys and patrolling of borders or coastlines. During these surveillance missions, there are situations when a vehicle, person or object is spotted and needs to be inspected or followed. Since this is not a preplanned objective, the navigation needs to be implemented while in flight with limited information about the object. This is called Dynamic Pursuit Navigation and allows the onboard camera has to be positioned relative to the object by using real-time data to enable an unobstructed line of sight.

This part of the thesis focusses on the development of the intermediate guidance control and a Dynamic Pursuit Navigation algorithm.

1.2 Thesis layout

1.2.1 Take-off layout

The Take-off section begins with the system design in Chapter 2. An overview will be presented of the requirements and procedures that need to be completed to fulfil Take-off. A description of the required controllers will then be outlined.

Chapter 3 defines all the descriptions required to describe the aircraft's attitude and motion. The aircraft's interaction with the runway and atmosphere is also analysed to produce a full non-linear model of the aircraft on the runway.

The Take-off controller design is split into two chapters. Chapter 4 designs all the aerodynamic Take-off controllers. The lateral motion is linearised, analysed and the controllers are designed in Chapter 5.

All these controllers are then combined and tested in a complete non-linear simulation. The results of these simulations are shown in Chapter 6. This concludes the Take-off section.

1.2.2 Waypoint- and Dynamic Pursuit Navigation layout

Once Take-off is completed flight control will be discussed. Chapter 7 describes the system design required for Waypoint- and Dynamic Pursuit Navigation, in which an overview of the control strategy and controllers will be given.

The model for the aircraft in flight is not explicitly derived, instead the model designed by [14] is used and summarised in Chapter 8.

Chapter 9 discusses the design of the flight stability (innerloop) controllers, with the focus being on the airspeed and roll controllers. The other modes are controlled by [14]'s controllers, as they are sufficient.

A new set of guidance (outerloop) controllers are designed in Chapter 10 that allow more of the aircraft's flight envelope to be used, without requiring overly complicated calculations. All these controllers are then combined to create a flight guidance system.

The waypoint- and Dynamic Pursuit Navigation algorithms are developed in Chapter 11. This allows the UAV to fly between specified waypoints and follow moving surface objects[1]. This system is then tested in a full non-linear simulation and the results are shown in Chapter 12. This concludes the second section of this thesis.

A summary of the results of the Take-off analysis and controllers, and Dynamic Pursuit Navigation algorithm is given in Chapter 13. Any recommendations for future research are also made here.

1.3 Hardware

To enable the implementation of this research, a hardware platform is required. A new airframe and a digital avionics pack, previously designed at the ESL, was selected for this purpose.

1.3.1 Airframe

Since this research is aimed at fixed wing UAV research, a suitable airframe is required. A Super Frontier Senior 46 trainer aircraft was used as the application airframe. This airframe was shared with another masters research project [25] and had to conform to the requirements

[1] Objects that travel on the surface of the earth

of both projects. It was chosen since it has a low wing loading[2], sufficient space to build in the avionics and is configurable into two different undercarriage configurations.

Figure 1.1: Photograph of the airframe used in this research

1.3.2 Avionics

A digital electronic avionics pack was required as it allows for flexibility in the implementation of the control strategies. The avionics used has been developed in the ESL which includes an Inertial Measurement Unit (IMU), low cost GPS, pressure sensors and a magnetometer. A PC-104 based PC with a 300 MHz Celeron CPU was used as the Onboard Computer (OBC).

1.4 Simulation

In order to minimise risk to the aircraft, extensive Hardware In the Loop (HIL) simulations were run to ensure the satisfactory operation of the system. These simulations use the flight ready avionics and connects it to a simulation environment that emulates the motion of the physical airframe and sends dummy sensor data to the avionics. Since the avionics cannot tell the difference between real and dummy data, this test emulates actual flight with a high degree of accuracy. The HIL simulation that was used has been developed in the ESL in Simulink (as part of the MATLAB® software package).

[2] A ratio of aircraft mass to wing surface area.

1.5 Thesis goals

In summary, the goals of this thesis are,

- Analise the interactions of the aircraft while on the runway to gain detailed insight into the dynamics.
- Use this analysis to determine what type of control is best suited for Take-off.
- Design controllers that enable automated Take-off.
- Simulate these controllers to determine their effectiveness.
- Design new innerloop controllers that are applicable to the new guidance architecture (airspeed and roll controllers).
- Design a new guidance architecture that utilises more of the flight envelope, while keeping the computational demand low and allows the implementation of navigation algorithms.
- Develop an algorithm that allows a moving surface object to be followed with no previous information about its motion (Dynamic Pursuit Navigation).
- Test the controllers and algorithms in a non-linear simulation environment.
- Practically test the working of all the controllers (Take-off and flight) and algorithms (Waypoint- and Dynamic Pursuit Navigation).

Part I

Take-off

Chapter 2

Take-off System Design

Before the Take-off controllers are designed, it is necessary to define Take-off. Take-off is the procedure used to get an aircraft airborne from a stationary position. For the purpose of controller design, the Take-off procedure has to be simplified into phases which allow one set of controllers to be used for each phase.

2.1 Phases of Take-off

The general phases of Take-off have been defined in [11] as follows. The acceleration of the aircraft from a stationary position up to rotation speed[1] ($\overline{V}_r$) is defined as the Groundroll phase. Once $\overline{V}_r$ is reached, the aircraft must become airborne by rotating[2]. This is called the Rotation phase. Once the aircraft is airborne it must gain altitude as fast as possible without stalling[3], which is called the Climb out phase.

2.1.1 Phases of control used by [11]

Additional phases were added for control by [11], as the avionics used put certain constraints on the available measurements. Five phases were used, with the Groundroll phase being split into three. Phase 1 starts by placing the aircraft in the centre of the runway, facing along its length in the direction of Take-off. A low groundspeed is regulated until a valid GPS heading is measured, after which phase 2 is entered.

Phase 2 is used to guide the aircraft down the runway and when it is lined up[4], phase 3 is entered. In phase 3 the aircraft accelerates up to $\overline{V}_r$. Phases 1 to 3 are all part of the Groundroll phase.

Once $\overline{V}_r$ is reached, phase 4 is entered. Phase 4 is the Rotation phase in which the aircraft increases pitch to generate sufficient lift to become airborne. The Rotation phase is considered complete when the aircraft is more that 5m above the runway. The Climb out phase (phase 5) is then entered and continues until the aircraft is 30m above the runway. Take-off is then considered complete.

[1] The airspeed at which the aircraft can generate enough lift to safely depart the runway into flight.
[2] Increasing the aircraft's lift to allow it to depart the runway.
[3] Linear airflow over the lifting surface is disrupted and does not produce sufficient lift.
[4] The aircraft is centred width wise along the runway and pointing down the length of the runway

2.1.2 Phases used in this research

A kinematic state estimator was used to obtain accurate heading measurements while stationary. The use of phase 1 is thus not necessary. The other four phases are used as defined, but renamed as starting at phase 2 is confusing.

Phase 2 is renamed as the Taxi phase. Phase 3 is called the Acceleration phase, in which the maximum thrust is to be used to ensure the shortest Groundroll to reach $\overline{V}_r$. Phase 4 and 5 are called by their general description of Rotation and Climb out phases respectively. Figure 2.1 shows a comparison of the general phases, those used by [11] and this thesis.

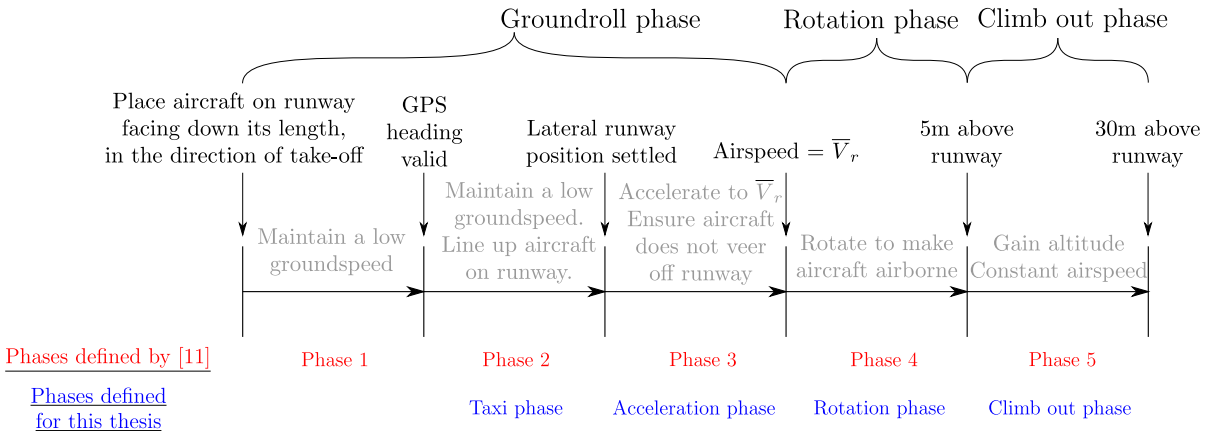

Figure 2.1: Graphical depiction of Take-off phases

2.2 Control required during Take-off phases

The control strategies are dependant on the motion of the aircraft during each phase, during Take-off. The motion during each phase will be analysed and used as the base for the control strategy.

2.2.1 Strategies

Taxi phase

At low speeds the aircraft's body does not pitch or roll, unless there is an external disturbance present (eg: wind). It is thus assumed that all the tyres remain in contract with the runway at all times. This simplifies motion during the Taxi phase into two modes, namely axial (forward body motion) and lateral (changing of the aircraft's heading). Thrust created by the engine is designed to change the aircraft's axial motion. The steering wheel is designed to change the aircraft's heading while on the runway.

Thrust will be used to ensure the aircraft maintains low ground speeds (groundspeed controller). The steering wheel is used to control the aircraft's lateral motion on the runway so that it is lined up correctly for the Acceleration phase (lateral controller). Since all the other actuators require sufficient airflow to be effective they will not be used at this low speed.

Acceleration phase

When the aircraft accelerates to $\overline{V}_r$ the same modes of motion are present as in the Taxi phase. The difference is that the aircraft starts producing lift, which decreases the restoring moments of the undercarriage. It is possible that a wind gust would be able to cause the undercarriage to lose contract with the runway, by pitching or rolling the aircraft. It is thus important that these disturbances be actively rejected.

Maximum thrust will be applied to ensure the shortest ground roll[5]. Lateral motion is still regulated by the steering wheel, but the increase of airspeed will increase the effectiveness of the rudder. The combined use of the steering wheel and rudder to control the lateral motion will thus be investigated. Wind disturbances will be actively rejected by the elevator and aileron (pitch- and roll rate regulation), but in such a way as not to cause unwanted torque effects.

Rotation phase

Once $\overline{V}_r$ is reached the aircraft has to depart the runway. The aircraft is in contact with the runway for a very short time during this phase. The effects of the undercarriage can thus be ignored.

Maximum thrust remains to be applied to prevent a reduction in airspeed. The aircraft is rotated by using the elevator (pitch angle control), while keeping the wings level[6] (roll angle controller). The steering wheel is disabled since it will no longer make contact with the runway, while the rudder is used to prevent side slip (as it would in normal flight).

Climb out phase

During the Climb out phase the aircraft is fully airborne and is more related to flight control than Take-off, as it will rely fully on aerodynamic control to control its motion. Simplified flight control can thus be applied to ensure sufficient altitude is gained.

In order to keep the separation between the two main sections (Take-off and navigation) in this thesis, the Climb out phase will not be discussed. It will rather be assumed that flight control is enabled during Climb out, with a specified airspeed and climb rate command.

Before any controllers can be designed, a model must be derived for Take-off which gives a mathematical description of the forces and moments that act on the aircraft.

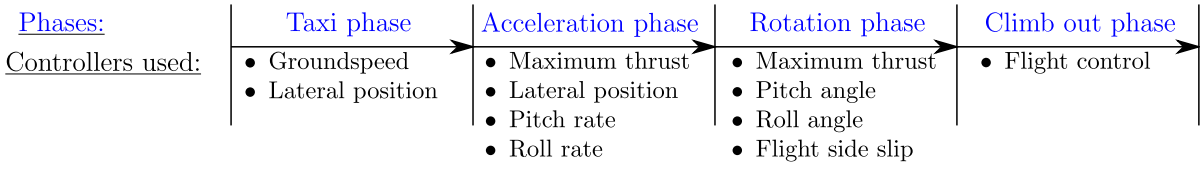

Figure 2.2: Controllers required during Take-off phases

[5]The distance travelled on the runway.
[6]Wings parallel to the horizon.

Figure 2.2 gives a summary of the controllers used in each phase of Take-off. The overall system construction is represented in block diagram form in Figure 2.3

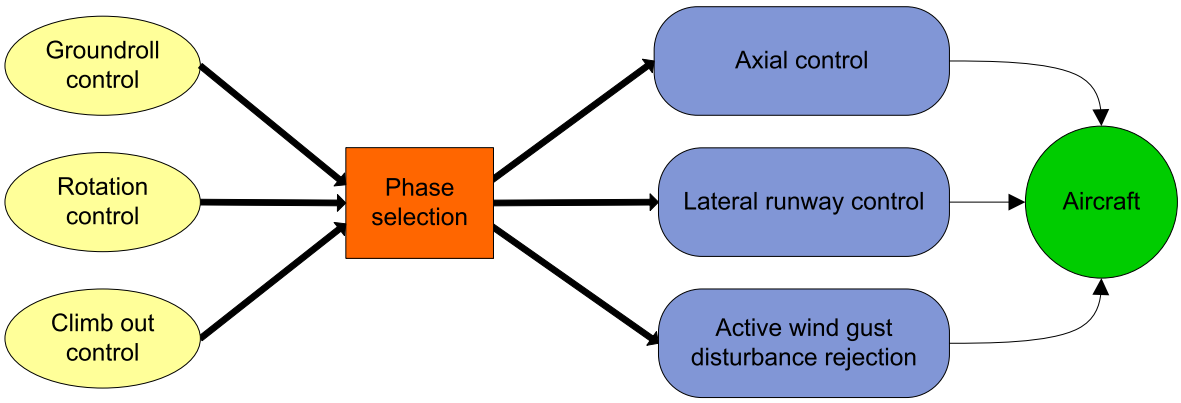

Figure 2.3: Overall Take-off system construction

2.3 Summary

It is now clear what type of controllers need to be implemented during Take-off. The specific controllers are designed in Chapter 4 and 5, after thorough analysis. But first the aircraft's model, while on the runway, needs be derived.

Chapter 3

Dynamic Runway Model

A mathematical description of the dynamic motion of the aircraft is required so that linear control techniques can be applied. Since the aircraft interacts with both the runway and atmosphere while on the runway, a combined model will be derived.

Every model requires a frame of reference relative to which the object is to be described. As a result, axis systems and attitude descriptions are defined in order to describe the position, motion and orientation of the aircraft. Using these descriptions, the interactions that cause undercarriage forces and moments are integrated with the aerodynamic forces and moments to produce the full non-linear model of the aircraft while on the runway (called the Runway model).

3.1 Axis, Attitude and Conventions

3.1.1 Body axis

To be able to describe motion and orientation of the aircraft we need to define an axis system. A right-handed orthogonal axis system is defined with its origin at the aircraft's centre of mass (also called the centre of gravity, CG) with the positive x-axis extending through the nose of the aircraft (parallel to the thrust line of the engine). The positive y-axis is defined along the starboard[1] main wing. Finally, the positive z-axis is defined down through the bottom of the aircraft.

The aircraft's body is assumed to be rigid. The Body axis thus stays fixed to the aircraft's body, with the position vector from any point on the aircraft to the centre of mass remaining unchanged over time. The xz_B-plane is usually a plane of symmetry for the aircraft. Throughout this thesis, all forces and moments are coordinated in Body axis unless specified otherwise.

[1] The right wing when looking from behind the aircraft

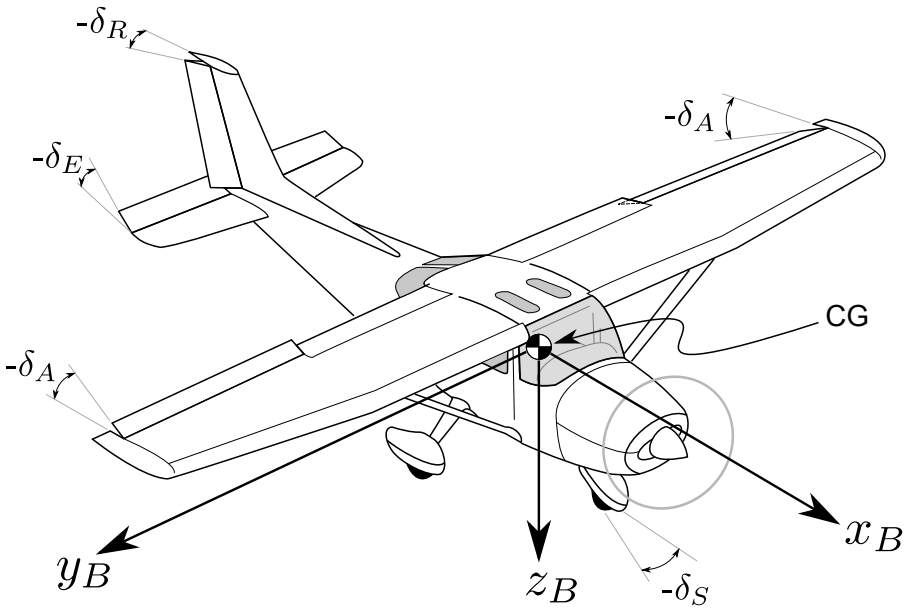

Figure 3.1: The Body axis

3.1.2 Stability axis

The Stability axis is a type of Body axis, that has been rotated about the y_B-axis by the body's angle of attack[2] (α). This causes the relative wind velocity vector ($\overline{V}_a$) to lie in the xz_B-plane and be aligned with the x_S-axis.

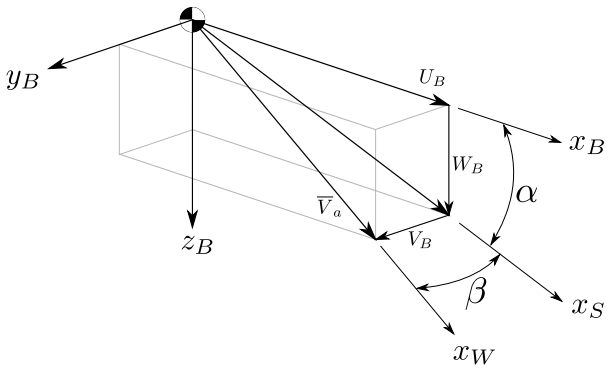

Figure 3.2: The Stability- and Wind axis

3.1.3 Wind axis

The Wind axis is a further extension of the Stability axis by rotating it about the z_S-axis through the side slip angle (β), so that the relative wind velocity vector is always aligned with the x_W-axis. Figure 3.2 shows the relationship between the Body-, Stability- and Wind axis systems.

[2] Angle between the x_B-axis and the velocity vector.

3.1.4 Earth axis

The aircraft's motion needs to be described with respect to a reference frame. All navigation is described with relation to the Earth. The distances that will be covered by this research are small enough to approximate the earth as a flat surface. Consequently the Earth axis is defined as a Cartesian right-handed orthogonal axis system with the origin at the centre of the Take-off runway. The positive x_E-axis points due north, the positive y_E-axis due east and the positive z_E-axis down toward the centre of the earth.

The earth is not inertially fixed as it is rotating in space. The Earth's rotation relative to space is very small compared to the rotations of the aircraft relative to the earth. As a result, it can be approximated that inertial rotations of the aircraft are the same as aircraft rotations and accelerations relative to the Earth, by ignoring the influence of the Earth's rotation.

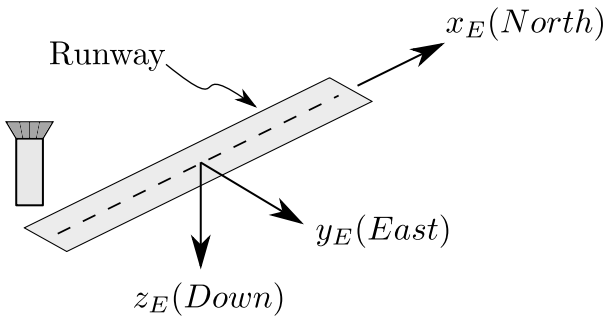

Figure 3.3: The Earth axis

3.1.5 Aircraft Notation and Sign Conventions

The notation used in aviation follows a consecutive alphabetical format, starting with the x-, y- and then z-axis. Body axis velocities are U (in the positive x_B-axis), V (y_B-axis) and W (z_B-axis). Rates of rotation are P, Q and R. Forces acting on the aircraft in the body axis are X, Y and Z, while moments are L, M and N. Actuator deflections are defined such that a negative deflection will cause a positive moment about an axis. The actuator convention is clearly visible in Figure 3.1.

3.1.6 Attitude Description

It is essential to be able to describe the orientation of the aircraft relative to the Earth axis. A number of descriptions exist, but Euler angles are used as they are intuitive and their singularities will not be a problem. Euler angles are defined as rotations about the Body axis, with the number describing the axis rotated about. 1 is Roll (ϕ) about the current x_B-axis, 2 is Pitch (θ) about the current y_B-axis and 3 is Yaw (ψ) about the current z_B-axis. A pictorial representation is shown in Figure 3.4.

Euler angles have a singularity at various attitudes, depending on the description. As this research is not aimed at aerobatic flight, the Euler 3-2-1 attitude description was used that has a singularity when the aircraft's x_B-axis lines up with the earth's z_E-axis (or $\pm 90°$ pitch). Euler

3-2-1 describes the aircraft's orientation relative to the earth by assuming initial orientation is aligned with the Earth axis, then rotating through the ψ, then θ and finally ϕ angle.

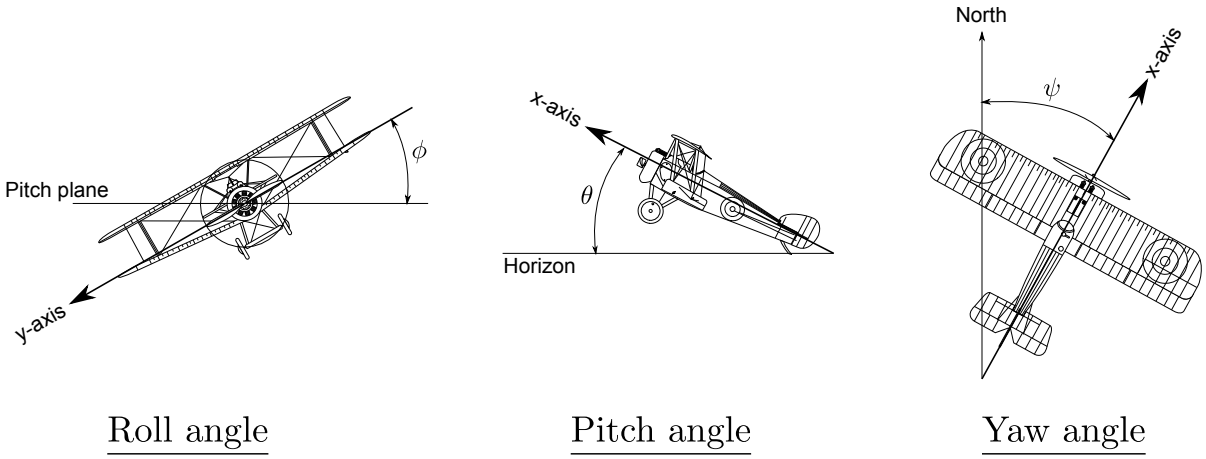

Figure 3.4: Euler attitude description angles (aircraft image courtesy of [29])

The Direction Cosine Matrix (DCM) [8] is defined such that vectors coordinated in one axis system can be coordinated in another (see appendix A). The DCM can be written using Euler angles and in the case where a vector from the Inertial axis has to be coordinated into the Body axis, the DCM^{BI} is used. Coordinating a Body axis vector into Inertial axis requires the inverse DCM, but because the DCM is orthogonal, $\left[DCM^{BI}\right]^{-1} = \left[DCM^{BI}\right]^{T}$ [13].

$$\boldsymbol{V}_B = \mathbf{DCM}^{BI}\boldsymbol{V}_I \tag{3.1.1}$$

$$\boldsymbol{V}_I = \left[\mathbf{DCM}^{BI}\right]^{T}\boldsymbol{V}_B \tag{3.1.2}$$

Since the attitude angles change, their dynamics (the rotational dynamics) need be described. They are described by Equation 3.1.3.

$$\begin{bmatrix}\dot{\phi}\\ \dot{\theta}\\ \dot{\psi}\end{bmatrix} = \begin{bmatrix}1 & \sin\phi\tan\theta & \cos\phi\tan\theta\\ 0 & \cos\phi & -\sin\phi\\ 0 & \sin\phi\sec\theta & \cos\phi\sec\theta\end{bmatrix}\begin{bmatrix}P\\ Q\\ R\end{bmatrix} \tag{3.1.3}$$

3.1.7 6 Degree of Freedom Equations of Motion

The 6-DOF EOM are derived in their scalar form in [13]. This form allows the body forces and moments to describe the motion of the aircraft. The 6-DOF EOM in Body axis can be written as,

$$\begin{aligned} \mathrm{X} &= m(\dot{U} + WQ - VR) \\ \mathrm{Y} &= m(\dot{V} + UR - WP) \\ \mathrm{Z} &= m(\dot{W} + VP - UQ) \end{aligned} \tag{3.1.4}$$

$$\begin{aligned} \mathrm{L} &= \dot{P}I_x - \dot{R}I_{xz} + QR\left(I_z - I_y\right) - PQI_{xz} \\ \mathrm{M} &= \dot{Q}I_y + PR\left(I_x - I_z\right) + \left(P^2 - R^2\right)I_{xz} \\ \mathrm{N} &= \dot{R}I_z - \dot{P}I_{xz} + PQ\left(I_y - I_x\right) + QRI_{xz} \end{aligned} \tag{3.1.5}$$

The relationship between force, acceleration, velocity and position are described below [14]. The position- and velocity vector dynamics, relative to inertial space, is shown in Equation 3.1.6.

$$\begin{aligned} \left.\frac{d}{dt}\mathbf{P}^{BI}\right|_I &= \mathbf{V}^{BI} \\ \left.\frac{d}{dt}\mathbf{V}^{BI}\right|_I &= \mathbf{A}^{BI} = \left.\frac{d}{dt}\mathbf{V}^{BI}\right|_B + \omega^{BI} \times \mathbf{V}^{BI} \end{aligned} \tag{3.1.6}$$

3.2 Undercarriage Forces and Moments

The undercarriage model gives a mathematical description of the aircraft's interactions with the runway. In order to produce this model, we need to first define the forces and moments that the undercarriage induce on the aircraft. These forces and moments are produced by the interaction between the tyres and the ground.

After defining an appropriate axis system for the tyre, these interactions are investigated. The forces and moments created by airflow are discussed in Section 3.3, which completes the non-linear Runway model.

3.2.1 Tyre axis

The origin of the Tyre axis (shown in Figure 3.5) is defined at the centre of contact between the tyre and the surface that it is on. The plane that the wheel rotates in, is called the Wheel plane. The x_t-axis is the intersection between the Wheel plane and the ground plane, with the positive being in the forward direction of wheel motion due to rotation. The z_t-axis is perpendicular to the ground plane and positive downward. The y_t-axis completes the right-hand orthogonal Tyre axis system and is perpendicular to the x_t-axis and parallel to any vector that lies in the ground plane.

Two angles are formed between the Wheel plane and the Tyre axis. The tyre slip angle (α_t) is the angle formed between the tyre's velocity vector ($\overline{V}_t$) and x_t-axis. The camber angle (γ_t)

is formed between the Wheel plane and negative z_t-axis. Tyre forces and moments are defined according to aviation convention. The forces and moments along the x_t-, y_t- and z_t-axis are X_t, Y_t and Z_t and L_t, M_t and N_t' respectively.

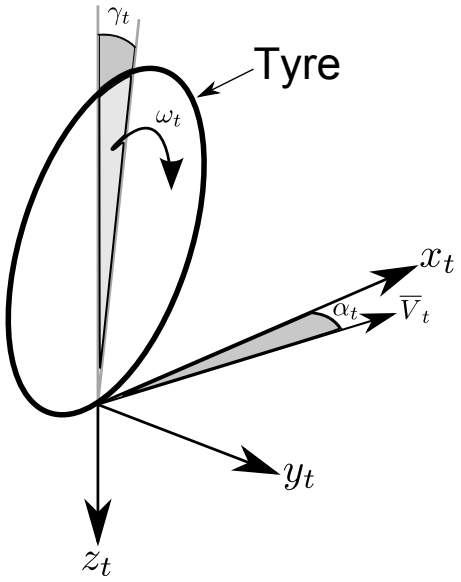

Figure 3.5: The Tyre axis

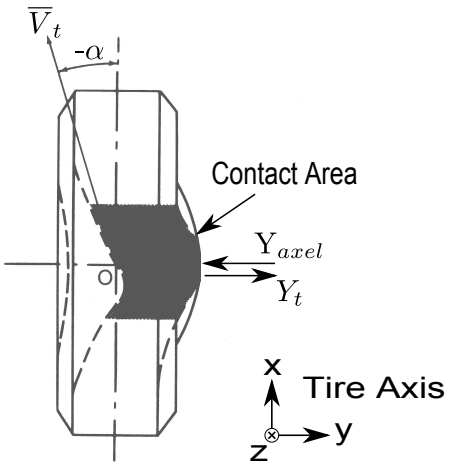

Figure 3.6: Tyre deformation due to slip angle [7]

3.2.2 Tyre Forces and Moments [7]

If we only consider the interaction between the tyre and ground, there are forces and moments that influence the motion of the tyre. These are Traction- (X_t), Lateral- (Y_t) and Normal forces (Z_t) as well as Overturning- (X_t), Rolling Resistance- (M_t) and Aligning moments (N_t').

Traction force is mainly caused by the deformation of the tyre carcass. This is a mechanical drag that does not affect the lateral dynamics of the tyre. Instead it only produces friction that inhibits forward motion on the runway. This force varies extensively with tyre type, -pressure and normal force, and is difficult to determine. Consequently it will be lumped with the kinetic friction variable (μ_f). Traction force is then,

$$X_t = -\mu_f N_t. \tag{3.2.1}$$

Lateral tyre force (Y_t) is a result of lateral tyre deformation (shown in Figure 3.6) and is caused by the tyre's camber- (γ_t) and slip angles (α_t). The contribution to lateral tyre force due to tyre camber is about five times smaller than that of tyre side slip for the same angle deflection [7]. As tyre camber is typically small (less than 1°) its effect can be ignored without adversely affecting the model. The contribution to lateral force due to slip angle is modelled well by the Foundation Stiffness Model [6] as a set of stretched out springs. Through extensive investigation is has been found that Y_t is linear as long as side slip is small (less that 4°) [7],

and the Cornering Stiffness (C_α) is defined to relate side slip (α_t) to lateral force (Y_t).

$$C_\alpha = \frac{\partial Y_t}{\partial \alpha_t} \quad [7] \tag{3.2.2}$$

Vertical load (or Normal force (N_t)) is the parameter that has the largest influence on the Cornering Stiffness of a tyre, which allows for the non-dimensionalising of C_α with respect to vertical load in the variable Cornering Coefficient ($C_{\alpha\alpha}$). Tyre pressure only has a moderate effect on Cornering Stiffness and does not change during the use of the tyre unless it is punctured, thus it is not included as a model parameter.

$$C_\alpha = C_{\alpha\alpha} N_t \tag{3.2.3}$$

Note that lateral force is negative for a positive side slip, thus C_α and $C_{\alpha\alpha}$ are negative per definition. Lateral force due to side slip is thus,

$$Y_t = C_{\alpha\alpha} N_t \alpha_t \tag{3.2.4}$$

Both Overturning- (L_t) and Rolling Resistance moments (M_t) have negligibly small or no effect on the dynamic lateral response of the tyre [7], and are also ignored. When the tyre deforms laterally, the lateral tyre force does not act on the centre of the tyre's contract area with the ground. The Aligning moment is formed between Y_t and the force that the undercarriage causes on the axle of the wheel (Y_{axel}). This moment is very small due to the short distance between Y_t and Y_{axel} (see Figure 3.6). Thus it is only considered when effort to steer the wheel is analysed.

Tyre slip angles

Each individual tyre will have its own local slip angle. Subscripts s, l and r relate to the steering-, left- and right wheels respectively. When viewing the undercarriage from above, as in Figure 3.7, the slip angles are calculated in equations 3.2.5.

$$\begin{aligned}
\alpha_s &= \arctan\left(\frac{V_s}{U_s}\right) = \arctan\left(\frac{V + l_s R}{U}\right) + \delta_s \\
\alpha_l &= \arctan\left(\frac{V_l}{U_l}\right) = \arctan\left(\frac{V - l_m R}{U + l_l R}\right) \\
\alpha_r &= \arctan\left(\frac{V_r}{U_r}\right) = \arctan\left(\frac{V - l_m R}{U - l_r R}\right)
\end{aligned} \tag{3.2.5}$$

Undercarriage Normal Forces

An aircraft's wheels are usually connected to the airframe with a spring and damper suspension system to increase passenger comfort. UAVs do not have to take passenger comfort into consideration and subsequently their undercarriage usually does not have suspension components in order to reduce complexity and weight. As there are no sensors that can measure the normal forces on the wheels and aircraft are generally parallel to the runway during Take-

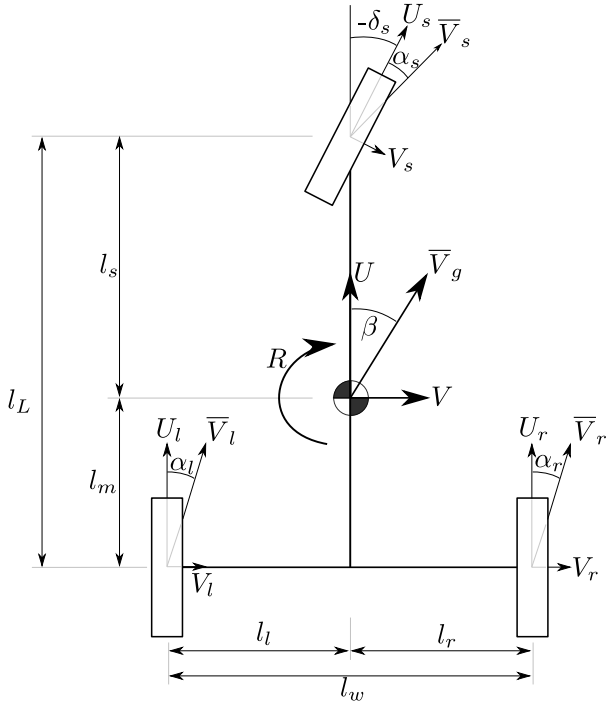

Figure 3.7: Undercarriage notation and slip angles

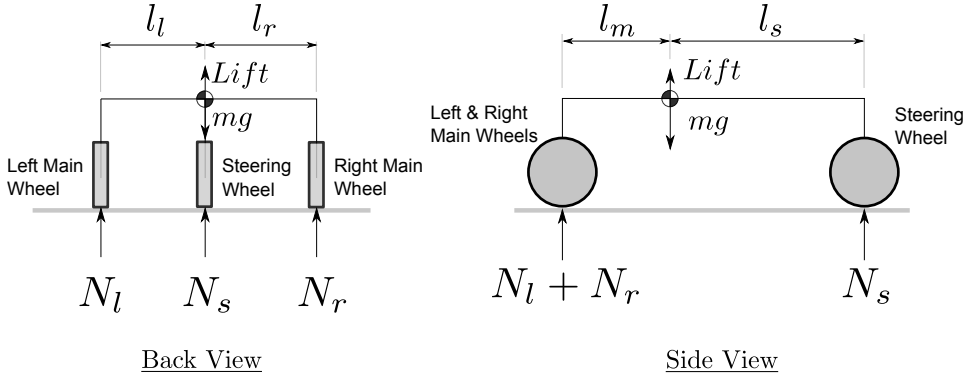

Figure 3.8: View from the back and side of the undercarriage depicting the normal forces

off, the normal forces are modelled as the mass that is evenly distributed.The total normal force will be represented by N. The magnitude of the normal forces on each individual wheel is then,

$$N_s = \frac{l_m}{l_L} N \tag{3.2.6}$$

$$N_l = \frac{l_s}{l_L}\frac{l_r}{l_w} N \tag{3.2.7}$$

$$N_r = \frac{l_s}{l_L}\frac{l_l}{l_w} N \tag{3.2.8}$$

Taking the height between the tyre's contact area and centre of mass into account, increases the model complexity but does not add to the fidelity of the model and is thus ignored [11].

The lateral force produced locally at each wheel (X_s, X_l and X_r) has an effect on the body,

which is both a force and a moment. The total undercarriage force vector in Body axis is,

$$\begin{bmatrix} X_U \\ Y_U \\ Z_U \end{bmatrix}_B = \begin{bmatrix} X_s \cos(-\delta_s) - Y_s \sin(-\delta_s) + X_l + X_r \\ X_s \sin(-\delta_s) + Y_s \cos(-\delta_s) + Y_l + Y_r \\ -N_s - N_l - N_r \end{bmatrix} \tag{3.2.9}$$

Each wheel creates a moment (L_s, M_l and N_r) as a result of a force acting over a distance. The total undercarriage moment vector in Body axis is,

$$\begin{aligned} \begin{bmatrix} L_U \\ M_U \\ N_U \end{bmatrix}_B &= \begin{bmatrix} L_s + L_l + L_r \\ M_s + M_l + M_r \\ N_s + N_l + N_r \end{bmatrix}_B \\ &= \begin{bmatrix} (0) + (-l_l Z_l) + (l_r Z_r) \\ (-l_s Z_s) + (l_m Z_l) + (l_m Z_r) \\ (l_s Y_s) + (l_l X_l - l_m Y_l) + (-l_r X_r - l_m Y_r) \end{bmatrix}_B \end{aligned} \tag{3.2.10}$$

3.3 Aerodynamic Forces and Moments [3]

Aircraft are designed to control their movement by using their aerodynamic surfaces to control the forces and moments that are generated on the body by its motion through the atmosphere. In [3] the model is described by analysing the aerodynamic forces and moments acting on the aircraft's body. This description is easier to incorporate with the Runway model.

The forces and moments created by the movement of the aircraft through the atmosphere are modelled in [3], and only stated here. These equations have been derived assuming a small angle of attack (α). The aerodynamic forces and moments (denoted with subscript a) are defined in Equation 3.3.1 by using non-dimensional aerodynamic coefficients coordinated in Stability axis.

$$\begin{aligned} X_a &= \bar{q}S\left(C_{X_S} - C_{Z_S}\alpha\right) \\ Y_a &= \bar{q}S\left(C_{Y_S}\right) \\ Z_a &= \bar{q}S\left(C_{Z_S} + C_{X_S}\alpha\right) \\ L_a &= \bar{q}Sb\left(C_{L_S} - C_{N_S}\alpha\right) \\ M_a &= \bar{q}Sc\left(C_{M_S}\right) \\ N_a &= \bar{q}Sb\left(C_{N_S} - C_{L_S}\alpha\right) \end{aligned} \tag{3.3.1}$$

The non-dimensional aerodynamic coefficients are defined by the use of stability- and control derivatives [1].

$$\begin{aligned} C_{X_S} &= -C_D \\ C_{Y_S} &= C_{y_\beta}\beta + \frac{b}{2\overline{V}_a}\left(C_{Y_p}P + C_{y_r}R\right) + C_{y_{\delta_A}}\delta_A + C_{y_{\delta_R}}\delta_R \\ C_{Z_S} &= -C_L \\ C_{L_S} &= C_{l_\beta}\beta + \frac{b}{2\overline{V}_a}\left(C_{l_p}P + C_{l_r}R\right) + C_{l_{\delta_A}}\delta_A + C_{l_{\delta_R}}\delta_R \\ C_{M_S} &= C_{m_\alpha}\alpha + \frac{c}{2\overline{V}_a}\left(C_{m_q}Q\right) + C_{m_{\delta_E}}\delta_E \\ C_{N_S} &= C_{n_\beta}\beta + \frac{b}{2\overline{V}_a}\left(C_{n_p}P + C_{n_r}R\right) + C_{n_{\delta_A}}\delta_A + C_{n_{\delta_R}}\delta_R \end{aligned} \tag{3.3.2}$$

with,

$$\begin{aligned} C_L &= C_{L_0} + C_{L_\alpha}\alpha + C_{L_q}Q + C_{L_{\delta_E}}\delta_E \\ C_D &= C_{D_0} + \frac{C_L^2}{\pi A e} \\ A &= \frac{b}{c} \end{aligned} \tag{3.3.3}$$

and,

$$\overline{q} = \frac{1}{2}\rho\overline{V}_a^2$$

3.4 Other Forces

3.4.1 Thrust

A methanol internal combustion engine is used for propulsion, which can be adequately modelled as a first order lag from commanded thrust (T_c) to actual thrust (T) [11, 18]. It is assumed that the thrust acts through the x_B-axis and the torque from the prop is small compared to the moment of inertia of the aircraft and the countering effect of the ailerons, allowing it to be ignored. The transfer function of the dynamic response of the engine is,

$$\frac{T}{T_c} = \frac{1}{\tau_T s + 1} \tag{3.4.1}$$

where τ_T is the engine time constant.

3.4.2 Gravity

Gravity always acts from an object's lumped centre of mass, to the centre of the earth and can be coordinated into the Body axis,

$$\begin{bmatrix} X_B \\ Y_B \\ Z_B \end{bmatrix} = \left[DCM^{BI}\right] \begin{bmatrix} 0 \\ 0 \\ mg \end{bmatrix}_E \tag{3.4.2}$$

$$\tag{3.4.3}$$

3.5 Summary

All the forces and moments that act on the aircraft while on the runway (undercarriage and aerodynamic) have been described. Combining these with the 6-DOF EOM produces the full non-linear Runway model, which is used for non-linear simulation. The controller designs in the following chapter, use this model as their plant.

Chapter 4

Take-off part 1: Aerodynamic Control

In the previous chapter the Runway model was derived. The focus of this chapter is to use this model to design linear controllers that can be used for Take-off.

Using the complete Runway model to design control systems is possible, but unnecessarily complicated. The Runway model can be simplified by analysing the coupling between different modes of motion, and should this coupling be sufficiently small, the modes can be assumed to be decoupled. This decreases the amount of differential equations for each controller and reduces complexity. The model is then linearised about a specified work point before control is applied.

A standard sequence for the design of each controller is used, which is:

- Decouple the model to reduce the DOF.
- Linearise the model.
- Design the controller.
- Show linear simulation results of the controller.

Certain assumptions are made throughout this chapter which simplifies the controller design. The effect of these simplifications will be tested when a full non-linear simulation is run and its results shown in Chapter 6. These assumptions are:

- No wind is present, thus airspeed is equal to groundspeed.
- The lateral velocity is much smaller than axial velocity.
- The xy_B-plane is parallel to the xy_E-plane.

Due to the amount of detail of the lateral runway controller, its analysis and design will be described in Chapter 5. All the other Take-off controllers are designed in this chapter.

Runway Modes of motion

Four modes of motion have been identified in Section 2.2. These are axial (along the x_B-axis), lateral (directional motion restricted to the xy_B-plane), pitch (rotation about the y_B-axis) and roll (rotation about the x_B-axis). The only mode of motion left is normal (along the z_B-axis).

If the tyres remain in contact with the runway, lift and gravity are the only two components that influence the normal force. The amount of lift is influenced by the airspeed and static incidence angle of the main wing.

4.1 Axial Runway Control

4.1.1 Decoupling

The mathematical model describing the axial motion can be derived from the 6-DOF EOM developed in Chapter 3. Assuming motion only along the x_B-axis, the axial EOM can be simplified to a 1-DOF dynamic model shown in Equation 4.1.1.

$$T + X_U + X_a + X_G = m(\dot{U} + WQ - VR) \tag{4.1.1}$$

Thrust (T) , friction from the undercarriage (X_U), aerodynamic drag (X_a) and gravity (X_G) are the contributors to axial motion from the body. Friction and drag is however difficult to model accurately and only cause steady state errors that vary with speed. This allows them to be omitted from the dynamic model and considered disturbances. Since lateral velocity (V) and yaw rate (R) are small, their product is negligibly small and can be ignored. Pitch rate (Q) is ignored due to the decoupling assumption. Gravity will not act axially as the aircraft remains parallel to the runway. Thus Equation 4.1.1 simplifies to Equation 4.1.2 for controller design.

$$T = m(\dot{U}) \tag{4.1.2}$$

4.1.2 Control Design

Before the aircraft commences Take-off, it has to be lined up with the runway. This is a low speed manoeuvre at taxi speeds. As the steering wheel only works while the aircraft is moving, a groundspeed controller is designed to regulate a low groundspeed until the aircraft is lined up.
The design specifications are,

- Rise time under 5 seconds.
- Overshoot of less than 10%.

Steady state errors are not of much concern as the groundspeed controller is used only while the aircraft lines up on the runway. Due to the low amount of runway friction on UAVs, any significant throttle increase will produce motion.

The most important design constraint is not the open loop response frequency of the engine, but rather its actuation. Thrust produced by the engine (or propeller) is dependant on the airflow through the engine. If this airflow is turbulent due to a noisy throttle actuator, the engine will produce less thrust than expected at a specified thrust setting or possibly stall. The only sensor on our aircraft that can measure the effect of thrust, is the axial (x_B-axis) accelero-

meter. Due to vibration, this accelerometer is noisy and, as a result, direct feedback from this sensor will be avoided.

The linear plant used for both controllers is made up of the axial EOF (Equation 4.1.2) and the thrust actuator model (Equation 3.4.1) and stated in transfer function form in Equation 4.1.3.

$$\frac{a_x}{T_c} = \frac{\frac{1}{m}}{\tau_T s + 1} \tag{4.1.3}$$

4.1.3 Groundspeed Controller

The groundspeed controller does not have to be an accurate controller as it is only used to generate some groundspeed until the aircraft is lined up. A simple proportional controller is implemented. The control law is defined as:

$$T_c = k_v \left(\overline{V}_{g_{ref}} - \overline{V}_g \right) \tag{4.1.4}$$

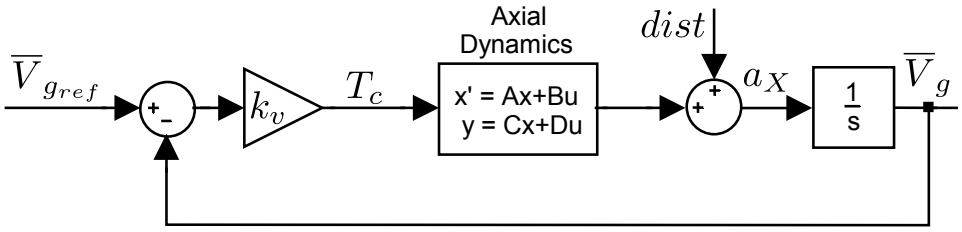

Figure 4.1: Taxi groundspeed controller architecture

Implementing the control law, the closed loop transfer function is,

$$\frac{\overline{V}_{g_{ref}}}{\overline{V}_g} = \frac{\frac{k_v}{m\tau_T}}{s^2 + \frac{1}{\tau_T}s + \frac{k_v}{m\tau_T}} \tag{4.1.5}$$

Controller gain and Pole placement

There are two poles present in the system described in Equation 4.1.5. They will be placed as a complex pole pair with their damping (ζ_τ) to be controlled. The only force that can slow the aircraft down at low speeds is the friction from the wheels, which is small. To reduce the possibility of overshoot, this controller's damping is high. The controller gain and damping is calculated as,

$$k_v = \frac{m}{4\tau_T \zeta_\tau^2} \quad \text{with,} \quad \zeta_\tau = 0.9 \tag{4.1.6}$$

Step Response

The closed loop root locus and linear step response is shown in Figure 4.2. As no disturbances are present, there is no steady state error. The rise time is within the desired specification.

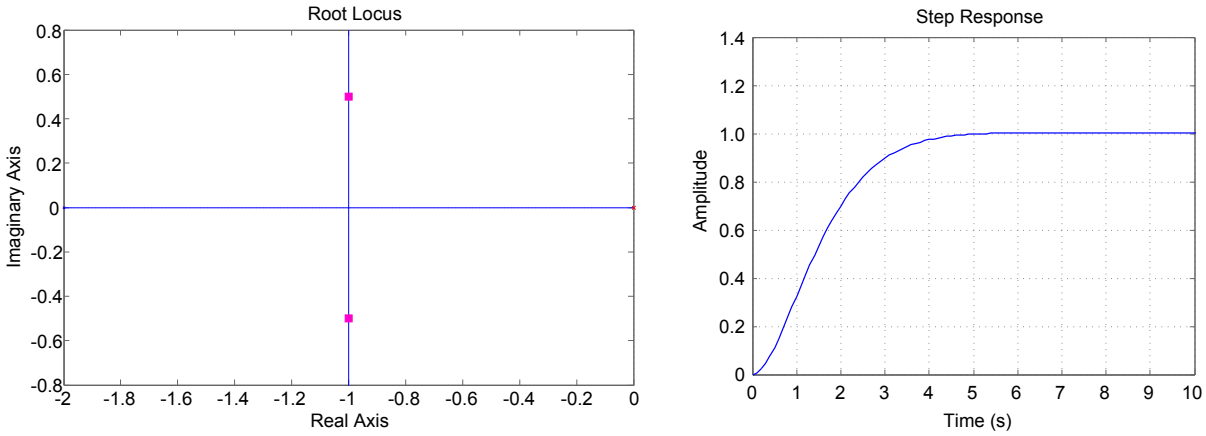

Figure 4.2: Taxi groundspeed controller root locus and linear step response

4.1.4 Throttle ramp

Once the aircraft is lined up with the runway, it needs to accelerate to reach rotation speed. The strategy of axial acceleration control can be used to quantify the response of the thrust. There are however two limiting factors. Firstly, the quadratic increase in drag will require a type 4 system to follow it with a zero steady state error. But by far the dominant reason is the lack of actuation. Unless a small acceleration is required, the controller would saturate the thrust command quickly. The purpose of this controller is to accelerate the aircraft up to V_r as fast as possible which allows for the shortest required runway length.

It was thus deemed unnecessary to design a closed loop system. Rather a open loop ramp is applied to the throttle that opens it to maximum within a specified time. A linear fit is used in Equation 4.1.7 to actuate the throttle, where T_{max} is the maximum thrust available, t_{max} is the time the throttle takes to open the throttle to maximum. T_{start} is the throttle value when the ramp is applied at t_{start}. A graphical depiction is shown in Figure 4.3.

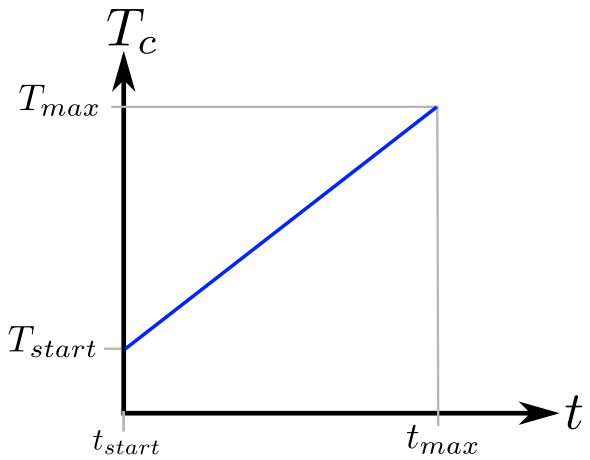

Figure 4.3: Take-off throttle ramp

$$T_c = \frac{T_{max}}{t_{max}} t + T_{start} \tag{4.1.7}$$

4.2 Runway Pitch Control

Pitch control is crucial during Take-off. Any wind gusts can pitch the aircraft before $\overline{V}_r$ is reached, causing it to stall. It is thus essential that the aircraft's pitch is controlled. The undercarriage will not necessarily keep the aircraft at a zero pitch angle (θ). If the controller tries to enforce a zero pitch angle, the actuator could saturate. Thus, during the Groundroll phase, pitch rate will be regulated to reject any pitch disturbances due to wind. Once $\overline{V}_r$ is reached the aircraft must pitch up to depart the runway. Pitch angle control will be required for this.

4.2.1 Decouple

Pitch motion on the runway has no lateral component as is defined as pure rotation about the y_B-axis. The undercarriage produces a stable restoring pitch moment, but as the normal forces cannot be measured it is difficult to model. A pure aerodynamic model is thus derived so that wind disturbances can be rejected.

Using Equation 3.1.5, the pitch motion is described by a 1-DOF EOM 4.2.1.

$$M = \dot{Q}I_y + PR\left(I_x - I_z\right) + \left(P^2 - R^2\right)I_{xz} \tag{4.2.1}$$

Enforcing the assumptions made earlier, $P = I_{xy} = 0$, the pitch EOM simplifies to Equation 4.2.2.

$$M = \dot{Q}I_y \tag{4.2.2}$$

Since only the aerodynamic effects are taken into account, the aerodynamic pitching moment (M_a) from Equation 3.3.1 is used. Applying a small angle of attack assumption, the contribution to pitching moment of $C_{m_\alpha}\alpha$ is negligibly small compared to $\frac{c}{2\overline{V}_a}C_{m_q}Q$ and is omitted. The aerodynamic moment is simplified to,

$$M_a = \overline{q}Sc\left(\frac{c}{2\overline{V}_a}C_{m_Q}Q + C_{m_{\delta_E}}\delta_E\right) \tag{4.2.3}$$

4.2.2 Linear

The dynamic decoupled equation (Equation 4.2.2) for pitch shows that the only dynamic variable is pitch rate (Q), and it can be measured. The state space representation is directly written in Equation 4.2.4.

$$\begin{aligned}\dot{Q} &= \left[\frac{\overline{q}Sc^2C_{m_Q}}{2\overline{V}_aI_y}\right]Q + \left[\frac{\overline{q}ScC_{m_{\delta_E}}}{I_y}\right]\delta_E \\ &= \left[A_Q\right]Q + \left[B_Q\right]\delta_E \\ Q &= [1]Q + [0]\delta_E\end{aligned} \tag{4.2.4}$$

4.2.3 Pitch Rate Controller

Since the plant can be described by a single real pole, the closed loop pole can theoretically be placed as fast a desired. Practically this would lead to excessive actuation effort. The rate regulator is not explicitly designed. Rather, the pitch rate controller is designed with PI control to give a specified closed loop pole placement.

In order to implement proportional rate feedback damper, the feedback gain needs to be designed. Instead of explicitly designing the gain, the proportional gain of the PI controller is used for the damper. Since k_q will always be positive, the rate damper will always be stable.

PI controller design

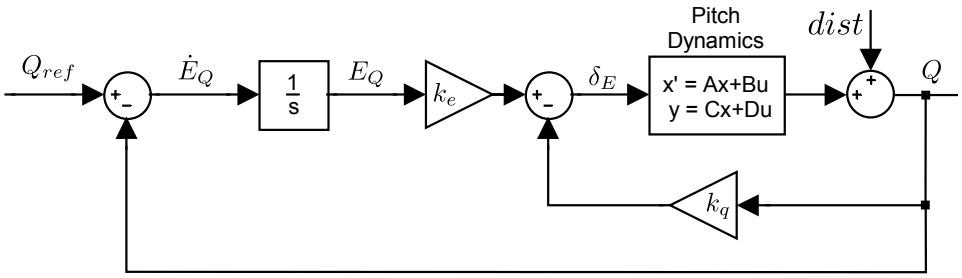

Figure 4.4: Runway pitch rate controller architecture

Since the airframe is stable its natural frequency is fast enough for the purpose of controller design, only the damping is to be changed. The closed loop poles are placed at the open loop frequency to prevent excessive actuator use. The two complex poles that are placed will have a frequency of ω_Q and damping ζ_Q. The control law, architecture and gain calculations are,

$$\begin{aligned} \delta_E &= k_e E_Q - k_q Q \\ \dot{E}_Q &= Q_{ref} - Q \end{aligned} \tag{4.2.5}$$

With closed loop pole locations and controller gains of,

$$\begin{aligned} \omega_Q &= A_Q & \qquad k_q &= \frac{2\zeta_Q\omega_Q + A_Q}{B_Q} \\ \zeta_Q &= 0.8 & \qquad k_e &= \frac{\omega_Q^2}{B_Q} \end{aligned} \tag{4.2.6}$$

Rate regulator implementation and Disturbance rejection

Using the gain calculated above, the rate regulator implementation is shown in Figure 4.5. A disturbance rejection plot is shown in Figure 4.6. Since no integrator is present, a steady state error could be present. This error will be eliminated by the undercarriage.

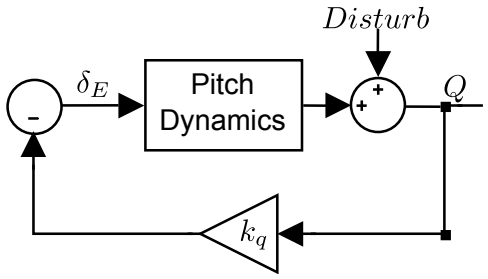

Figure 4.5: Runway pitch rate controller linear disturbance rejection

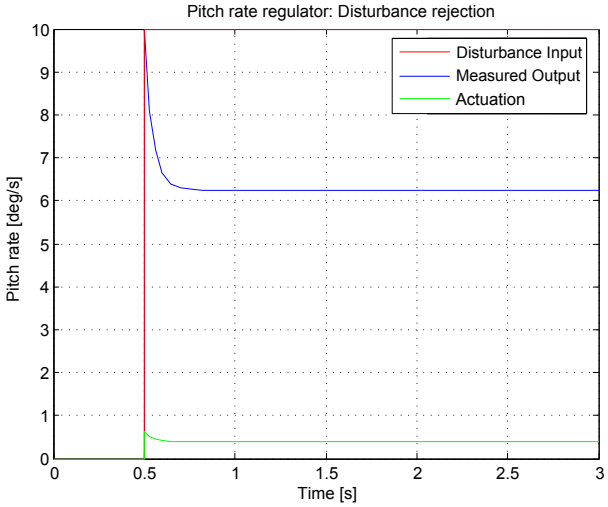

Figure 4.6: Linear runway pitch rate regulator with a $10°/s$ disturbance

4.2.4 Runway Pitch Angle Control

No guidance is required for pitch control while the aircraft is busy with the Groundroll phase. Once the aircraft has reached $\overline{V_r}$, it has to become airborne by rotating (pitching up). A constant pitch angle is then required to ensure the aircraft remains airborne. A pitch angle controller is thus implemented.

The design requirements are as follows,

- Rejection within 4 seconds.
- Zero steady state error.

Pitch Angle Controller Design

The pitch angle controller is designed using consecutive loop closure, with the pitch rate PI controller as its innerloop. The PI rate controller is designed to eliminate any steady state errors and as no pitch angle disturbances are present, proportional control will be used for the angle loop. The control law and architecture are shown below,

$$Q_{ref} = k_\theta \left(\theta_{ref} - \theta\right) \tag{4.2.7}$$

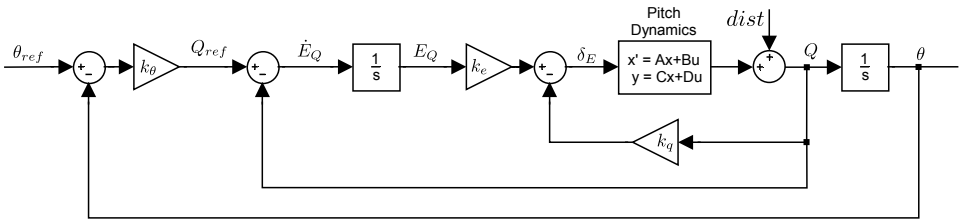

Figure 4.7: Runway pitch angle controller architecture

Pole placement and Controller gain

This architecture takes the rate controller's dynamics into account, which allow for the maximising of the angle loop frequency. The position of one real pole is controllable, which will be the angle pole (ω_θ). In order to keep the controller general, a frequency of ω_θ is determined in terms of the innerloop frequency (ω_Q). This controller gain and closed loop frequency is shown in Equation 4.2.8, with the resulting root locus shown in Figure 4.8.

$$\begin{aligned} k_\theta &= \frac{\omega_\theta^2 \left(A_Q - k_q B_Q + \omega_\theta\right)}{k_e B_Q} + \omega_\theta \\ \omega_\theta &= \frac{\omega_Q}{4} \end{aligned} \tag{4.2.8}$$

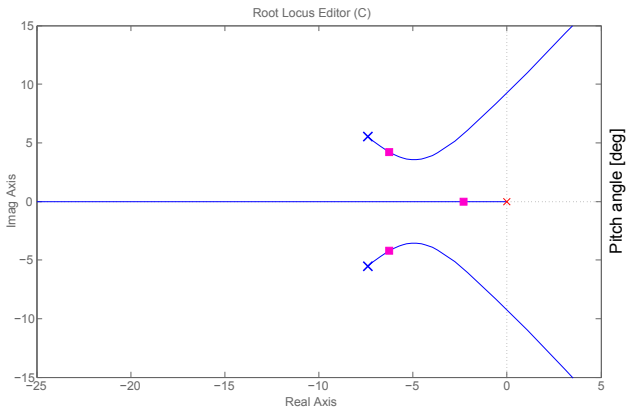

Figure 4.8: Runway pitch angle controller root locus

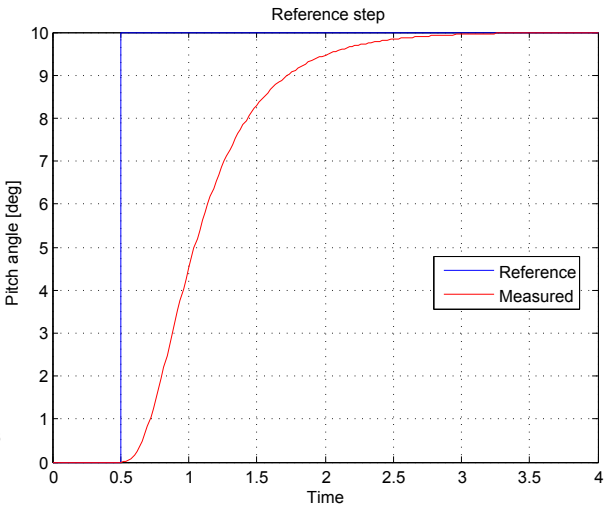

Figure 4.9: Runway pitch angle controller linear reference step response

Step response

A pitch angle step is shown in Figure 4.9. The reference is tracked within 3 seconds with no steady state error, fulfilling the design requirements.

4.3 Runway Roll Control

The restoring moments that are created by the undercarriage keeps the aircraft's wings level. Wind disturbances can roll the aircraft and need to be rejected. As this is a purely aerodynamic disturbance, the aerodynamic actuator is well suited to rejecting these disturbances.

The undercarriage does not guarantee a zero roll angle while stationary. Trying to regulate the roll angle could cause the aerodynamic actuator to saturate. Wind produces a roll moment disturbance, which can be rejected with a rolling rate regulator. Once the aircraft rotates, the wings will be kept level with a roll angle controller.

4.3.1 Decouple

From previous work it has been found that pitching and rolling motion can be totally decoupled [13]. Since the ailerons are well suited to controlling the roll of the aircraft, a 1-DOF EOM model is decoupled for wind disturbance rejection from Equation 3.1.5, and shown in Equation 4.3.2.

$$L = \dot{P}I_x - \dot{R}I_{xz} + QR\left(I_z - I_y\right) - PQI_{xz} \tag{4.3.1}$$

If there is pure rolling motion, we can assume that there is no lateral motion ($\beta = \dot{R} = R = Q = 0$). Equation 4.3.1 then simplifies to,

$$L = \dot{P}I_x \tag{4.3.2}$$

Since only the aerodynamic moments (L_a) are taken into account, Equation 3.3.1 describes these moments. The rudder has a negligible influence on roll compared to the ailerons, and is thus omitted. Since α is a small angle, Equation 3.3.1 simplifies to:

$$\begin{aligned} L_a &\simeq \bar{q}Sb\left(C_{L_S}\right) \\ &\simeq \bar{q}Sb\left(\frac{b}{2\overline{V}_a}C_{l_p}P + C_{l_{\delta_A}}\delta_A\right) \end{aligned} \tag{4.3.3}$$

4.3.2 Linear

Equation 4.3.2 identifies the state for the roll EOM to be roll rate (P), which can be measured. The state space form is thus,

$$\begin{aligned} \dot{P} &= \left[\frac{\bar{q}Sb^2C_{l_p}}{2\overline{V}_aI_x}\right]P + \left[\frac{\bar{q}SbC_{l_{\delta_A}}}{I_x}\right]\delta_A \\ &= \left[A_P\right]P + \left[B_P\right]\delta_A \\ P &= \left[1\right]P + \left[0\right]\delta_A \end{aligned} \tag{4.3.4}$$

4.3.3 Roll rate regulator

Since the criteria in terms of operation is the same as for pitch control, the same control architecture will be used (Figure 4.4). Only the pole placement will differ.

Using the state space model in Equation 4.3.4, the control law is defined in Equation 4.3.5. The controller gains are calculated in Equation 4.3.6, with desired closed loop frequency (ω_P) and damping (ζ).

$$\delta_A = k_e E_P - k_p P \tag{4.3.5}$$

$$\begin{aligned} k_p &= \frac{2\zeta_P \omega_P + A_P}{B_P} \\ k_e &= \frac{\omega_P^2}{B_P} \end{aligned} \tag{4.3.6}$$

The rate damping implementation is shown below in Figure 4.10.

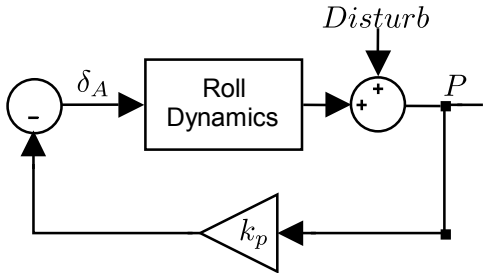

Figure 4.10: Runway roll rate regulator architecture

Pole placement

The closed loop system has two poles (open loop pole and integrator), which will be placed as a complex pole pair. The desired closed loop characteristic equation is shown in Equation 4.3.7.

$$s_{CL} = s^2 + (2\zeta_P \omega_P)\, s + \omega_P^2 \tag{4.3.7}$$

The closed loop poles will be placed at the same frequency as the open loop pole. This will give good roll rate disturbance rejection, without exciting unmodelled airframe dynamics. The damping is large since any unmodelled delays will practically reduce the damping. The control gain calculations are shown in Equation 4.3.6 and practically implemented open loop pole locations are shown below,

$$\begin{aligned} \omega_P &= A_P \\ \zeta_P &= 0.8 \end{aligned}$$

Disturbance response

The closed loop disturbance response is shown in Figure 4.11. As there is no integrator present in the controller, the disturbance will not always be followed with a steady state error.

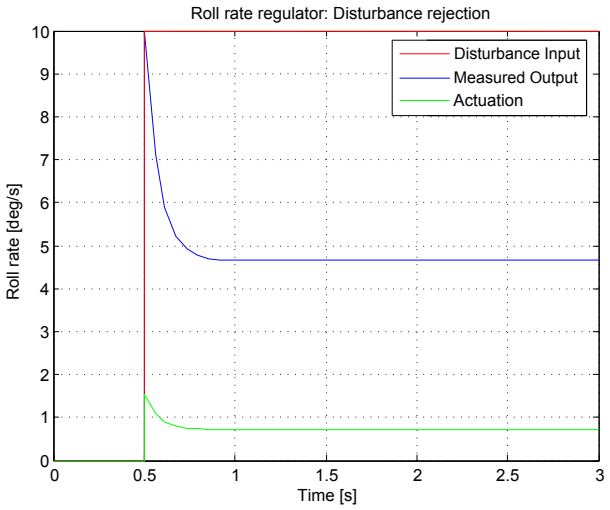

Figure 4.11: 10°/s linear roll rate disturbance response (runway controller)

4.3.4 Runway Roll Angle Control

Just like the pitch controller, no guidance is required for roll control during the Groundroll phase. Once the aircraft has rotated, its wings need to be kept level during the climb out phase to avoid it deviating off course.

- Rejection within 4 seconds.
- Zero steady state error.

Roll Angle Controller Architecture

The roll angle controller is designed using consecutive loop closure with the PI roll rate controller as its innerloop. As the rate controller is designed to follow references with a zero steady state error, a proportional controller will be sufficient for the angle controller as no angle disturbances are present. The architecture and control law are shown in Figure 4.12 and Equation 4.3.8.

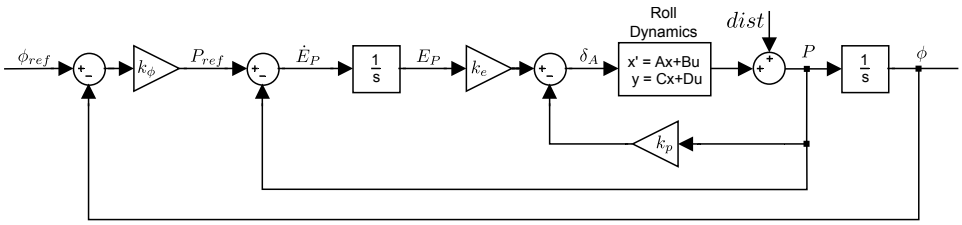

Figure 4.12: Runway roll angle controller architecture

$$P_{ref} = k_\phi \left(\phi_{ref} - \phi \right) \tag{4.3.8}$$

Controller gain

This control architecture allows freedom to place one real pole (ω_ϕ). It is placed much slower that the roll rate pole (ω_P) to avoid an overly aggressive controller. The controller gain calculation and pole location is shown below.

$$k_\phi = \frac{\omega_\phi^2 \left(A_P - k_p B_P + \omega_\phi\right)}{k_e B_P} + \omega_\phi \tag{4.3.9}$$

Pole placement

Since the closed loop roll rate pole is placed in terms of the plant's open loop frequency, the same is done with the roll angle closed loop pole. The angle controller is used to eliminate any angle error that might be caused due to the lag in the roll rate controller. It is thus placed at a much lower frequency.

$$\omega_\phi = \frac{\omega_P}{4} \tag{4.3.10}$$

4.4 Summary

This concludes the first part of the runway controllers design. The throttle-, pitch- and roll controllers will enable the aircraft to accelerate and become airborne while rejecting any disturbances that could cause premature rotation and a wing to strike the ground. These controllers can also implement the Rotation phase. The rate regulators are augmented with angle controllers to control pitch and roll.

The lateral position control is now lacking to complete automation of Take-off. The analysis and design of this controller is done in the following chapter.

Chapter 5

Take-off part 2: Lateral Analysis and Control

This chapter is dedicated to the lateral runway controller. The lateral runway controller is crucial to automating Take-off as it will prevent the aircraft from veering off the runway.

Since this controller must function over a large variety of speeds, the lateral modes of motion will be analysed after decoupling assumptions have been applied. This analysis will then be used to design a suitable innerloop controller that ensures the stability of the lateral mode. Linear simulation results of this controller will be shown.

A lateral guidance controller will then be designed to ensure that the aircraft does not depart the runway (off the sides). The linear simulation results of the entire lateral runway controller will be shown.

The same assumptions are used as in Chapter 4, namely:

- No wind is present, thus airspeed is equal to groundspeed.
- The lateral velocity is much smaller than axial velocity.
- The xy_B plane is assumed parallel to the xy_E-plane.

Throughout this chapter undercarriage, aerodynamic and gravity components are shown with U, a and G subscripts respectively.

5.1 Decoupling

As axial motion already covers 1-DOF in the xy_B-plane, the lateral model completes the motion in the xy_B-plane with a 2 DOF dynamic EOM.

$$\begin{aligned} Y_U + Y_a + Y_G &= m(\dot{V} + UR - WP) \\ N_U + N_a &= \dot{R}I_z - \dot{P}I_{xz} + PQ\left(I_y - I_x\right) + QRI_{xz} \end{aligned} \tag{5.1.1}$$

Since lateral motion is constrained to the xy_B-plane, ($W = P = \dot{P} = Q = Y_G = 0$). The undercarriage's lateral forces and moments have a component of friction (X_s, X_l and X_r) that can be ignored, as it has a negligibly small contribution. The aerodynamic contribution to

lateral motion from the ailerons, are negligibly small. As ground- and airspeed change much slower than lateral motion, it is considered constant.

$$\begin{aligned} Y_U + Y_a &= m(\dot{V} + UR) \\ N_U + N_a &= \dot{R} I_z \end{aligned} \tag{5.1.2}$$

The runway and aerodynamic lateral forces and moments simplify to,

$$\begin{aligned} \mathrm{Y}_U &= \mathrm{Y}_s \cos(-\delta_s) + \mathrm{Y}_l + \mathrm{Y}_r \simeq \mathrm{Y}_s + \mathrm{Y}_l + \mathrm{Y}_r \\ \mathrm{N}_U &= l_s \mathrm{Y}_s \cos(-\delta_s) - l_m \mathrm{Y}_l - l_m \mathrm{Y}_r \simeq l_s \mathrm{Y}_s - l_m \mathrm{Y}_l - l_m \mathrm{Y}_r \\ \mathrm{Y}_a &= \bar{q} S \left(C_{y_\beta} \beta + \frac{b}{2\overline{V}_a} C_{y_R} R + C_{y_{\delta_R}} \delta_R \right) \\ \mathrm{N}_a &= \bar{q} S b \left(C_{n_\beta} \beta + \frac{b}{2\overline{V}_a} C_{n_R} R + C_{n_{\delta_R}} \delta_R \right) \end{aligned} \tag{5.1.3}$$

Normal forces on the wheels

Since there is no normal motion during Groundroll, the EOM describing the normal modes of motion are used as a 1-DOF static model for determining the normal force on the tyres. Applying the same simplifications as for the lateral mode, there will be no pitch or roll. There will be no change in normal acceleration as the tyres are in constant contact with the runway. The equation describing the normal force is thus,

$$Z_U + Z_a + Z_G = 0 \tag{5.1.4}$$

The undercarriage force component is equal to the total normal force on the tyres ($Z_U = -N$). The aerodynamic force is created by the lift and drag of the aircraft. The non-dimensional coefficients that directly affect lift are described by Equation 3.3.3. Assuming that the only motion is axial and lift is only produced by the main wing, C_L reduces to $C_L = C_{L_0} + C_{L_\alpha}\alpha$. The total aerodynamic force thus becomes,

$$Z_a = \bar{q} S \left(C_{L_0} + C_{L_\alpha} \alpha \right) \tag{5.1.5}$$

And the total normal force is,

$$N = mg - \bar{q} S \left(C_{L_0} + C_{L_\alpha} \alpha \right) \tag{5.1.6}$$

5.2 State Space Representation

State Space is a linear representation of the model in matrix form. Writing the model in State Space form would aid analysis, understanding and controller design of the coupled system. The system needs to be linearised before it can be written in state space form.

Linearisation is done by applying small angle approximations and then linearising about a small change in state. Calculating the partial derivative of the dynamic equation, with respect to the specific state, will produce a small linear region of interaction.

Any trigonometric function that is applied to a small angle (less than 10°), can be assumed linear. If Θ is a small angle (in radians), the simplification would yield,

$$\begin{aligned} \sin(\Theta) &\simeq \Theta \\ \cos(\Theta) &\simeq 1 \\ \arctan(\Theta) &\simeq \Theta \end{aligned}$$

Linearised Lateral Model

It is clear from equations 5.1.2 that there are two states present in the lateral mode of motion. The first is yaw rate (R) which is a result of an applied moment. The second is lateral body velocity (V), due to lateral forces. The V state does, however, not give much insight into the aircraft's motion without knowing the axial velocity (U). Side slip (β) is a more practical state as it takes both lateral- (V) and axial velocity (U) into account, and is directly linked to the tyre force and the direction of the velocity vector. As a result, it is preferable for the lateral velocity state to be transformed to β, with the conversion shown below, where $\overline{V}$ is the velocity magnitude.

$$\begin{aligned} \frac{V}{\overline{V}} &= \sin(\beta) \quad [3] \\ \therefore V &= \overline{V}\sin(\beta) \end{aligned} \tag{5.2.1}$$

Applying a small angle approximation to Equation 5.2.1, with the knowledge that axial velocity is significantly larger than lateral velocity ($U \gg V$) and normal velocity is zero ($W = 0$),

$$\begin{aligned} \overline{V} &= \sqrt{U^2 + V^2 + W^2} \simeq U \\ \therefore V &\simeq U\beta \\ \dot{V} &\simeq U\dot{\beta} + \dot{U}\beta \\ \text{but } \dot{U}\beta &\simeq 0 \\ \therefore \dot{V} &\simeq U\dot{\beta} \end{aligned} \tag{5.2.2}$$

Applying a small angle approximation and the side slip conversion, yields the lateral EOM.

$$\begin{aligned} \dot{\beta} &= \frac{Y_U + Y_a}{mU} - R \\ \dot{R} &= \frac{N_U + N_a}{I_z} \end{aligned} \tag{5.2.3}$$

Y is a function of β, and lateral acceleration (a_Y) measurements. Lateral acceleration measurements will thus contain information about β and will therefore be used as an output for the state space model. The output equation for lateral acceleration is given in Equation 5.2.4 and the linearised state space model is summarised in Equation 5.2.5. These equations are linearised in appendix C.

$$a_Y = \frac{Y}{m} \tag{5.2.4}$$

$$\begin{aligned}
\begin{bmatrix} \dot{\beta} \\ \dot{R} \end{bmatrix} &= \begin{bmatrix} \frac{NC_{\alpha\alpha}}{mU} + \frac{\bar{q}S}{m\overline{V}_a} C_{y_\beta} & \frac{\bar{q}S}{m\overline{V}_a} \frac{b}{2\overline{V}_a} C_{y_r} - 1 \\ \frac{\bar{q}Sb}{I_z} C_{n_\beta} & \frac{l_s l_m NC_{\alpha\alpha}}{I_z U} + \frac{\bar{q}Sb}{I_z} \frac{b}{2\overline{V}_a} C_{n_r} \end{bmatrix} \begin{bmatrix} \beta \\ R \end{bmatrix} + \begin{bmatrix} \frac{NC_{\alpha\alpha}}{mU} \frac{l_m}{l} & \frac{\bar{q}S}{m\overline{V}_a} C_{y_{\delta_R}} \\ \frac{l_s l_m}{l} \frac{NC\alpha\alpha}{I_z} & \frac{\bar{q}Sb}{I_z} C_{n_{\delta_R}} \end{bmatrix} \begin{bmatrix} \delta_S \\ \delta_R \end{bmatrix} \\
\begin{bmatrix} a_Y \\ R \end{bmatrix} &= \begin{bmatrix} \frac{NC_{\alpha\alpha}}{m} + \frac{\bar{q}S}{m} C_{y_\beta} & \frac{\bar{q}S}{m} \frac{b}{2\overline{V}_a} C_{y_r} \\ 0 & 1 \end{bmatrix} \begin{bmatrix} \beta \\ R \end{bmatrix} + \begin{bmatrix} \frac{NC_{\alpha\alpha}}{m} \frac{l_m}{l} & \frac{\bar{q}S}{m} C_{y_{\delta_R}} \\ 0 & 0 \end{bmatrix} \begin{bmatrix} \delta_S \\ \delta_R \end{bmatrix}
\end{aligned} \tag{5.2.5}$$

Now that a mathematical model has been derived that describes the lateral motion of the aircraft while it is on the runway, it would be advantageous to understand the model better before a controller is designed.

5.3 Understanding the Lateral Runway model for Control System Design Purposes

As the model is made up of undercarriage- and aerodynamic components, it will first be separated. The two separate models will be analysed independently. Once each model has been understood separately, they will be reunited to form the complete lateral model.

5.3.1 Undercarriage

Equation 5.2.5 simplifies to Equation 5.3.1 when all the aerodynamic interactions are eliminated. The normal force on the wheels are assumed to remain constant as groundspeed increases, since aerodynamic lift is ignored.

$$\begin{bmatrix} \dot{\beta} \\ \dot{R} \end{bmatrix} = \begin{bmatrix} \frac{NC_{\alpha\alpha}}{mU} & -1 \\ 0 & \frac{l_s l_m NC_{\alpha\alpha}}{I_z U} \end{bmatrix} \begin{bmatrix} \beta \\ R \end{bmatrix} + \begin{bmatrix} \frac{NC_{\alpha\alpha}}{mU} \frac{l_m}{l} \\ \frac{l_s l_m}{l} \frac{NC\alpha\alpha}{I_z} \end{bmatrix} \delta_S$$
$$\begin{bmatrix} a_Y \\ R \end{bmatrix} = \begin{bmatrix} \frac{NC_{\alpha\alpha}}{m} & 0 \\ 0 & 1 \end{bmatrix} \begin{bmatrix} \beta \\ R \end{bmatrix} + \begin{bmatrix} \frac{NC_{\alpha\alpha}}{m} \frac{l_m}{l} \\ 0 \end{bmatrix} \delta_S \quad (5.3.1)$$

There are many ways to analyse a model, but a block diagram representation was found to yield the best understanding. Equation 5.3.1 is shown in block diagram form in Figure 5.1. It is clear that there are two first order systems, namely side slip (β) and yaw rate (R).

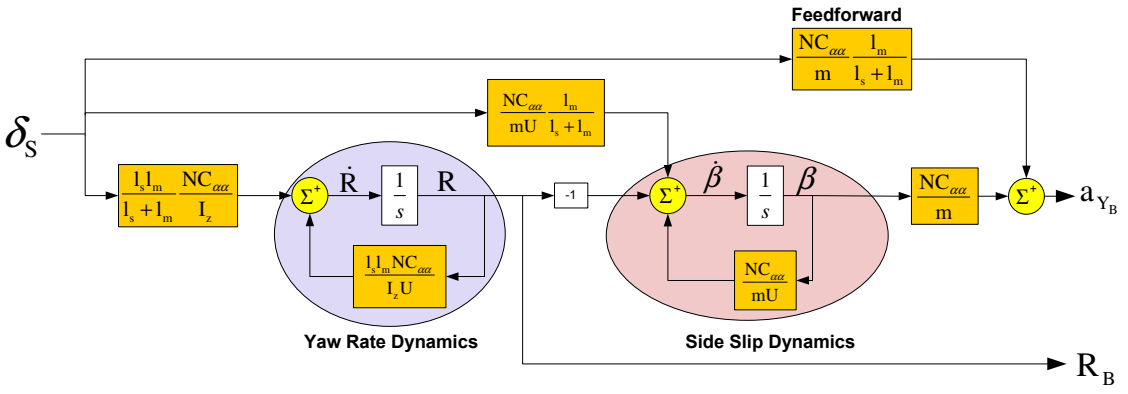

Figure 5.1: Block diagram representation of the Runway model, undercarriage effects only

Transient effects

A simplified progression of motion of the body due to a positive steering wheel deflection (δ_S), is shown in Figure 5.2 (viewed from above). Before the steering wheel is deflected the undercarriage is travelling forward at a constant groundspeed ($\overline{V}_g$), with no lateral velocity or yaw rate. A general description of an undercarriage is used, with only one wheel at the front (steering wheel) and one wheel at the back (main wheel, a combination of the left- and right main wheels) of the undercarriage. This simplification greatly aids insight while still remaining valid as long as movement is restricted to the xy_B-plane. It is assumed that $l_s = l_m$.

Figure 5.2.(a).1 The instant the steering wheel (δ_s) is deflected it creates an immediate local slip angle on the steering wheel (α_s), which causes a negative lateral force on the steering wheel (-Y_s). The local slip angle on the main wheel (α_m) will not have changed yet. Assuming the body's side slip angle (β) dynamics are faster than the yaw rate (R) dynamics (see Figure 5.3), no R is present.

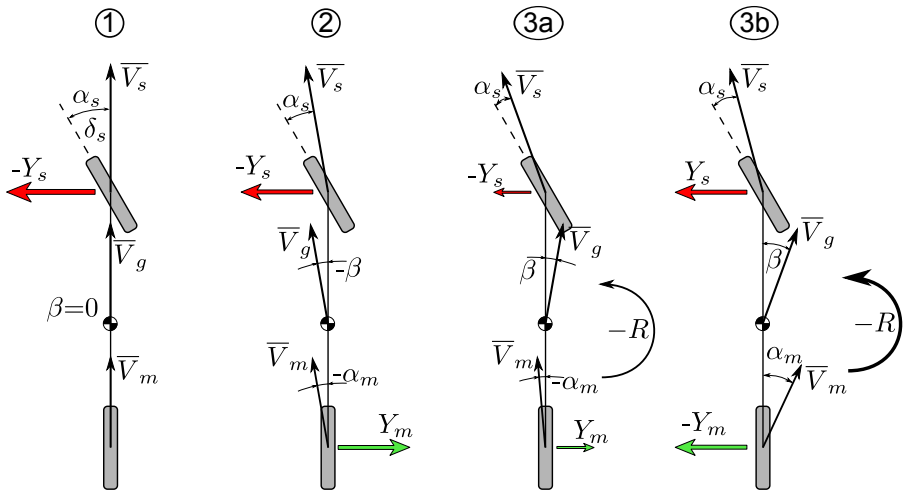

(a) Body forces and moments as a result of a δ_s deflection

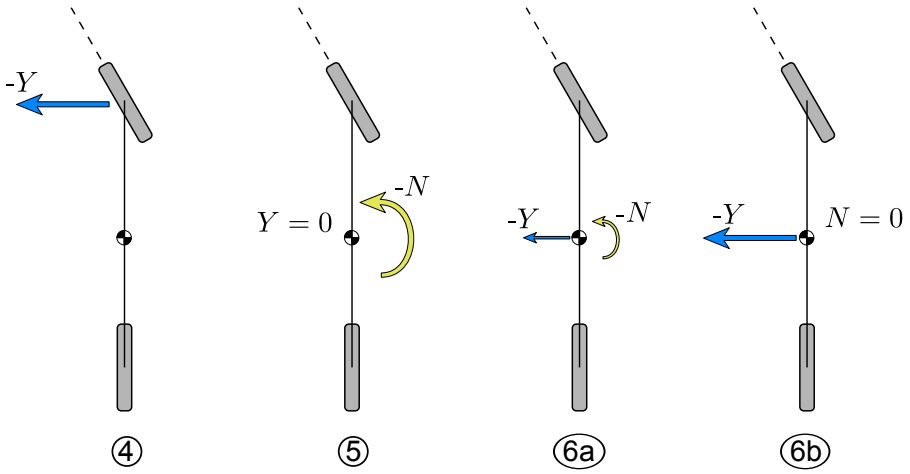

(b) Equivalent body forces and moments created by undercarriage

Figure 5.2: Sequence of force generation due to δ_s deflection, undercarriage effects (viewed from above)

Figure 5.2.(a).2 The applied force on the steering wheel will cause a negative β, which decreases α_s slightly while α_m increases negatively. This is a "differential mode" change in wheel slip angles, as the slip angles on the steering- and main wheels change in opposite directions. The β dynamics will settle quickly when the lateral forces on the steering wheel (Y_s) and main wheels (Y_m) are equal. After they have settled, the combined effect of $-Y_s$ and Y_m creates a moment couple.

The motion that follows is separated into two sequences, as it aids understanding.

Figure 5.2.(a).3a and 3b A yaw rate is produced by the presence of the moment couple. R will decrease α_s and α_m ("differential mode" change in slip angles), which decrease the forces on the wheels (3a). Thus the moment couple is being reduced, but at the same time β increases positively. As β builds up both α_s and α_m will increase in the same direction ("common mode" increase in slip angles), increasing the forces on the wheels and thus the force being applied to the CG (3b).

β will increase as long as there is a moment present. Once the moment has been eliminated, there will no longer be a build up of β and the body will settle with a constant R and Y.

Figure 5.2.(b).4-6b The overall effect of the tyre forces on the body are depicted in Figure 5.2.4 to 6.b. There is an initial force that acts on the steering wheel (Figure 5.2.(b).4). The "differential mode" change in slip angles causes a moment couple to be formed (Figure 5.2.(b).5). The increasing R reduces N, while increasing β and thus Y on the CG (Figure 5.2.(b).6a). β will continue to grow until $N = 0$, and the system will settle at a constant R and Y that acts on the CG to counter the body's centripetal acceleration (Figure 5.2.(b).6b).

Poles and Zeros

The poles and zeros give insight into how the system can be controlled. Figure 5.3 shows the undercarriage pole movement with a change in groundspeed. The two poles can be identified as the side slip angle pole (ω_β) and the yaw rate pole (ω_R). Both reduce in frequency with an increase in groundspeed.

The zeros of the system are dependant on the output under consideration. In both cases the zeros are caused by the feedforward from the steering wheel (δ_S). Figure 5.4 shows the complex pair of zeros for an acceleration (a_Y) output. Their position does not change much with groundspeed as their feedforward effect is not dependant on groundspeed. Since the steering wheel will cause a force in the same direction, too much feedback will cause the damping of the system to decrease.

Figure 5.5 shows the zero for a yaw rate (R) output is exactly on the ω_β pole. Since β does not feed back to create a moment, it can be seen that the zero cancels the pole. The system is thus reduced to a 1^{st} order system. This is also clear from the block diagram, as the β state has no effect on the R state. There is thus no feedforward from δ_S to R.

Since the general placement of the poles and zeros are relatively invariant to changes in groundspeed, it would thus be advantageous if the difference between the two real poles (ω_β

and ω_R) is large enough so that time scale separation (TSS) could be applied, which will allow the system to be reduced to a 1^{st} order system.

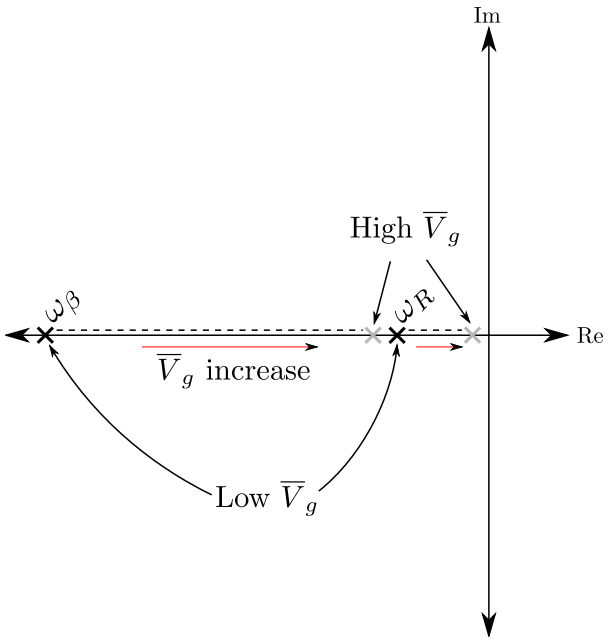

Figure 5.3: Poles of the Runway model (undercarriage effects only)

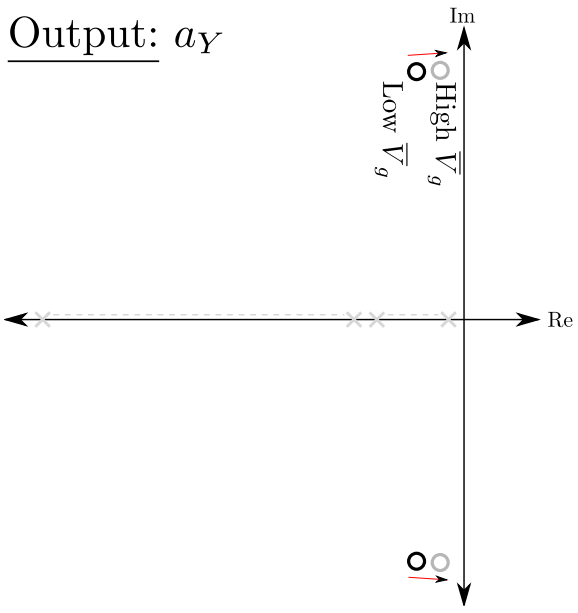

Figure 5.4: Zeros of the Runway model with a_Y as output (undercarriage effects only)

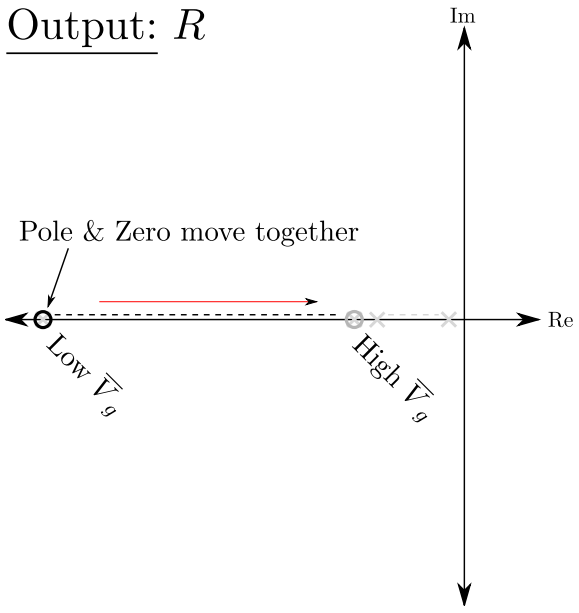

Figure 5.5: Zeros of the Runway model with R as output (undercarriage effects only)

Decoupling the undercarriage contribution to the Runway model

$$\frac{\omega_\beta}{\omega_R} = \frac{I_z}{m l_s l_m} \tag{5.3.2}$$

The relationship between these two frequencies is given by Equation 5.3.2 and does not vary with ground speed. It would be advantageous for future work if this equation is generalised, which would allow it to be applied to any undercarriage configuration. The radius of gyration (r_z) about the z_B-axis, and the undercarriage lengths are written in terms of the wheelbase length (l_L). This defines the relationship between ω_β and ω_R to be dependant on the mass distribution and the position of the centre of mass along the length of the wheelbase.

$$\begin{aligned} r_z &= \sqrt{\frac{I_z}{m}} \\ l_s &= a l_L \\ l_m &= (1-a) l_L \\ \therefore \frac{\omega_\beta}{\omega_R} &= \frac{r_z^2}{a(1-a) l_L^2} = \left(\frac{r_z}{l_L}\right)^2 \frac{1}{a(1-a)} \end{aligned} \tag{5.3.3}$$

In order for TSS to apply, $\frac{\omega_\beta}{\omega_R} > 5$ [13]. Once the body has been designed, its weight distribution (r_z) is fixed. Thus this relationship can only be altered by the positioning of the front and rear wheels relative to the CG. Figure 5.6 shows this relationship with variation in CG position between the front and rear wheels (where a is denoted as a percentage of the wheel base length, measured from the front wheels).

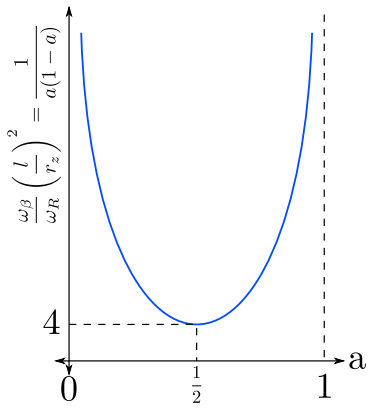

Figure 5.6: Undercarriage frequency variation caused by centre of mass position on the wheelbase

The minimum is found where,

$$\begin{aligned} \frac{\partial}{\partial a}\left(\frac{1}{a(1-a)}\right) = \frac{2a-1}{(a-a^2)^2} &= 0 \\ \therefore \frac{\partial}{\partial a}\left(\frac{1}{a(1-a)}\right)\Big|_{a=\frac{1}{2}} &= 0 \\ \frac{1}{a(1-a)}\Big|_{a=\frac{1}{2}} &= 4 \end{aligned} \tag{5.3.4}$$

This minimum is at $a = \frac{1}{2}$, where the CG is in the middle of the wheelbase.It must be remembered that the radius of gyration (r_z) and wheel base length (l_L) will change the offset of the curve in Figure 5.6.

Using these relationships, a ground vehicle can be designed so that it can be approximated as a 1^{st} order system yaw rate dynamics ($\dot{R}$).

5.3.2 Aerodynamic

Equation 5.2.5 simplifies to Equation 5.3.5 when ignoring the effect of the undercarriage.

$$\begin{bmatrix} \dot{\beta} \\ \dot{R} \end{bmatrix} = \begin{bmatrix} \frac{\bar{q}S}{m\bar{V}_a} C_{y_\beta} & \frac{\bar{q}S}{m\bar{V}_a} \frac{b}{2\bar{V}_a} C_{y_r} - 1 \\ \frac{\bar{q}Sb}{I_z} C_{n_\beta} & \frac{\bar{q}Sb}{I_z} \frac{b}{2\bar{V}_a} C_{n_r} \end{bmatrix} \begin{bmatrix} \beta \\ R \end{bmatrix} + \begin{bmatrix} \frac{\bar{q}S}{m\bar{V}_a} C_{y_{\delta_R}} \\ \frac{\bar{q}Sb}{I_z} C_{n_{\delta_R}} \end{bmatrix} \delta_R$$

$$\begin{bmatrix} a_Y \\ R \end{bmatrix} = \begin{bmatrix} \frac{\bar{q}S}{m} C_{y_\beta} & \frac{\bar{q}S}{m} \frac{b}{2\bar{V}_a} C_{y_r} \\ 0 & 1 \end{bmatrix} \begin{bmatrix} \beta \\ R \end{bmatrix} + \begin{bmatrix} \frac{\bar{q}S}{m} C_{y_{\delta_R}} \\ 0 \end{bmatrix} \delta_R \tag{5.3.5}$$

Just like the undercarriage, the aerodynamic effects are represented in block diagram form in

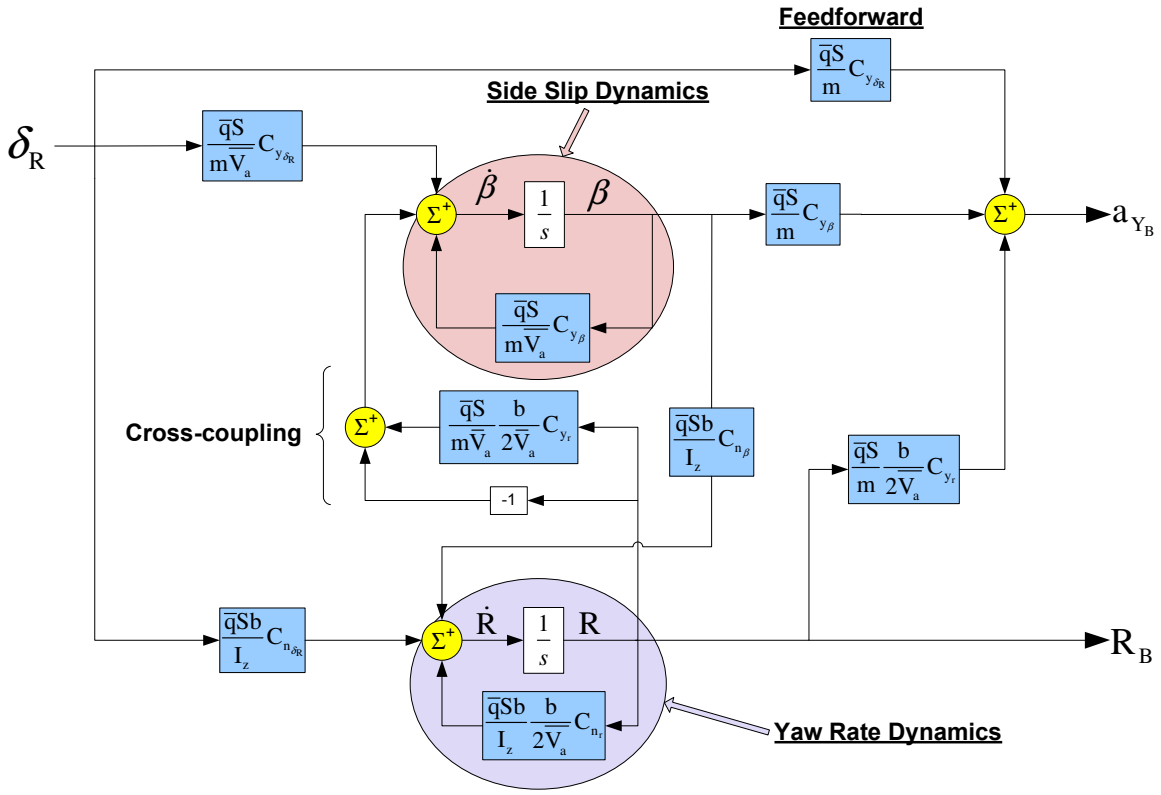

Figure 5.7: Block diagram representation of the Runway model, aerodynamic effects only

Figure 5.7. In this case it is a coupled 2^{nd} order system. This is very similar to the Dutch Roll mode of aircraft in flight. When the aircraft side slips, a lateral force is induced. This force mostly acts on the fin at a distance, causing a moment that induces a yaw rate.

Any yaw rate creates an induced local incidence angle on the fin. This increases the lateral aerodynamic force (lift) created by the fin, which directly induces a side slip angle while causing a yawing moment. The aerodynamic side slip and yaw rate can thus not be decoupled since conventional airframes (like the one used in this research) are designed to be stable with all the forces and moment restoring the aircraft to forward flight.

Poles and Zeros

The root locus (Figure 5.8) is vastly different from the undercarriage case. The coupled system is represented by two lightly damped complex poles. It is clear that the frequency of the poles increases with airspeed, but the change in damping will be analysed.

The characteristic equation of Equation 5.3.5 is analysed to determine how the damping (ζ) term is influenced by airspeed. Equation 5.3.6 shows this analysis.

$$\begin{aligned} s_{CL} &= s^2 - \left(\frac{\bar{q}S}{m\overline{V}_a}C_{y_\beta} + \frac{\bar{q}Sb^2}{2I_z\overline{V}_a}C_{n_r}\right)s - \left(\frac{\bar{q}Sb}{2m\overline{V}_a^2}C_{y_r} - 1\right)\left(\frac{\bar{q}Sb}{I_z}C_{n_\beta}\right) \\ &= s^2 - \frac{1}{2}\rho\overline{V}_aS\left(\frac{C_{y_\beta}}{m} + \frac{b^2C_{n_r}}{2I_z}\right)s - \frac{\frac{1}{2}\rho\overline{V}_a^2Sb}{I_z}\left(\frac{\frac{1}{2}\rho Sb}{2m}C_{y_r}C_{n_\beta} - C_{n_\beta}\right) \\ &= s^2 + (2\zeta\omega)s + \omega^2 \\ \therefore \zeta &= \frac{\frac{1}{2}\rho\overline{V}_aS\left(\frac{C_{y_\beta}}{m} + \frac{b^2C_{n_r}}{2I_z}\right)}{\sqrt{\frac{\frac{1}{2}\rho\overline{V}_a^2Sb}{I_z}\left(\frac{\frac{1}{2}\rho Sb}{2m}C_{y_r}C_{n_\beta} - C_{n_\beta}\right)}} \\ &= \frac{1}{2}\sqrt{\frac{\rho SI_z}{b}}\frac{\frac{C_{y_\beta}}{m} + \frac{b^2C_{n_r}}{2I_z}}{\sqrt{\frac{\rho Sb}{m}C_{y_r}C_{n_\beta} - C_{n_\beta}}} \end{aligned} \tag{5.3.6}$$

From Equation 5.3.6 it is clear that the damping of the system is not influenced by variation in airspeed.

The zeros, when considering the a_Y output (Figure 5.9), show that there is non-minimum phase present. This is caused by the rudder creating acceleration (force) in the opposite direction than the induced incidence angle in the steady state. As airspeed increases, the frequency of the zeros increase.

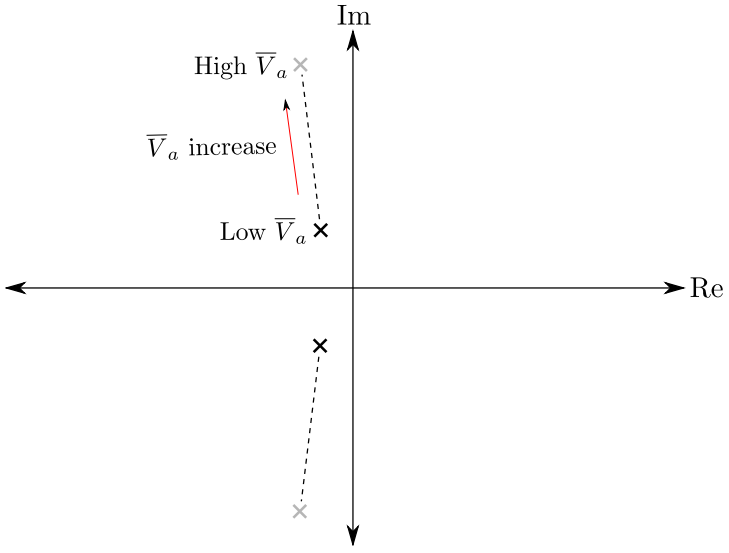

Figure 5.8: Movement of the Runway model poles (aerodynamics only)

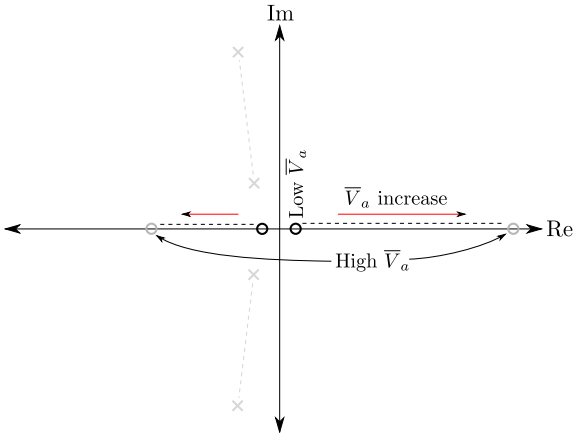

Figure 5.9: Zeros of the Runway model with a_Y as output (aerodynamic effects only)

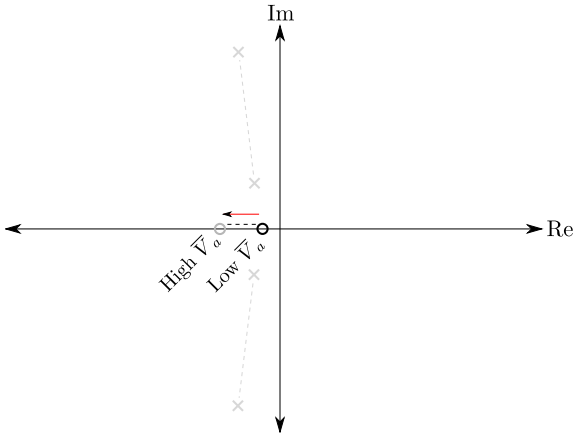

Figure 5.10: Zeros of the Runway model with R as output (aerodynamic effects only)

Figure 5.10 shows that when R is the output under consideration, any feedback will increase the damping of the system and with enough damping, the system will approach a 1^{st} order response. As airspeed increases, the frequency of the system increases. The general placement of the poles and zeros does not drastically change with airspeed.

5.3.3 Combined model

Now that the individual components to the lateral runway model are understood, they can be combined in one block diagram, which is represented in Figure 5.11. At low speeds, the model has the characteristics of the undercarriage model. At high speeds or when the wheels are not in contact with the runway (due to lift), the model is the same as the aerodynamic model. During medium speeds, these models interweave to produce a hybrid which is best understood by looking at the change of the pole and zero locations with variations in speed in Figure 5.12 (assuming ground- and airspeed are equal).

Poles

Assuming low initial speed, the undercarriage dominates the dynamics and we start with the poles at the same location as the undercarriage poles at ω_β and ω_R. As speed increases, ω_β and ω_R will reduce in frequency. As soon as the aerodynamic surfaces start becoming effective, the ω_R pole will increase in frequency.

The poles will continue along the real axis toward each other, until they meet at the same frequency and become complex. It is at this speed that the aerodynamic effects start to have a larger contribution to the model than the undercarriage. This point is affected by the amount of grip that the wheels have (thus the normal force). The damping of the poles will now reduce until they reach the damping of the aerodynamic model, while the frequency increases slightly. As soon as the airspeed is sufficient to lift the aircraft so that there is no normal force, the model will be purely aerodynamic.

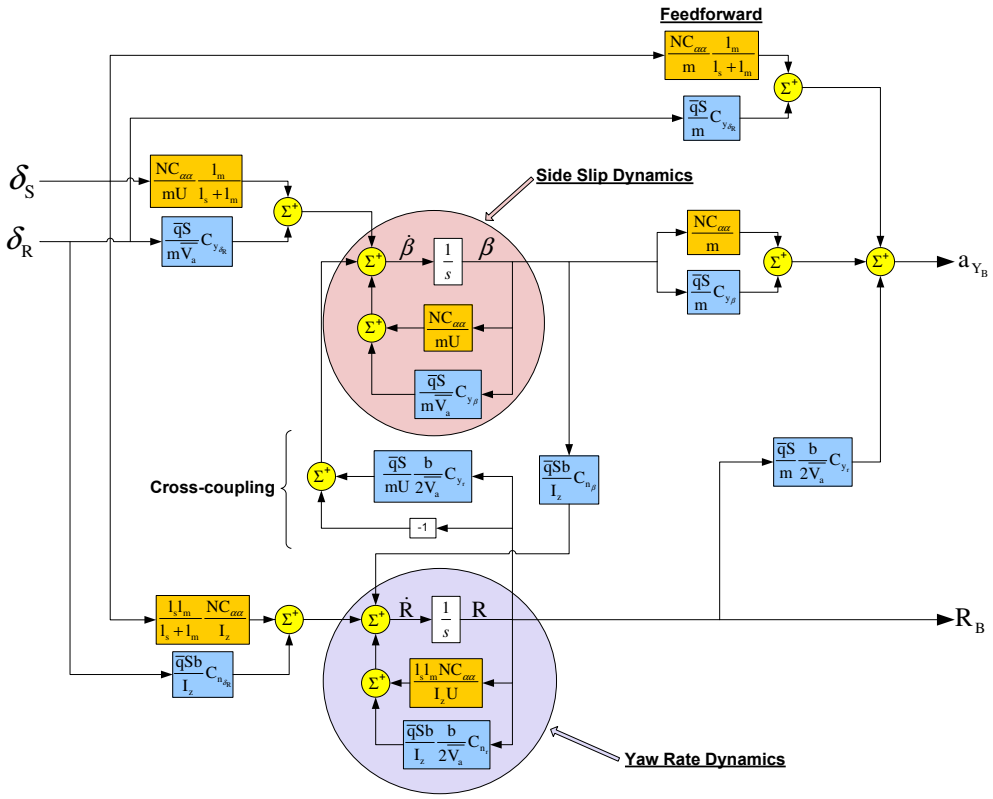

Figure 5.11: Block diagram of the Runway model, undercarriage and aerodynamics combined

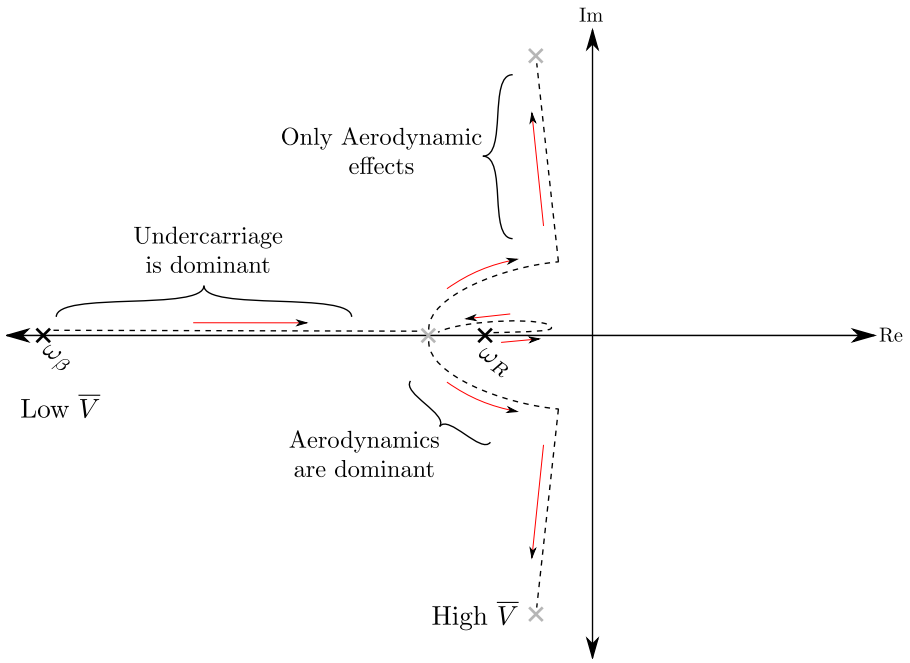

Figure 5.12: Pole movement of the Runway model due to speed increase (undercarriage and aerodynamics combined)

Zeros

The actuator being used and output influences the zeros of the system. The effect of each actuator on each output of the system will be analysed separately.

δ_S to a_Y: These zeros (Figure 5.13) start at the same position as in Figure 5.4. As the speed increases, the aircraft's lift increases therefore the normal force on the wheels decrease. The effectiveness of the steering wheel to actuate reduces, relating to the zeros moving to the origin. When there is no more normal force, the zeros are at the origin and the system has no more gain.

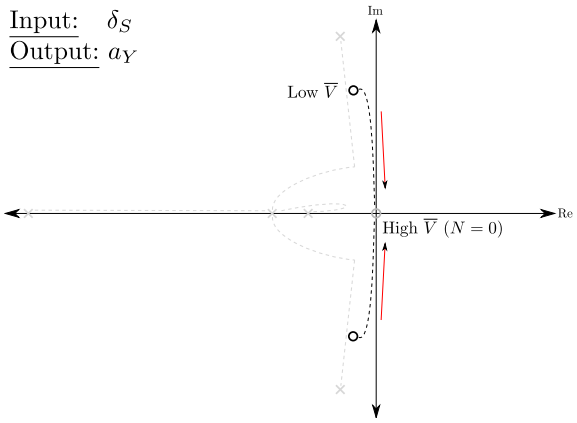

Figure 5.13: The effect of speed on the zeros seen from δ_S to a_Y (undercarriage and aerodynamics combined)

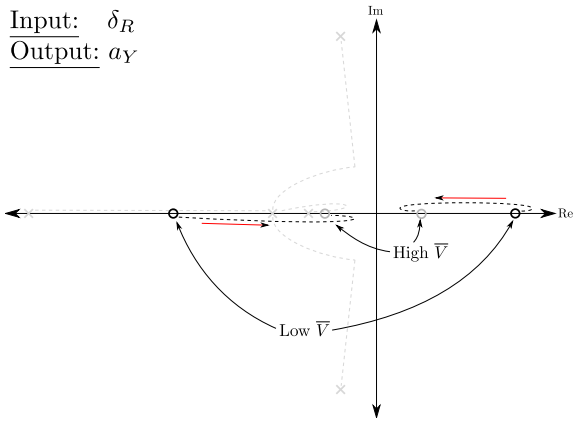

Figure 5.14: The effect of speed on the zeros seen from δ_R to a_Y (undercarriage and aerodynamics combined)

δ_R to a_Y: At low speed there are two real zeros at high frequencies (Figure 5.14). These represent the non-minimum phase caused by the rudder. As speed increases, their frequency will decrease which practically means that the non-minimum phase will be more pronounced. When the aerodynamic effects become dominant, the zeros will increase in frequency.

δ_S to R: Figure 5.15 shows the zero staring on the pole, but its frequency decreases slower than the pole. The zero will finally end up at the origin as the normal force reduces to zero. This relates to the steering wheel (δ_S) having no actuation at higher groundspeeds.

δ_R to R: The zero in Figure 5.16 starts off at a faster frequency than the closest pole. Its frequency will reduce until the aerodynamic forces become dominant. It will then increase in frequency.

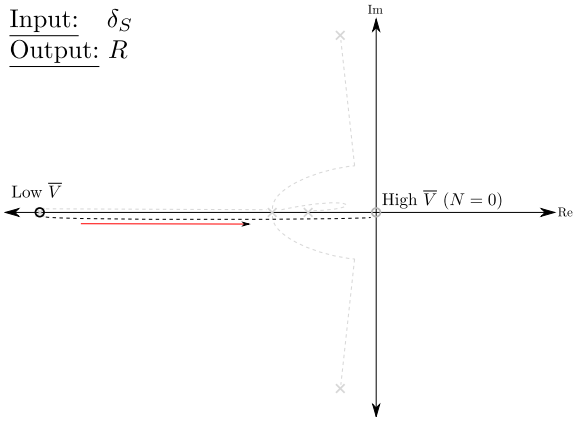

Figure 5.15: The effect of speed on the zero seen from δ_S to R (undercarriage and aerodynamics combined)

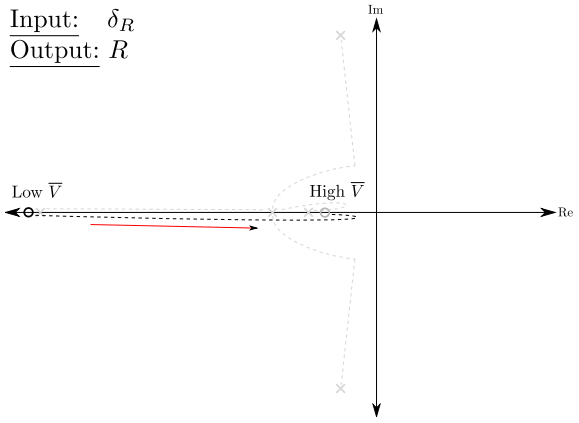

Figure 5.16: The effect of speed on the zero seen from δ_R to R (undercarriage and aerodynamics combined)

Most control architecture use direct feedback from a sensor to the actuator. It would thus be prudent to analyse the effect of such feedback, and thus on the root locus.

Figure 5.17 shows the root locus of feedback from a_Y to δ_S. At low speed, only small controller gains are advisable as large gains will reduce damping. At higher speeds, the root locus does not lend itself to changing the response of the system.

Figure 5.18 shows the root locus when feedback from a_Y to δ_R is applied. In both cases, any feedback will increase damping, but lower the closed loop frequency. The presence of the non-minimum phase zero could cause instability should the system's gain be larger than calculated. The effect of the non-minimum phase zero will also increase as speed increases.

Since neither actuator gives desirable change in the closed loop pole locations, it is not advisable to use direct feedback from the a_Y measurement. The root locus of feedback from R

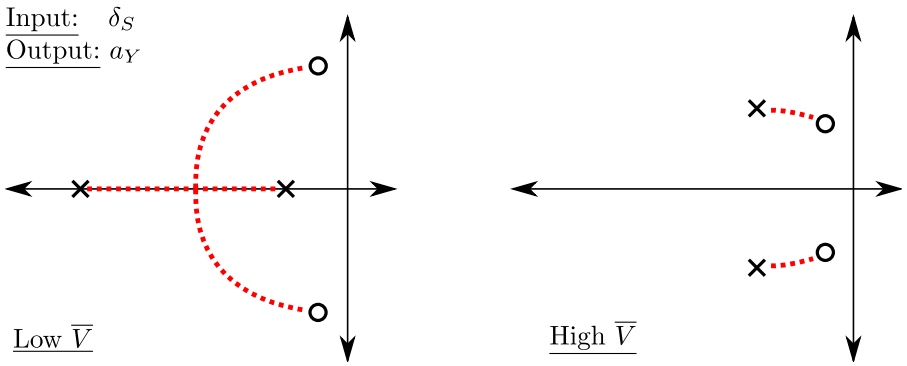

Figure 5.17: Conceptual root locus of direct feedback from a_Y to δ_S at low and high speeds. (undercarriage and aerodynamics combined)

to both δ_S and δ_R is shown in Figure 5.19 since both root loci are similar in shape. It is clear that at both low and high speed, this type of feedback will either increase frequency or damping, or both. Should the actual root locus differ, due to inaccuracies in modelling, the system is guaranteed to remain stable. Direct feedback from the R measurement is thus advisable.

Now that the lateral plant is understood, it can be used for controller design.

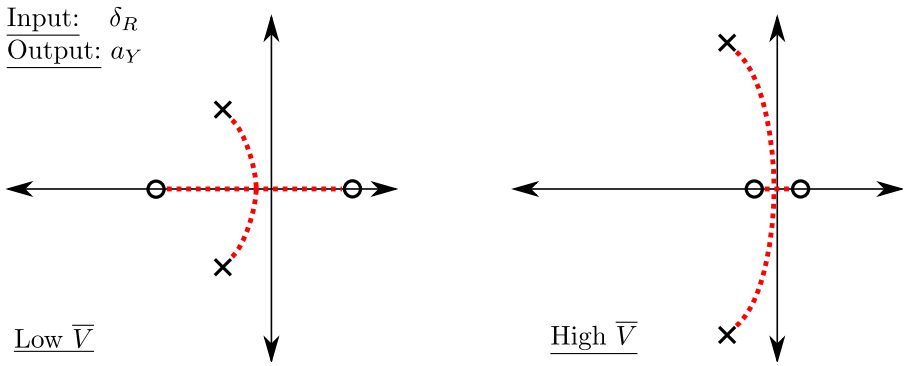

Figure 5.18: Conceptual root locus of direct feedback from a_Y to δ_R at low and high speeds. (undercarriage and aerodynamics combined)

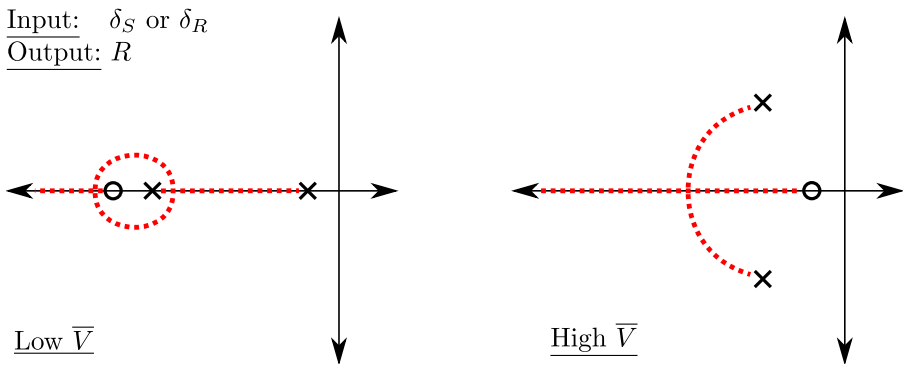

Figure 5.19: Conceptual root locus of direct feedback from R to δ_S or δ_R at low and high speeds. (undercarriage and aerodynamics combined)

5.4 Lateral Runway Innerloop Controller Design

Aircraft are exposed to a number of factors that cause it to deviate from the runway. These include wind, uneven surface and helical prop wash. This controller design is aimed at rejecting the effect of any of these factors and regulating the aircraft's stability while on the runway. The controller is designed with an interface that allows control over the fundamental motion of the aircraft, while on the runway. Since two actuators are present that have similar effects on the aircraft, a method of combining them needs to be defined before the controller can be designed.

5.4.1 Virtual actuator

The presence of two actuators, steering wheel (δ_s) and rudder (δ_R), with the capability of controlling the lateral runway motion of the aircraft, adds an extra dimension to the already complicated control problem. For the purpose of this thesis, it was decided to simplify the control system architecture by combining the two actuators into a single virtual actuator (δ_{Run}). This would allow the MIMO system to be reduced to a SIMO system, thereby simplifying the control problem.

Defining the Mix Law

A relationship between the virtual actuator δ_{Run} and the actual actuators is defined below,

$$\begin{bmatrix} \delta_s \\ \delta_R \end{bmatrix} = \begin{bmatrix} M_1 \\ M_2 \end{bmatrix} \delta_{Run} \tag{5.4.1}$$

Assuming an arbitrary dynamic system (shown below in state space form), the actuator (u) drives into the dynamics via the input matrix (**B**). The **B** matrix quantifies the effect of the actuator on the dynamics ($\dot{\mathbf{x}}$).

$$\dot{\mathbf{x}} = \mathbf{A}\mathbf{x} + \mathbf{B}u$$

If the same arbitrary dynamics have a steering wheel and rudder as actuators, they drive into the dynamics through their individual actuator gains ($\mathbf{K}_{\delta_s}$ and $\mathbf{K}_{\delta_R}$).

$$\dot{\mathbf{x}} = \mathbf{A}\mathbf{x} + \begin{bmatrix} \mathbf{K}_{\delta_S} & \mathbf{K}_{\delta_R} \end{bmatrix} \begin{bmatrix} \delta_s \\ \delta_R \end{bmatrix}$$

The virtual actuator has to combine the effect of the steering wheel and rudder on the dynamics. In order to quantify this effect, $K_{\delta_{Run}}$ is defined as the virtual actuator's gain.

$$\begin{aligned} \dot{\mathbf{x}} &= \mathbf{A}x + \begin{bmatrix} \mathbf{K}_{\delta_S} & \mathbf{K}_{\delta_R} \end{bmatrix} \begin{bmatrix} \delta_s \\ \delta_R \end{bmatrix} \\ &= \mathbf{A}x + \begin{bmatrix} \mathbf{K}_{\delta_S} & \mathbf{K}_{\delta_R} \end{bmatrix} \begin{bmatrix} M_1 \\ M_2 \end{bmatrix} \delta_{Run} \\ &= \mathbf{A}x + \left[\mathbf{K}_{\delta_{Run}}\right] \delta_{Run} \end{aligned}$$

$$\therefore \mathbf{K}_{\delta_{Run}} = \mathbf{K}_{\delta_S} M_1 + \mathbf{K}_{\delta_R} M_2 \tag{5.4.2}$$

In the above equation, $\mathbf{K}_{\delta_S}$ and $\mathbf{K}_{\delta_R}$ are the actual system variables, and will be discussed later. Now that the Mix Law has been defined, we can proceed to develop the mixing strategy.

Use of the Actuators Over Speed

Before the specific mixing is done, we will first investigate under which circumstances the actuators are best suited for use. This will give a good indication of how to mix the actuators.

Steering wheel: The effectiveness of the steering wheel is dependant on its normal force (N_s), which changes with the aircraft's speed. At low speed the aircraft does not generate much lift, allowing most of the weight to rest on the undercarriage and producing a large normal force. As speed increases, the aircraft will generate more lift, consequently reducing the normal force. As a result, the steering wheel is a good low speed actuator.

Rudder: The rudder's effectiveness is proportional to the speed of the local flow across it ($\overline{V}_{a_{\delta_R}}$). It is thus clear that the rudder is a good high speed actuator. However, if the rudder is in the engine's prop wash, $\overline{V}_{a_{\delta_R}}$ could be greater than aircraft's airspeed $\overline{V}_a$, making the rudder more effective at low ground speeds. Determining the rudder airspeed accurately is difficult to do mathematically, and placing an additional airspeed sensor at the rudder was deemed over complicated and practically irrelevant since this is not a standard measurement on actual aircraft. In order to eliminate the requirement for a rudder airspeed measurement and reduce uncertainty, the rudder is only used at high speeds where the prop wash has little effect, and $\overline{V}_{a_{\delta_R}} \simeq \overline{V}_a$.

Mixing the Actuators

Applying the reasoning from the previous section to Equation 5.4.2 and assuming the extreme case where only one actuator is used due to the severe ineffectiveness of the other, yields equations 5.4.3 and 5.4.4.

Ignoring the small effect of the rudder at low speed and not using it as an actuator, would require M_2 to be zero (Equation 5.4.3). At high speed the steering wheel's effectiveness is greatly reduced and it will not be used for actuation, thus M_1 must be zero (Equation 5.4.4).

$$\mathbf{K}_{\delta_{Run}} = \mathbf{K}_{\delta_S} M_1 \qquad (\overline{V} = slow) \tag{5.4.3}$$

$$\mathbf{K}_{\delta_{Run}} = \mathbf{K}_{\delta_R} M_2 \qquad (\overline{V} = fast) \tag{5.4.4}$$

In order to create a boundary for the conditions discussed above, two speeds are defined. U_{bend} is the $\overline{V}_g$ below which the rudder has negligible effect, compared to the steering wheel, and is not used ($M_2 = 0$). U_{fade} is the $\overline{V}_g$ above which the steering wheel has negligible effect, and is not used ($M_1 = 0$).

$$\begin{aligned} M_1 &= 0, \quad \overline{V}_g > U_{fade} \\ M_2 &= 0, \quad \overline{V}_g < U_{bend} \end{aligned} \tag{5.4.5}$$

The value of $\mathbf{K}_{\delta_{Run}}$

If we consider the arbitrary dynamics of a 1^{st} order system (shown below), $K_{\delta_{Run}}$ directly influences the open loop gain of the system. From a control point of view, it would be advantageous if $K_{\delta_{Run}}$ were a constant value. The effect of δ_{Run} on the dynamics of the system, would then be speed invariant.

$$\dot{x} = Ax + [K_{\delta_{Run}}]\,\delta_{Run}$$

The value of $K_{\delta_{Run}}$ is determined form the boundary condition where $M_1 = 1$ (and $\overline{V}_g = U_{bend}$).

$$K_{\delta_{Run}} = K_{\delta_{S_{M1}}}\Big|_{\overline{V}_g = U_{bend}} \tag{5.4.6}$$

As Take-off starts at a low speed, we will start with the low speed mixing.

Mixing M_1: At low speeds, the virtual actuator should emulate the physical low speed actuator. Thus $\delta_{Run} \simeq \delta_s$, $K_{\delta_{Run}} \simeq K_{\delta_s}$ and $M_1 \simeq 1$. A linear approach to mixing is followed between U_{bend} and U_{fade} (shown in Figure 5.20), with the constraints being,

$$M_1 = 1, \quad \overline{V}_g = U_{bend}$$
$$M_1 = 0, \quad \overline{V}_g = U_{fade}$$

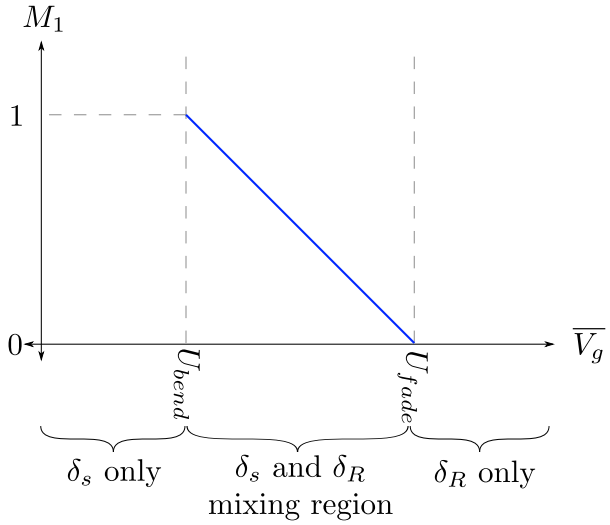

Figure 5.20: M_1 plotted against groundspeed, in the mixing region

The linear relationship between M_1 and $\overline{V}_g$ in the mixing region is derived from Figure 5.20, which is,

$$M_1 = \frac{-1}{U_{fade} - U_{bend}} \overline{V_g} + \frac{U_{fade}}{U_{fade} - U_{bend}} \tag{5.4.7}$$

With this, M_1 is summarised below as a piecewise defined function over groundspeed in Equation 5.4.8.

$$M_1 = \begin{cases} \frac{K_{\delta_{Run}}}{K_{\delta_{S_{M1}}}}, & \overline{V_g} < U_{bend} \\ \frac{-1}{U_{fade} - U_{bend}} \overline{V_g} + \frac{U_{fade}}{U_{fade} - U_{bend}}, & U_{bend} \leq \overline{V_g} \leq U_{fade} \\ 0, & \overline{V_g} > U_{fade} \end{cases} \tag{5.4.8}$$

Mixing M_2: Taking all the previous sections into account, M_2 can be determined from equations 5.4.2, 5.4.4 and 5.4.5, and is given below.

$$M_2 = \begin{cases} 0, & \overline{V}_g < U_{bend} \\ \frac{K_{\delta_{Run}} - M_1 K_{\delta_{S_{M1}}}}{K_{\delta_{R_{M2}}}}, & U_{bend} \leq \overline{V}_g \leq U_{fade} \\ \frac{K_{\delta_{Run}}}{K_{\delta_{R_{M2}}}}, & \overline{V}_g > U_{fade} \end{cases} \tag{5.4.9}$$

Now that a general solution to the Mix Law has been derived, we need to analyse the aircraft's specific parameters. The specific aircraft determines the values of K_{δ_s} and K_{δ_R}, which will be discussed in the next section. U_{bend} and U_{fade} are dependant on the values of K_{δ_s} and K_{δ_R}.

Determining the values of $\mathbf{K}_{\delta_{S_{M1}}}$ and $\mathbf{K}_{\delta_{R_{M2}}}$

The effectiveness of the actuators (or actuator gains), can be determined from the open loop state space representation of the system dynamics. Since the Mix Law is derived for the lateral runway model, the linear dynamic state space model (from Equation 5.2.5) is shown below.

$$\begin{bmatrix} \dot{\beta} \\ \dot{R} \end{bmatrix} = \begin{bmatrix} \frac{NC_{\alpha\alpha}}{mU} + \frac{\bar{q}S}{m\overline{V}_a} C_{y_\beta} & \frac{\bar{q}S}{m\overline{V}_a}\frac{b}{2\overline{V}_a} C_{y_r} - 1 \\ \frac{\bar{q}Sb}{I_z} C_{n_\beta} & \frac{l_s l_m NC_{\alpha\alpha}}{I_z U} + \frac{\bar{q}Sb}{I_z}\frac{b}{2\overline{V}_a} C_{n_r} \end{bmatrix} \begin{bmatrix} \beta \\ R \end{bmatrix} + \begin{bmatrix} \frac{NC_{\alpha\alpha}}{mU}\frac{l_m}{l} & \frac{\bar{q}S}{m\overline{V}_a} C_{y_{\delta_R}} \\ \frac{l_s l_m}{l}\frac{NC\alpha\alpha}{I_z} & \frac{\bar{q}Sb}{I_z} C_{n_{\delta_R}} \end{bmatrix} \begin{bmatrix} \delta_S \\ \delta_R \end{bmatrix} \tag{5.4.10}$$

Ignoring the dynamics to determine the effect of the actuators, Equation 5.4.10 can be written as,

$$\begin{aligned} \begin{bmatrix} \dot{\beta} \\ \dot{R} \end{bmatrix} &= \mathbf{A} \begin{bmatrix} \beta \\ R \end{bmatrix} + \begin{bmatrix} \frac{NC_{\alpha\alpha}}{mU}\frac{l_m}{l} & \frac{\bar{q}S}{mU} C_{y_{\delta_R}} \\ \frac{l_s l_m}{l}\frac{NC\alpha\alpha}{I_z} & \frac{\bar{q}Sb}{I_z} C_{n_{\delta_R}} \end{bmatrix} \begin{bmatrix} \delta_S \\ \delta_R \end{bmatrix} \\ &= \mathbf{A} \begin{bmatrix} \beta \\ R \end{bmatrix} + \begin{bmatrix} K_{\delta_{S_\beta}} & K_{\delta_{R_\beta}} \\ K_{\delta_{S_R}} & K_{\delta_{R_R}} \end{bmatrix} \begin{bmatrix} \delta_s \\ \delta_R \end{bmatrix} \end{aligned} \tag{5.4.11}$$

As there are two states, each actuator has two contributions to the dynamics of the system (represented by the amount of rows in the **B** matrix). The contribution to the β state is the lateral force that the actuator exerts on the body, while the contribution to the yaw rate (R) state is the yaw moment that the actuator produces. These actuators are designed to change the direction that the aircraft travels in, while on the runway, by changing the aircraft's heading. Since heading is the integral of yaw rate, the actuator contributions to the yaw rate state will be used as the Mix Law actuator gains.

$$K_{\delta_{S_{M1}}} = K_{\delta_{s_R}} = \frac{l_s l_m}{l}\frac{NC\alpha\alpha}{I_z}$$
$$K_{\delta_{R_{M2}}} = K_{\delta_{R_R}} = \frac{\bar{q}Sb}{I_z}C_{n_{\delta_R}} \tag{5.4.12}$$

The state space representation of the system after the Mix Law has been applied is represented as,

$$\begin{aligned}
\begin{bmatrix}\dot{\beta}\\ \dot{R}\end{bmatrix} &= \begin{bmatrix}\frac{NC_{\alpha\alpha}}{mU}+\frac{\bar{q}S}{m\overline{V}_a}C_{y_\beta} & \frac{\bar{q}S}{m\overline{V}_a}\frac{b}{2\overline{V}_a}C_{y_r}-1\\ \frac{\bar{q}Sb}{I_z}C_{n_\beta} & \frac{l_s l_m NC_{\alpha\alpha}}{I_z U}+\frac{\bar{q}Sb}{I_z}\frac{b}{2\overline{V}_a}C_{n_r}\end{bmatrix}\begin{bmatrix}\beta\\ R\end{bmatrix}+\begin{bmatrix}\frac{NC_{\alpha\alpha}}{mU}\frac{l_m}{l}M_1 & \frac{\bar{q}S}{m\overline{V}_a}C_{y_{\delta_R}}M_2\\ \frac{l_s l_m}{l}\frac{NC\alpha\alpha}{I_z}M_1 & \frac{\bar{q}Sb}{I_z}C_{n_{\delta_R}}M_2\end{bmatrix}\delta_{Run}\\
&= \begin{bmatrix}a_{11} & a_{12}\\ a_{21} & a_{22}\end{bmatrix}\begin{bmatrix}\beta\\ R\end{bmatrix}+\begin{bmatrix}b_{11_{mix}} & b_{12_{mix}}\\ b_{21_{mix}} & b_{22_{mix}}\end{bmatrix}\delta_{Run}\\
\begin{bmatrix}a_Y\\ R\end{bmatrix} &= \begin{bmatrix}\frac{NC_{\alpha\alpha}}{m}+\frac{\bar{q}S}{m}C_{y_\beta} & \frac{\bar{q}S}{m}\frac{b}{2\overline{V}_a}C_{y_r}\\ 0 & 1\end{bmatrix}\begin{bmatrix}\beta\\ R\end{bmatrix}+\begin{bmatrix}\frac{NC_{\alpha\alpha}}{m}\frac{l_m}{l}M_1 & \frac{\bar{q}S}{m}C_{y_{\delta_R}}M_2\\ 0 & 0\end{bmatrix}\delta_{Run}\\
&= \begin{bmatrix}c_{11} & c_{12}\\ 0 & 1\end{bmatrix}\begin{bmatrix}\beta\\ R\end{bmatrix}\begin{bmatrix}d_{11_{mix}} & d_{12_{mix}}\\ 0 & 0\end{bmatrix}\delta_{Run}
\end{aligned} \tag{5.4.13}$$

Choosing values for $\mathbf{U}_{bend}$ and $\mathbf{U}_{fade}$

The optimal values for U_{bend} and U_{fade} were not investigated, an intuitive selection was made instead. U_{bend} is chosen where the rudder has half the actuation gain of the steering wheel ($\frac{K_{\delta_{S_R}}}{2} = K_{\delta_{R_R}}$). U_{fade} is chosen where the rudder has double the actuation gain of the steering wheel ($2K_{\delta_{S_R}} = K_{\delta_{R_R}}$). Equations 5.4.14 and 5.4.15 give mathematical solutions of these two velocities.

$$\begin{aligned}
\frac{K_{\delta_{S_R}}}{2} &= K_{\delta_{R_R}}\\
\therefore U_{bend} &= \sqrt{\frac{2mg}{\rho S\left(C_{L_0}+C_{L_\alpha}\alpha_0+\frac{2blC_{n_{\delta_R}}}{l_s l_m C_{\alpha\alpha}}\right)}}
\end{aligned} \tag{5.4.14}$$

$$\begin{aligned}
2K_{\delta_{S_R}} &= K_{\delta_{R_R}}\\
\therefore U_{fade} &= \sqrt{\frac{2mg}{\rho S\left(C_{L_0}+C_{L_\alpha}\alpha_0+\frac{blC_{n_{\delta_R}}}{2l_s l_m C_{\alpha\alpha}}\right)}}
\end{aligned} \tag{5.4.15}$$

These selections for U_{bend} and U_{fade} were confirmed in simulation to give satisfactory results without requesting abnormally large actuator commands.

5.4.2 Controller design

The lateral runway model has shown that an aircraft's lateral dynamics during the Take-off, vary drastically with speed. Subsequently, the control problem was separated into two separate problems, low- and high speed.

The low speed controller is designed by applying TSS to the plant. This allows the faster ω_β pole to be ignored when designing the controller. The TSS assumption is not valid above velocities where $\omega_\beta \not> 5\omega_R$. A high speed controller is thus designed which takes the entire model into account.

The design specifications for these controllers are,

- Rise time under 2 seconds.
- Zero steady state errors.
- Lateral acceleration interface.

The outerloop controllers are kinematic and it would simplify the control if the innerloop controllers have an acceleration interface. State space design allows the same number of degrees of freedom as feedback gains (if all the states are observable and controllable). The two open loop poles can thus be placed arbitrarily with feedback from both lateral sensors, lateral acceleration (a_Y) and yaw rate (R). Any steady state errors are removed by implementing an integrator from the reference. A representation of such a control architecture is shown in Figure 5.21.

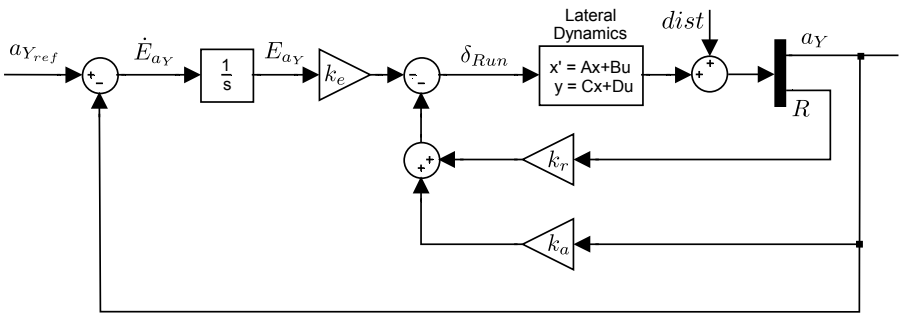

Figure 5.21: a_Y control architecture with complete control over closed loop poles

As discussed in Section 5.3.3 direct feedback from the a_Y measurement is not advisable. The acceleration gain (k_a) will thus be set to zero. Making the k_a gain zero, leaves only two degrees of freedom. Taking this into account, the low- and high speed controller designs follow.

Low Speed (Yaw Rate Controller)

At low speed, the decoupling assumption discussed in Section 5.3.1 allows the β state to be ignored from the dynamics ($\dot{\beta} = 0$). The kinematic relationship between yaw rate (R) and lateral acceleration (a_Y) will simplify to $a_Y = UR$. Due to the low groundspeed, the aircraft will have to experience high yaw rates in order to produce lateral accelerations that are larger than the lateral accelerometer's noise floor. This is not practically feasible nor desired.

Using a TSS assumption, the side slip dynamics can be ignored and a pure yaw rate controller is designed for low speeds Acceleration is determined from the kinematic steady state relationship ($a_Y = UR$). The yaw rate gyro can be combined with velocity to measure steady state acceleration, and produce a measurement with less noise (since gyros typically have a lower noise floor than accelerometers).

The simplified lateral plant is shown in Equation 5.4.16, with the controller architecture used is shown in Figure 5.22. This architecture allows full control over the two closed loop poles, which can be placed anywhere as long as the closed loop frequency (ω_{CL}) does not violate time scale separation ($\omega_{CL} < 5\omega_\beta$) and too much control effort is not used. The simplified open loop plant, controller architecture and control law are shown below.

$$\begin{aligned} \dot{R} &= \left[\frac{l_s l_m N C_{\alpha\alpha}}{I_z U} + \frac{\bar{q}Sb}{I_z}\frac{b}{2\bar{V}_a}C_{n_r}\right] R + \left[\frac{l_s l_m}{l}\frac{NC_{\alpha\alpha}}{I_z}M_1 \quad \frac{\bar{q}Sb}{I_z}C_{n_{\delta_R}}M_2\right]\delta_{Run} \\ &= \left[a_{22}\right] R + \left[b_{21_{mix}} \quad b_{22_{mix}}\right]\delta_{Run} \\ R &= \left[1\right] R + \left[0\right]\delta_{Run} \end{aligned} \tag{5.4.16}$$

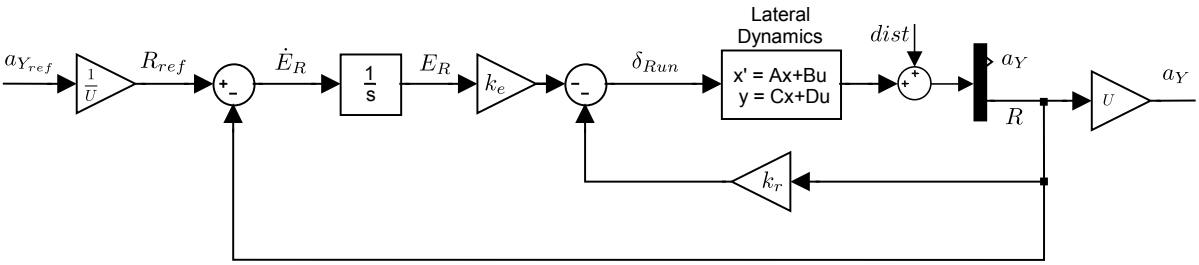

Figure 5.22: Low speed runway a_Y controller architecture

$$\begin{aligned} \delta_{Run} &= -\left(k_e E_R + k_r R\right) \\ \dot{E}_R &= \frac{a_{Y_{ref}}}{U} - R \end{aligned} \tag{5.4.17}$$

Closed loop solution

Using the control law from Equation 5.4.17, the closed loop state space form of this controller is,

$$\begin{aligned} \begin{bmatrix} \dot{R} \\ \dot{E_{a_Y}} \end{bmatrix} &= \begin{bmatrix} a_{22} - k_r b_{21_{mix}} & -k_e b_{21_{mix}} \\ -1 & 0 \end{bmatrix}\begin{bmatrix} R \\ E_{a_Y} \end{bmatrix} + \begin{bmatrix} 0 \\ 1 \end{bmatrix} R_{ref} \\ a_Y &= \begin{bmatrix} \frac{1}{U} & 0 \end{bmatrix}\begin{bmatrix} R \\ E_{a_Y} \end{bmatrix} + \begin{bmatrix} 0 \end{bmatrix} R_{ref} \end{aligned} \tag{5.4.18}$$

The closed loop characteristic equation is,

$$\begin{aligned} s_{CL} &= s^2 + (k_r b_{21_{mix}} - a_{22})\, s - k_e b_{21_{mix}} \\ &= s^2 + \alpha_1 s + \alpha_0 \end{aligned} \tag{5.4.19}$$

Controller gains

Using Equation 5.4.19, the controller gains used to realise the closed loop poles are,

$$\begin{aligned} k_e &= -\frac{\alpha_0}{b_{21_{mix}}} \\ k_r &= \frac{\alpha_1 + a_{22}}{b_{21_{mix}}} \end{aligned} \tag{5.4.20}$$

Pole placement

The placement of the yaw rate poles are critical to the overall lateral position response of the aircraft while on the runway, as the outerloop poles cannot be placed at a faster frequency than the innerloop. Since the low speed lateral controller is used during taxi to line up the aircraft on the runway, the dominant closed loop frequency has to be maximised.

The closed loop poles are placed as an over damped complex pole pair at the same frequency as the open loop poles (with frequency = ω_R and damping = ζ_R). This placement is shown in Figure 5.23. The desired closed loop pole positions and characteristic equation is thus,

$$\omega_R = \frac{l_s l_m N C_{\alpha\alpha}}{I_z U} + \frac{\bar{q} S b}{I_z} \frac{b}{2\overline{V}_a} C_{n_r}$$

$$\begin{aligned} \zeta_R &= 0.8 \\ \therefore s_{CL} &= s^2 + (2\zeta_R \omega_R)\, s + \omega_R^2 \end{aligned}$$

Step response (Root Locus)

Figure 5.24 shows the linear step response of the low speed controller at 5 m/s. The two step responses shown are of the same controller, but applied to both the simplified 1^{st} order plant and the coupled plant. It is clear that the controller satisfies the design specifications without violating the TSS assumptions.

High Speed (Lateral Acceleration Controller)

At higher speeds, the assumption that the side slip dynamics can be ignored, is no longer valid and the full model has to be used. The architecture in figure 5.21 is used, with $k_a = 0$. This forms a classical rate loop, encapsulated by the acceleration integrator (shown in Figure 5.26). The control law is shown in Equation 5.4.21. The yaw rate gain (k_r) will be used to control the damping of the rate loop (ζ_{a_Y}).

The closed loop root locus is influenced by the presence of the rate zero close to the ω_β pole, and with this control architecture a wide spectrum of damping is not possible. A specific

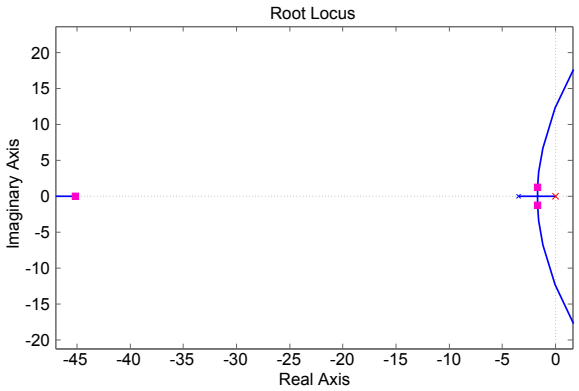

Figure 5.23: Root locus of innerloop low speed runway lateral controller (at 5m/s)

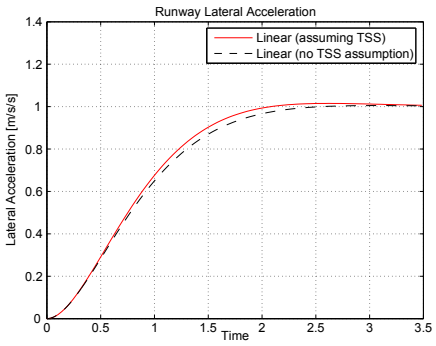

Figure 5.24: Linear step response of innerloop low speed runway lateral controller (at 5m/s)

closed loop rate damping cannot always be achieved, as can be seen by the root loci shown in Figure 5.25.

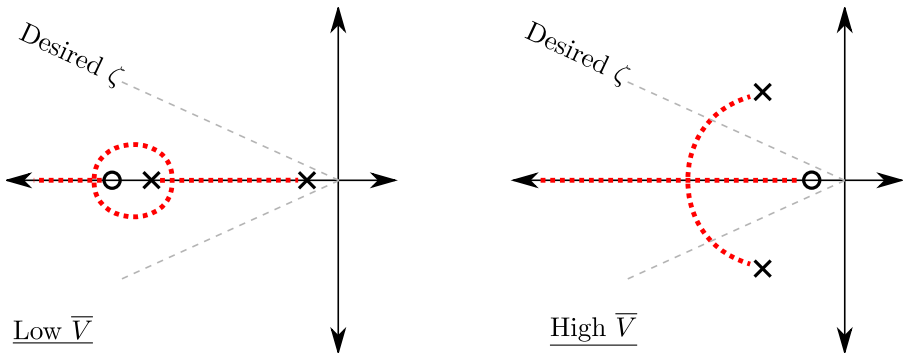

Figure 5.25: Limitations on the desired ζ, due to root locus shape at low and high speeds.

Thus a practically intuitive value for k_r is determined (in the following section) and the damping of the rate closed loop is calculated. Should the calculated damping be less than the desired damping (ζ_{a_Y}), k_r will be determined mathematically. The control law and architecture are shown in Equation 5.4.21 and Figure 5.26.

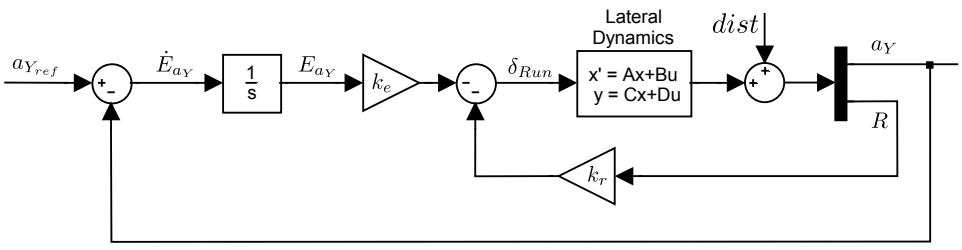

Figure 5.26: High speed runway a_Y controller architecture

$$\begin{aligned} \delta_{Run} &= -\left(k_e E_R + k_r R\right) \\ \dot{E}_{a_Y} &= a_{Y_{ref}} - a_Y \end{aligned} \tag{5.4.21}$$

Calculating k_r (practical)

Initially a practical actuator deflection to dampen a 10°/s yaw rate is determined by analysing the system's natural damping to yaw rate disturbances. By decoupling the side slip state, this damping is the a_{22} element from the state space model. Taking the effectiveness of the virtual actuator into consideration, the value for the k_r gain is,

$$\begin{aligned} k_r &= \frac{a_{22}}{10 b_{21_{mix}}} \\ &= \frac{\frac{l_s l_m N C_{\alpha\alpha}}{I_z U} + \frac{\bar{q} S b}{I_z} \frac{b}{2\overline{V}_a} C_{n_r}}{10 \left(\frac{l_s l_m}{l} \frac{N C_{\alpha\alpha}}{I_z} M_1 + \frac{\bar{q} S b}{I_z} C_{n_{\delta_R}} M_2 \right)} \end{aligned} \tag{5.4.22}$$

The closed loop pole position of the yaw rate feedback loop is determined with Equation 5.4.25, and it is checked that the damping is at least ζ_{a_Y}. If it is not, the gain is recalculated using a mathematical pole placement approach.

Calculating k_r (mathematical)

$$\begin{aligned} k_r &= \frac{-b_{tmp} - \sqrt{b_{tmp}^2 - 4 a_{tmp} c_{tmp}}}{2 a_{tmp}} \\ \text{with,} \quad a_{tmp} &= b_{21_{mix}}^2 \\ b_{tmp} &= 4 \zeta_{a_Y}^2 \left(a_{11} b_{21_{mix}} - a_{21} b_{11_{mix}} \right) - 2 b_{21_{mix}} \left(a_{11} + a_{22} \right) \\ c_{tmp} &= \left(a_{11} + a_{22} \right)^2 + 4 zeth a_{a_Y}^2 \left(a_{12} a_{21} - a_{11} a_{22} \right) \end{aligned} \tag{5.4.23}$$

$$\begin{bmatrix} \dot{\beta} \\ \dot{R} \end{bmatrix} \begin{bmatrix} a_{11} & a_{12} - k_r b_{11_{mix}} \\ a_{21} & a_{22} - k_r b_{21_{mix}} \end{bmatrix} \begin{bmatrix} \beta \\ R \end{bmatrix} + \begin{bmatrix} -b_{11_{mix}} \\ -b_{21_{mix}} \end{bmatrix} R_{ref} \tag{5.4.24}$$

Equation 5.4.24 shows the closed loop rate plant. Determining the closed loop rate damping and frequency (if the closed loop poles are complex),

$$\begin{aligned} \zeta_{a_Y} &= \frac{b_{tmp}}{2\omega_n} \\ \omega_{c_{a_Y}} &= \frac{k_r b_{21_{mix}} - a_{11} - a_{22}}{2\zeta_{a_Y}} \end{aligned}$$

$$\begin{aligned} \omega_n &= \frac{\sqrt{b_{tmp}^2 + \left| d_{tmp} \right|}}{2} \\ \text{with,} \quad b_{tmp} &= k_r b_{21_{mix}} - a_{22} - a_{11} \\ c_{tmp} &= a_{11} \left(a_{22} - k_r b_{21_{mix}} \right) + a_{21} \left(k_r b_{11_{mix}} - a_{12} \right) \\ d_{tmp} &= b_{tmp}^2 - 4 c_{tmp} \end{aligned} \tag{5.4.25}$$

Calculating k_e

Finally the integrator gain is calculated, which determines the frequency of the dominant integrator pole (ω_I). The maximum frequency at which the integrator pole ($\omega_{I_{max}}$) can be placed accurately, has been determined empirically to be three times slower than the closed loop yaw rate poles ($\omega_{I_{max}} = \frac{w_{c_{a_Y}}}{3}$). It is possible to place the integrator pole at a higher frequency, but this requires aircraft specific design over a variety of speeds, which is complex and not very robust.

$$
\begin{aligned}
k_e &= \omega_I \frac{A_{4_{tmp}} - A_{1_{tmp}}\omega_I + \omega_I^2}{A_{5_{tmp}} - A_{3_{tmp}}\omega_I - A_{2_{tmp}}\omega_I^2} \\
\text{with,} \quad & \\
& A_{1_{tmp}} = k_r b_{21_{mix}} - a_{11} - a_{22} \\
& A_{2_{tmp}} = d_{11_{mix}} \\
& A_{3_{tmp}} = (a_{11} + a_{22})\, d_{11_{mix}} - b_{11_{mix}} c_{11} - b_{21_{mix}} c_{12} \\
& A_{4_{tmp}} = a_{11}a_{22} - a_{12}a_{21} + k_r \left(a_{21} b_{11_{mix}} - a_{11} b_{21_{mix}}\right) \\
& A_{5_{tmp}} = \left(a_{22} b_{11_{mix}} - a_{12} b_{21_{mix}}\right) c_{11} + \left(a_{11} b_{21_{mix}} - a_{21} b_{11_{mix}}\right) c_{12} \\
& + \left(a_{12}a_{21} - a_{11}a_{22}\right) d_{11_{mix}}
\end{aligned}
\tag{5.4.26}
$$

Closed Loop solution

The closed loop solution to this controller is,

$$
\begin{aligned}
\begin{bmatrix} \dot{\beta} \\ \dot{R} \\ \dot{E_{a_Y}} \end{bmatrix} &= \begin{bmatrix} a_{11} & a_{12} - k_r b_{11_{mix}} & -k_e b_{11_{mix}} \\ a_{21} & a_{22} - k_r b_{21_{mix}} & -k_e b_{21_{mix}} \\ -c_{11} & k_r d_{11_{mix}} - c_{12} & k_e d_{11_{mix}} \end{bmatrix} \begin{bmatrix} \beta \\ R \\ E_{a_Y} \end{bmatrix} + \begin{bmatrix} 0 \\ 0 \\ 1 \end{bmatrix} a_{Y_{ref}} \\
a_Y &= \begin{bmatrix} c_{11} & c_{12} - k_r d_{11_{mix}} & -k_e d_{11_{mix}} \end{bmatrix} \begin{bmatrix} \beta \\ R \\ E_{a_Y} \end{bmatrix} \begin{bmatrix} 0 \end{bmatrix} a_{Y_{ref}}
\end{aligned}
\tag{5.4.27}
$$

Pole placement

The closed loop damping (ζ_{a_Y}) is set high to avoid overshoot should there be unmodelled delays. The closed loop frequency is set in terms of the open loop plant. The resulting root locus for two different speeds is shown in Figure 5.27.

$$
\begin{aligned}
\zeta_{a_Y} &= 0.8 \\
\omega_{I_{max}} &= \frac{w_{c_{a_Y}}}{3}
\end{aligned}
$$

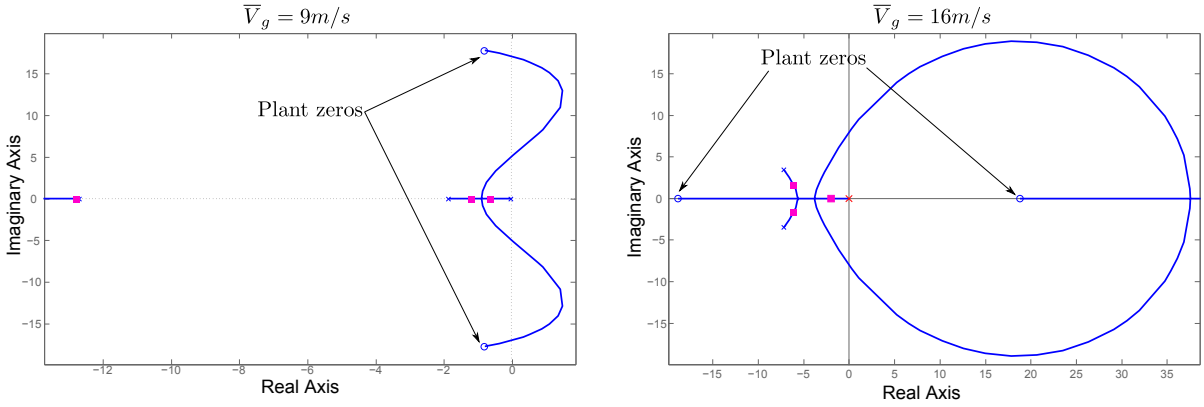

Figure 5.27: Root locus of innerloop high speed runway lateral controller (at 9 and 16 m/s)

Step response

The step responses of the controller is shown at two speeds in Figure 5.28. It is clear that the desired rise time cannot be met. This is due to the plant's low open loop bandwidth. The controller architecture that is designed to reduce noise from the accelerometer measurements, does not allow the increase of closed loop frequency that will allow the desired rise time to be achieved.

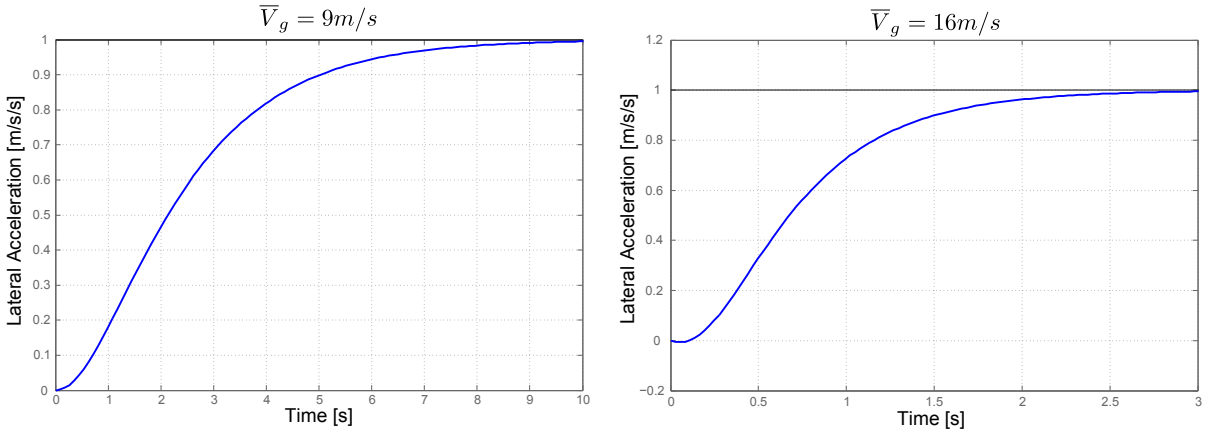

Figure 5.28: Linear step response of innerloop high speed runway lateral controller (at 9 and 16 m/s)

5.5 Lateral Runway Guidance Controller

The runway guidance controller has to ensure that the aircraft does not veer off the runway while it accelerates up to $\overline{V}_r$. The acceleration interface of the innerloop control allows a kinematic controller to be designed for lateral guidance.

To simplify the controller design, the aircraft is modelled as a point mass that can generate any required acceleration across the width of the runway (B_T). Velocity ($\dot{y}_T$) and position (y_T) control thus become a 1D design problem, with $y_T = 0$ when the aircraft is in the centre of the runway. The difference in heading between the runway centreline and the aircraft, is quantified by the heading angle ψ_R. Figure 5.29 shows a graphical representation.

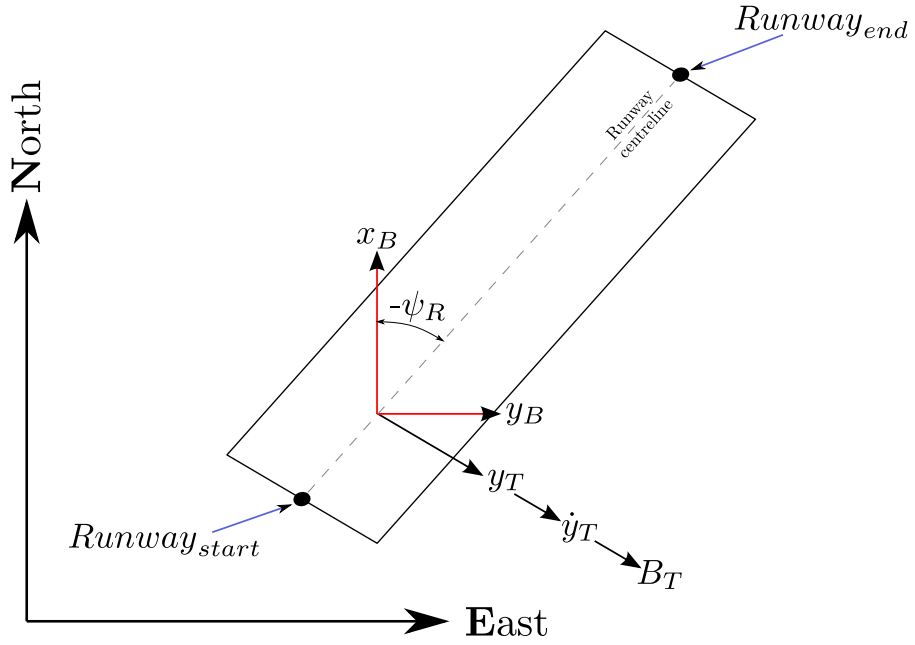

Figure 5.29: Runway Navigation

The largest concern while designing this controller is the closed loop frequency of the $\dot{y}_T$ controller. Assuming that the aircraft is travelling at a constant speed, $\dot{y}_T$ is equivalent to the aircraft's heading. Should the aircraft's heading change, it could veer off the runway. It is thus essential to be able to control heading ($\dot{y}_T$) as fast a possible. The guidance controller design is thus separated into lateral velocity and position controllers.

The runway guidance controllers will take the innerloop dynamics into account. This way the lateral velocity closed loop poles can be placed at higher frequencies. As shown in Section 5.3, the innerloop closed loop poles are very sensitive to changes in speed. A single off-line controller design is thus not possible. A generalised control strategy is followed that designs the lateral controllers in terms of the innerloop.

5.5.1 Converting B_T to a_Y accelerations

Converting B_T to a_Y accelerations, requires a DCM that is only rotated through a heading angle of ψ_R. We assume that axial body acceleration does not contribute to B_T and thus the conversion becomes a simple trigonometric relationship.

$$a_Y = \frac{B_T}{\cos(\phi_R)} \tag{5.5.1}$$

5.5.2 Lateral Velocity Control

The controller architecture that was empirically found to produce the fastest closed loop poles for this system, is a lead network. There is a low- and high speed innerloop plant, but the same control architecture is used for both. Since there will be multiple poles, only the dominant real pole's position will be controlled.

Low speed

A discrete implementation of the lead network controller is used as it does not require derivatives of signals (that can potentially be noisy). The transfer function and discrete representation of control law is shown below,

$$\begin{aligned} \frac{B_{T_{ref}}}{\dot{y}_{T_{ref}} - \dot{y}_T} &= k_v \frac{s + \omega_{zero}}{s + \omega_{pole}} \\ B_{T_{ref}}(k) &= \left(1 - T_s\omega_{pole}\right) B_{T_{ref}}(k-1) + k_v \left(T_s\omega_{zero} - 1\right) e_{dot}(k-1) + k_v e_{dot}(k) \\ \text{where,} \quad e_{dot}(k) &= \dot{y}_{T_{ref}}(k) - \dot{y}_T(k) \end{aligned} \tag{5.5.2}$$

Taking the inner closed loop dynamics designed for in Section 5.4.2 into account, the control architecture is shown in Figure 5.30.

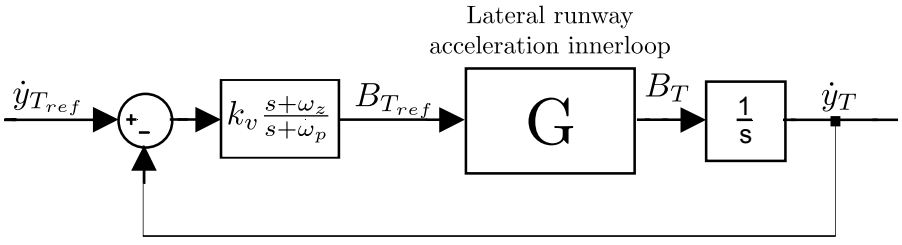

Figure 5.30: Lateral runway velocity lead network controller architecture

The closed innerloop controller poles (frequency = $\omega_{\dot{y}_T}$, damping = $\zeta_{\dot{y}_T}$) have a characteristic equation of,

$$\begin{aligned} s_{CL} &= s^2 + \left(2\zeta_{\dot{y}_T}\omega_{\dot{y}_T}\right) s + \omega_{\dot{y}_T}^2 \\ &= s^2 + \alpha_1 s + \alpha_0 \end{aligned}$$

The zero and pole position are specified in terms of the closed loop characteristic equation. The controller gain is calculated below to place a single dominant velocity pole (ω_{vel}), but is only valid as long as the maximum pole frequency is not exceeded.

$$\begin{aligned} \omega_{pole} &= \omega_c \\ \omega_{zero} &= 0.75\omega_c \\ k_v &= \frac{\omega_{vel}\left(\omega_{pole}-\omega_{vel}\right)\left(\alpha_0-\alpha_1\omega_{vel}+\omega_{vel}^2\right)}{\alpha_0\left(\omega_{zero}-\omega_{vel}\right)} \\ \text{as long as,}\quad \omega_{vel} &\leq 0.5\omega_c \end{aligned} \tag{5.5.3}$$

Pole placement The closed loop velocity pole is placed as fast as possible, and shown below,

$$\therefore \omega_{vel} = 0.5\omega_c \tag{5.5.4}$$

The resulting closed loop root locus and step response at 5 m/s is shown in Figure 5.31.

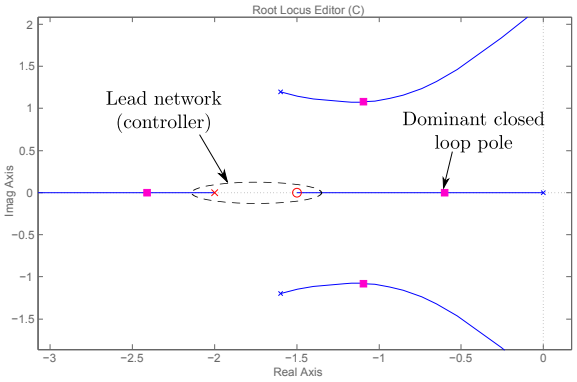

Figure 5.31: Lateral TSS runway velocity lead network velocity controller root locus (5m/s forward velocity)

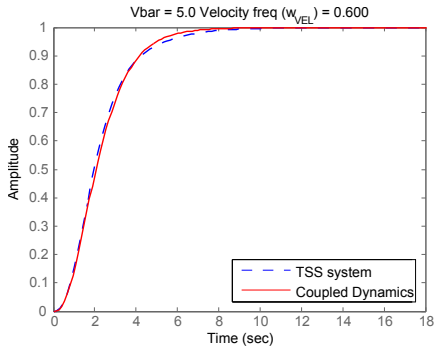

Figure 5.32: Lateral TSS runway velocity lead network velocity controller step response (5m/s forward velocity)

Step response Figure 5.32 shows the step response of this controller. The controller was also applied to the 2-DOF plant to show that the TSS assumption is valid.

High speed

The same control architecture is used for the high speed plant. The controller gain calculations, zero- and pole locations change slightly, since there is a third pole that has to be taken into account. The discrete control law remains the same as for the low speed controller (Equation 5.5.2).

Taking the closed innerloop dynamics designed for in Section 5.4.2 into account, the control architecture remains the same as for the low speed case and is shown in Figure 5.30.

Using the symbols defined in Equation 5.4.13, the closed innerloop controller poles have a characteristic equation of,

$$\begin{aligned} s_{CL} &= s^3 + \alpha_2 s^2 + \alpha_1 s + \alpha_0 \\ \text{where,}\quad \alpha_2 &= k_r b_{21_{mix}} - a_{11} - a_{22} - k_e d_{11_{mix}} \\ \alpha_1 &= a_{11}a_{22} - a_{12}a_{21} + k_r \left(a_{21} b_{11_{mix}} - a_{11} b_{21_{mix}}\right) \\ &+ k_e \left[\left(a_{11} + a_{22}\right) d_{11_{mix}} - b_{11_{mix}} c_{11} - b_{21_{mix}} c_{12}\right] \\ \alpha_0 &= k_e \left[\begin{array}{l} \left(a_{22} b_{11_{mix}} - a_{12} b_{21_{mix}}\right) c_{11} \\ + \left(a_{11} b_{21_{mix}} - a_{21} b_{11_{mix}}\right) c_{12} \\ + \left(a_{12}a_{21} - a_{11}a_{22}\right) d_{11_{mix}} \end{array}\right] \end{aligned}$$

The controller gain is calculated below to place a single dominant velocity pole (ω_{vel}) in terms of the innerloop integrator pole (ω_I), but is only valid as long as the maximum pole frequency is not exceeded.

$$\begin{aligned} \omega_{pole} &= 2.2\omega_I \\ \omega_{zero} &= 0.8\omega_I \\ k_v &= \frac{\omega_{vel}\left(\omega_{pole} - \omega_{vel}\right)\left(\alpha_0 - \alpha_1\omega_{vel} + \alpha_2\omega_{vel}^2 - \omega_{vel}^3\right)}{\alpha_0\left(\omega_{zero} - \omega_{vel}\right)} \\ \text{as long as,}\quad \omega_{vel} &\leq 0.64\omega_I \end{aligned} \tag{5.5.5}$$

Pole placement The closed loop velocity pole is placed as fast as possible, and shown below,

$$\omega_{vel} = 0.64\omega_I \tag{5.5.6}$$

The resulting closed loop root locus at two different speeds is shown in Figure 5.33.

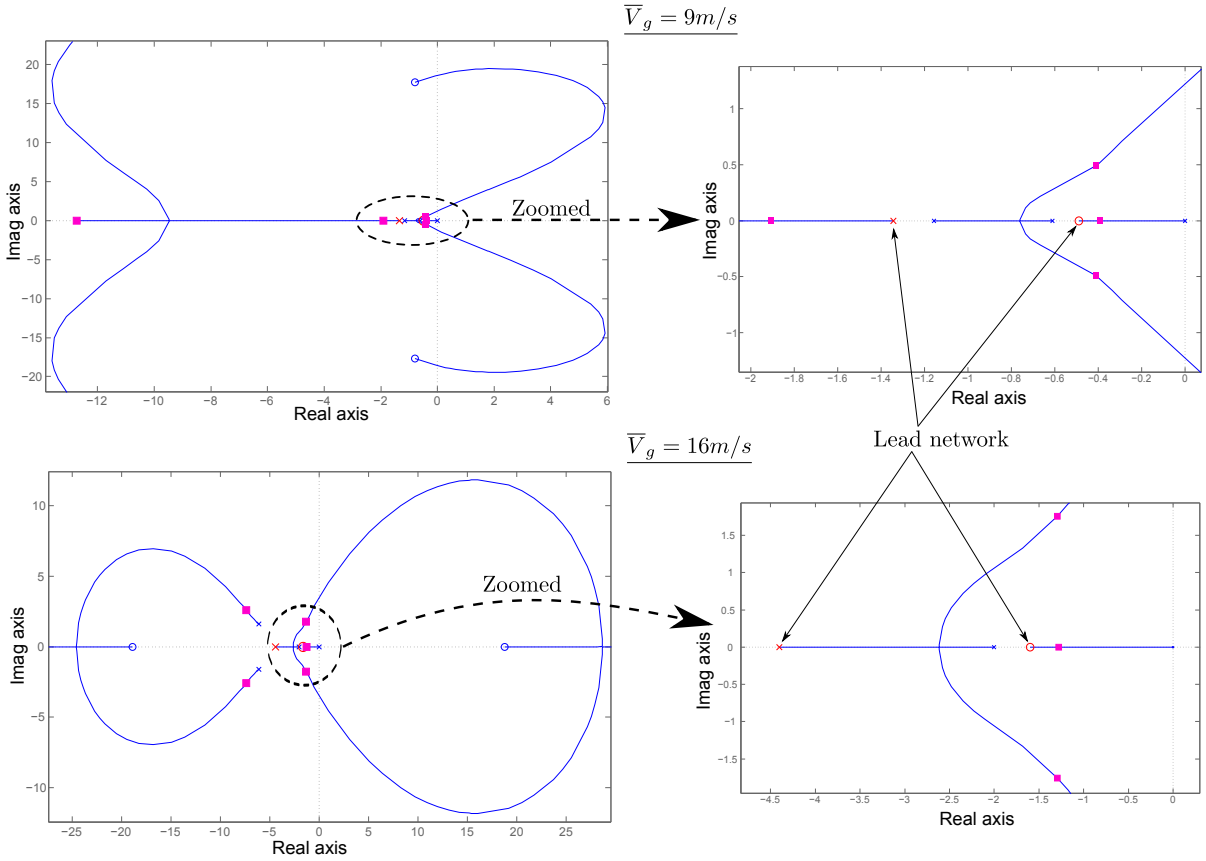

Figure 5.33: Lateral high speed runway velocity lead network velocity controller root locus (9 and 16 m/s forward velocity)

Step response Figure 5.34 shows the step response at 16 m/s.

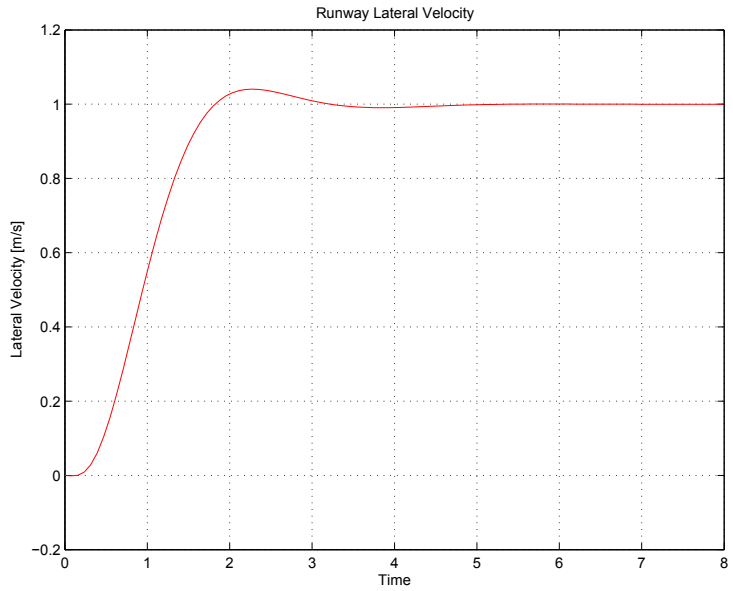

Figure 5.34: Lateral high speed runway velocity lead network velocity controller step response (16 m/s forward velocity)

5.5.3 Lateral Position Control

The lateral position (y_T) loop is now closed around the lateral velocity loop to ensure that the aircraft remains on the runway during the Groundroll phase. Since there are no position disturbances present on the runway, a proportional controller will suffice.

At low speeds, the lateral position controller is used to line the aircraft up with the runway before acceleration. A high closed loop frequency is needed to ensure that the aircraft does not use a large proportion of the runway to line its self up. At higher speeds a high closed loop frequency for the lateral position controller is not required as most of the disturbances will be countered by the lateral acceleration and -velocity controllers.

The lateral position controller gain will be designed by applying TSS assumptions to the innerloop dynamics. Only the velocity controller's closed loop poles will be taken into account. The two controllers use the same control architecture, thus the control law for both is defined as,

$$\dot{y}_{T_{ref}} = k_p \left(y_{T_{ref}} - y_T \right) \tag{5.5.7}$$

Thus the control architecture is also the same.

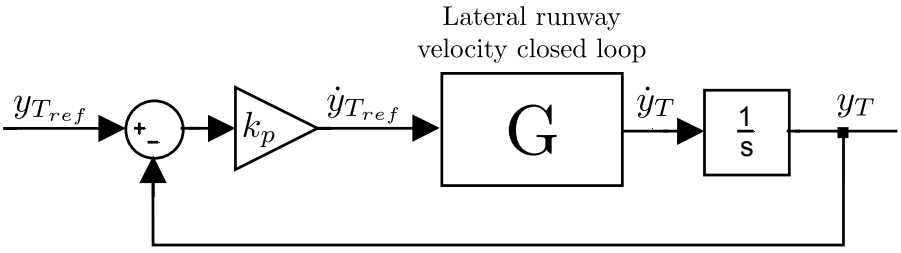

Figure 5.35: Runway lateral position controller architecture

The difference between the two controllers is the velocity closed loop system used to calculate the controller gain. A single dominant position pole (ω_{pos}) will be placed.

Low speed

The controller gain calculation and the maximum frequency that the position pole can accurately be placed, is shown below. The position pole is placed at its maximum allowable frequency.

$$k_p = \frac{\begin{bmatrix} w_{pos} k_v w_{zero} w_c^2 - w_{pos}^2 \left(w_{pole} w_c^2 + k_v w_c^2 \right) \\ + w_{pos}^2 \left(w_c^2 + 2 w_{pole} \zeta w_c \right) - w_{pos}^4 \left(2\zeta w_c + w_{pole} \right) + w_{pos}^5 \end{bmatrix}}{k_v w_{zero} w_c^2 - w_{pos} k_v w_c^2} \tag{5.5.8}$$

as long as, $\omega_{pos} \leq 0.4 \omega_{vel}$

The closed loop root locus and step response at 5 m/s is shown in Figure 5.36.

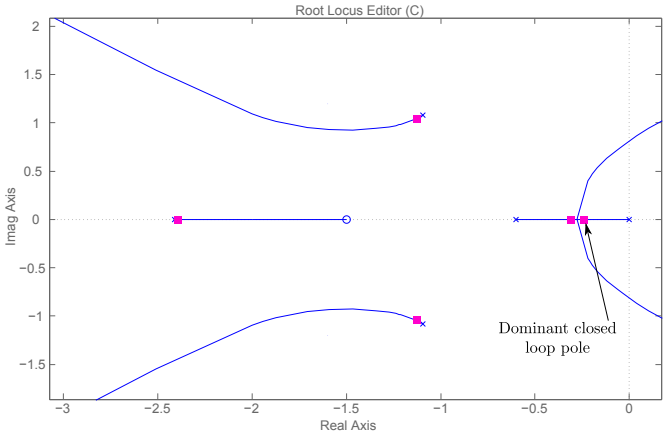

Figure 5.36: Lateral TSS runway position controller root locus (5 m/s forward velocity)

Step response The step response at 1 m/s and 5 m/s is shown in Figure 5.37.

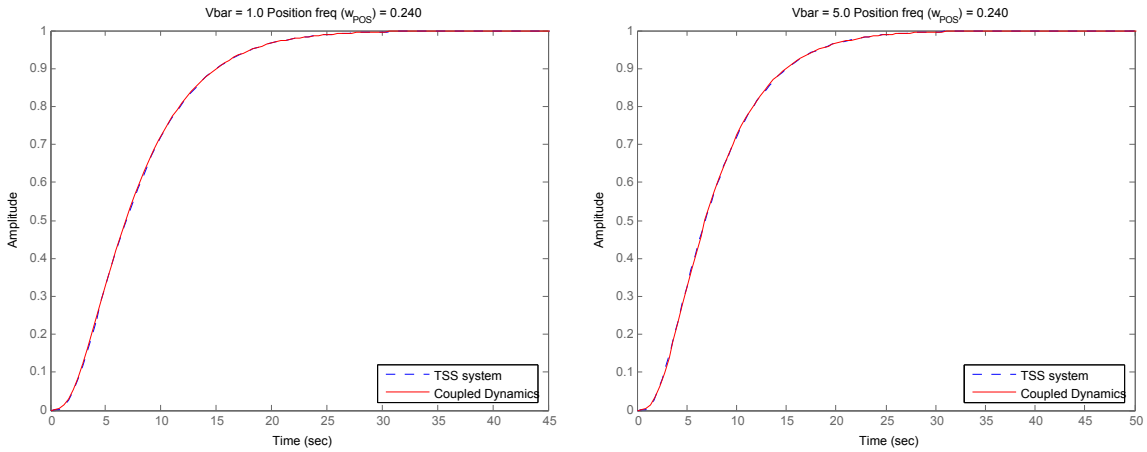

Figure 5.37: Low speed lateral TSS runway position controller step response (1 m/s and 5 m/s forward velocity)

High speed

The controller gain calculation and the maximum frequency that the position pole can accurately be placed, is shown below. The position pole is placed at its maximum allowable frequency.

$$k_p = \frac{\left[\begin{array}{c} w_{pos}w_{zero}k_v\alpha_0 - w_{pos}^2\left(\alpha_0 w_{pole} + k_v\alpha_0\right) + w_{pos}^3\left(\alpha_0 + \alpha_1 w_{pole}\right) \\ -w_{pos}^4\left(\alpha_1 + \alpha_2 w_{pole}\right) + w_{pos}^5\left(\alpha_2 + w_{pole}\right) - w_{pos}^6 \end{array}\right]}{k_v\alpha_0 w_{zero} - w_{pos}k_v\alpha_0} \tag{5.5.9}$$

as long as,$\omega_{pos} \leq 0.5\omega_{vel}$

The closed loop root locus and step response at two different speeds are shown in Figure 5.38.

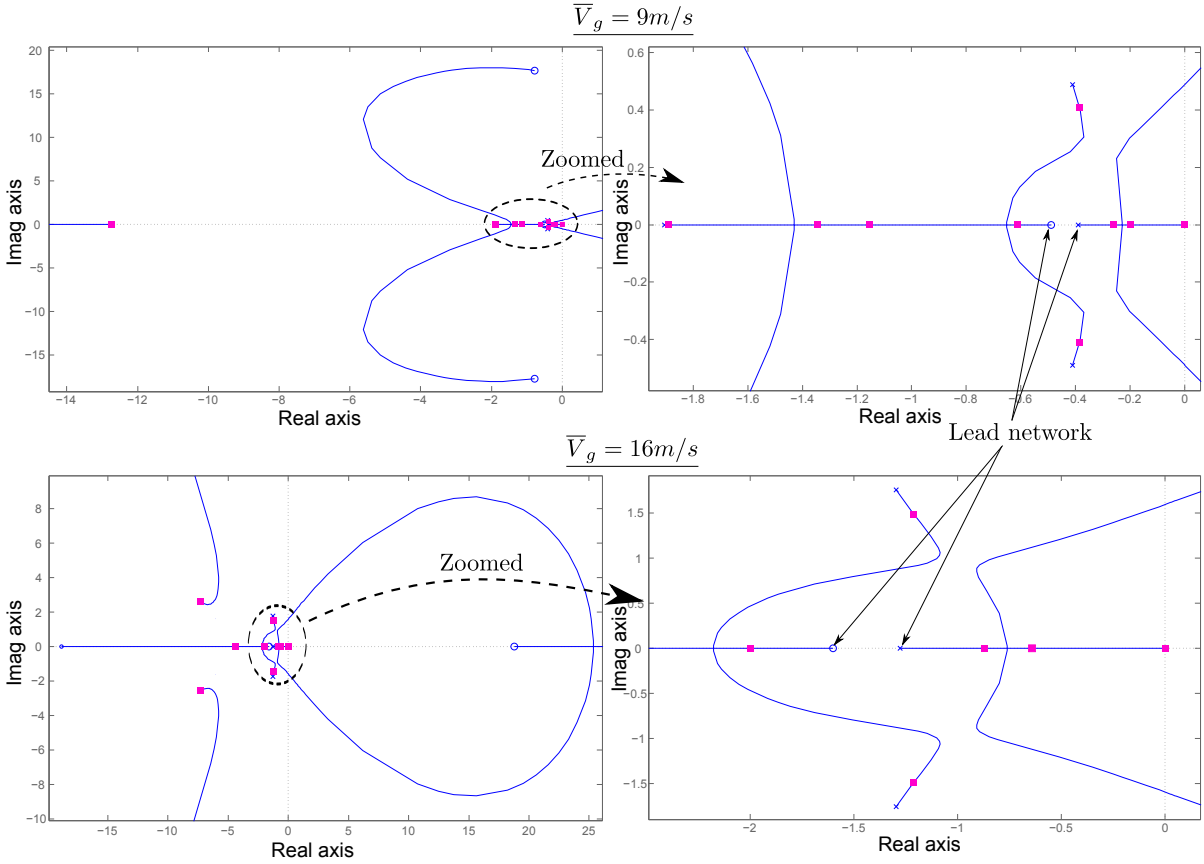

Figure 5.38: Lateral high speed runway position controller root locus (9 and 16 m/s forward velocity)

Step response The step response at 16 m/s is shown in Figure 5.39.

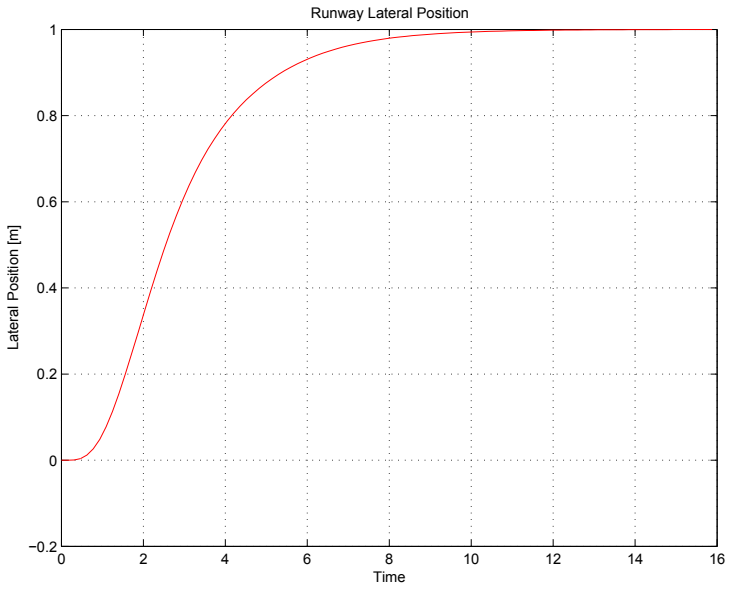

Figure 5.39: Lateral high speed runway position controller step response (16 m/s forward velocity)

5.6 Take-off path

The Take-off path has to be defined so that the lateral control can be applied. Two points are specified to describe the position and orientation of a runway in Earth axis (see Figure 5.29). These are,

- Start of runway ($Runway_{start}$)
- End of runway ($Runway_{end}$)

Figure 5.29 shows how these two points are used to define the heading of the runway (centreline). y_T will then describe the aircraft's perpendicular distance from the runway's centre line, or cross track position of the aircraft on the runway.

5.7 Summary

The aircraft's lateral position on the runway can now be controlled to ensure it remains on the runway during the Groundroll phase. It is not advised to keep this controller active while in the air as it does not take the aircraft's roll into account.

All the controllers described in Chapter 2 to implement Take-off, have been designed. The functionality of these controllers will be combined and tested in a full non-linear simulation environment. The results of these simulations are detailed in Chapter 6.

Chapter 6

Take-off Simulation

All the Take-off controllers are now combined to produce an autonomous Take-off system. To reduce risk to hardware and increase confidence in the system, a full non-linear Hardware In the Loop (HIL) simulation is set up in MATLAB. Practical sensor noise and wind disturbances are included in this simulation. The results of this simulation is shown in this chapter. Each controller's results are discussed individually to show its operation.

Two sets of Take-off simulations are run to test the performance of the different lateral acceleration controllers. The aircraft is placed in the centre of the runway with a 10° heading offset, before the simulation is started.

6.1 Throttle

Groundspeed

It is apparent in Figure 6.1 that the groundspeed is not tracked perfectly. As mentioned in Section 4.1.3 steady state errors are not catered for by the groundspeed controller.

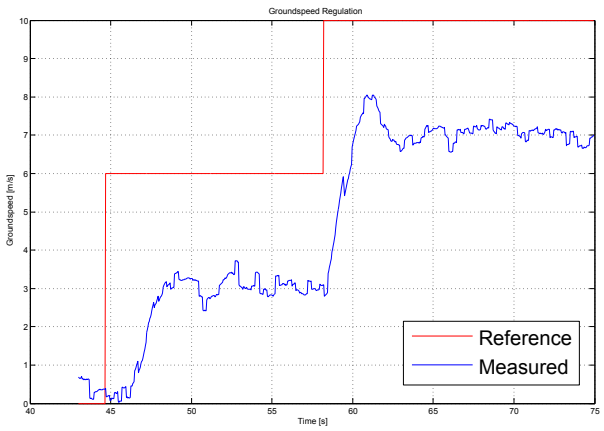

Figure 6.1: Simulated runway groundspeed regulation

Throttle ramp

Figure 6.2 shows the non-linear response to the throttle ramp. The groundspeed controller is initially engaged and the throttle ramp is engaged at 79.7 seconds. Once the throttle ramp starts, the axial acceleration increases quickly.

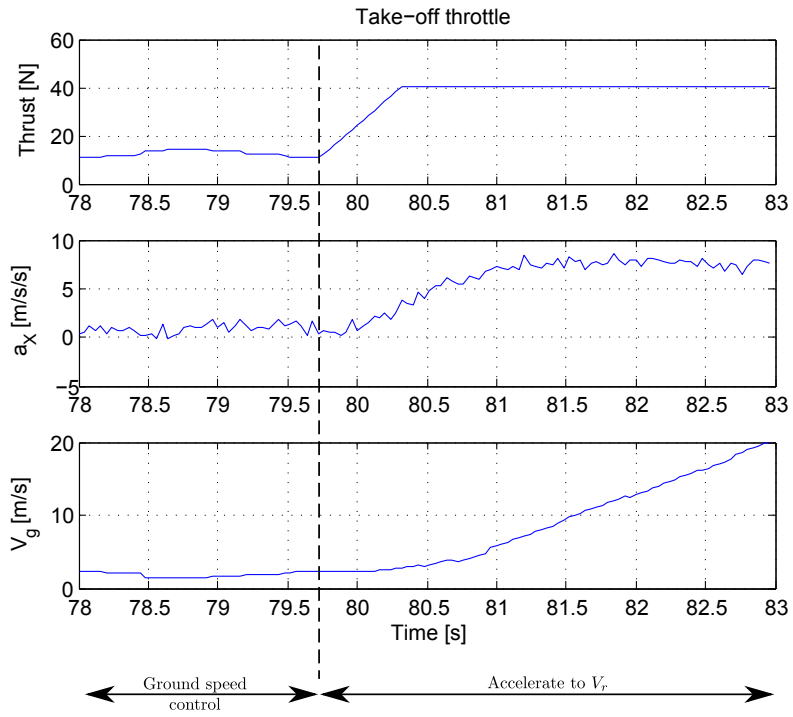

Figure 6.2: Simulated runway axial acceleration

6.2 Runway lateral position

Yaw rate controller

Figure 6.3 shows the position of the aircraft while it is in contact with the runway. The initial heading offset is countered before the aircraft accelerates, however the wind disturbance from the West causes the aircraft to veer to the right of the runway. It is clear that once the aircraft's speed increases, it does not alter course. Should the wind cause a large disturbance at low speeds, this could cause the aircraft depart the runway before rotation.

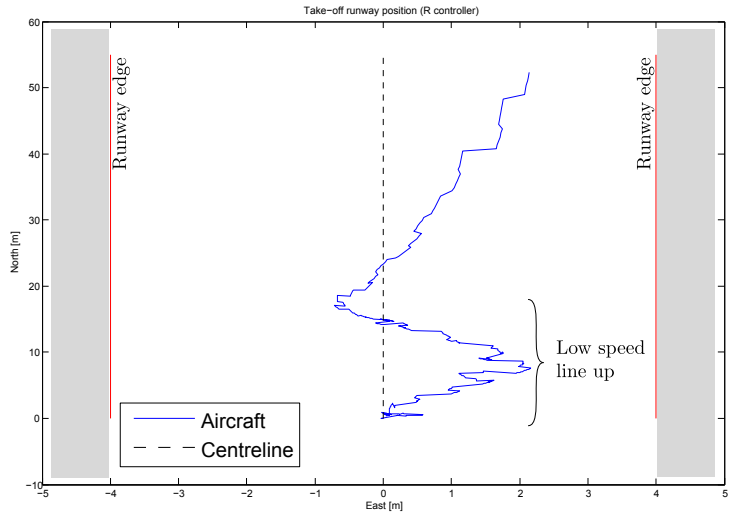

Figure 6.3: Simulated runway lateral position: Yaw rate control (with wind)

Lateral acceleration controller

Figure 6.2 shows the aircraft's heading offset is corrected. Once it accelerates down the runway, the position is corrected by altering the aircraft's heading.

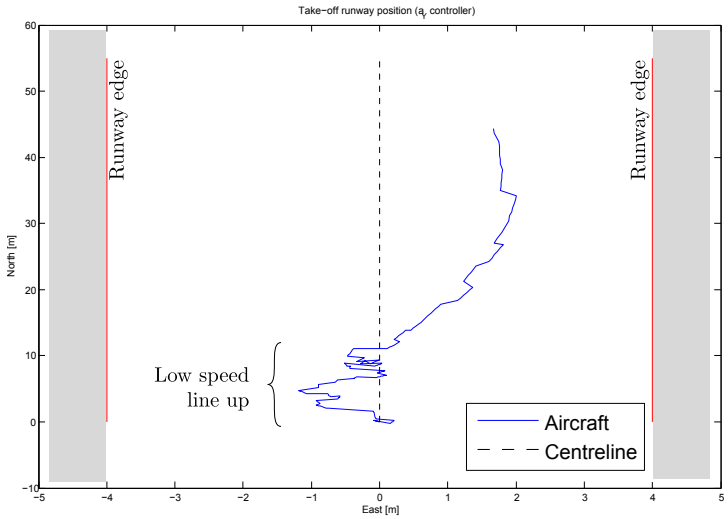

Figure 6.4: Simulated runway lateral position: Lateral acceleration control (with wind)

6.3 Runway Pitch Controller

During the first part of the Groundroll, only the pitch rate damper is active. As soon as $\overline{V}_r$ is reached, the pitch angle controller is engaged to rotate the aircraft and make it airborne.

Figure 6.5 shows the controller's response. It is clear that the aircraft has an initial pitch angle when on the runway. At 28 seconds, $\overline{V}_r$ is reached and the aircraft rotates. The pitch rate graph shows that the pitch damper succeeds in keeping the pitch mode under control. The angle control deviates a bit from the reference. This is due to sensor noise degrading the angle measurement. Altitude increases quickly after the aircraft rotates.

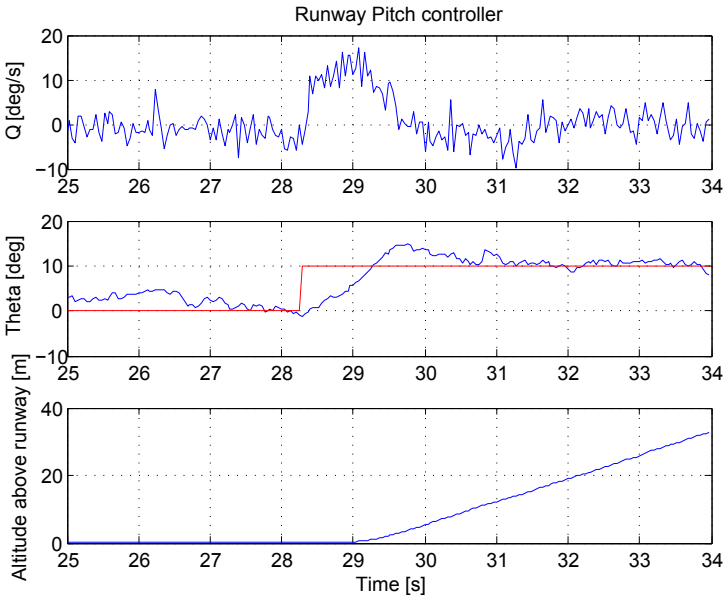

Figure 6.5: Simulated pitch control during Take-off

6.4 Runway Roll Regulation

The roll regulation response during Take-off is shown in Figure 6.6. Up until 81 seconds, the aircraft is still on the runway. Even though the noise degrades the angle measurement, it is clear that once the aircraft becomes airborne the angle is well regulated.

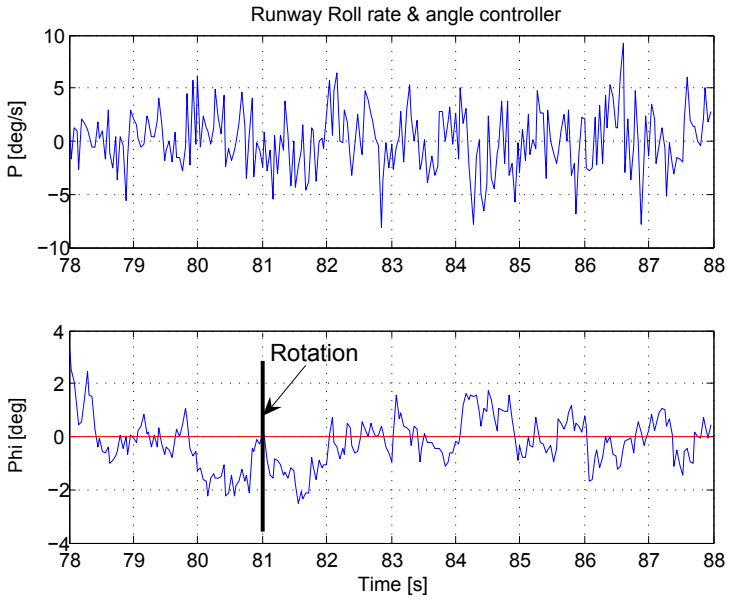

Figure 6.6: Simulated roll regulation during Take-off

6.5 Summary

The non-linear simulations confirms that all the Take-off controllers function as desired to perform Take-off. As mentioned in Section 2.2.1, Take-off specific Climb out controllers were not designed or implemented. However, the flight controllers designed in Chapter 9 and 10 are used for the Climb out phase.

This concludes the Take-off section of this thesis. The overall conclusions of the Take-off controllers together with recommendations, are stipulated in Chapter 13.

Part II

Waypoint- and Dynamic Pursuit Navigation

Chapter 7

Waypoint- and Dynamic Pursuit Navigation System Design

The goal of this section is to enable UAVs to fly between specified waypoints and be able to follow moving surface objects, which will be called Dynamic Pursuit Navigation. An upgrade of the current guidance controllers available in the ESL, need to be done to enable the Dynamic Pursuit Navigation algorithms to be applied. Some of the flight stability (innerloop) controllers will also require a redesign to function with the new guidance control.

Since a fixed wing aircraft is used for this research, it cannot hover. Aircraft are usually flown at a constant airspeed as the responsiveness to thrust commands are much slower than the aerodynamic surfaces. The dynamics and effectiveness of the aerodynamic surfaces is also a function of airspeed. In order to simplify the object following problem, the following assumptions are made:

- The aircraft maintains a constant airspeed.
- A stabilised camera is mounted on the aircraft that can change its line of sight to point in the direction of the object.
- Information about the object's motion (velocity and position) is available.
- The object being followed does not perform aggressive manoeuvres. Its velocity is assumed constant along straight lines for long periods of time.
- The aircraft travels faster than the object.

7.1 Strategy

7.1.1 Dynamic Pursuit Navigation

The idea behind Dynamic Pursuit Navigation, in this thesis, is to keep a constant distance between the aircraft and a moving surface object, with minimal information about the object and applying real-time trajectory planning. It is assumed that the aircraft flies faster than the object moves, and a circular path of constant radius and altitude is defined around the object. This will prevent constant change of the camera's view.

The information that is available about the object does not allow its dynamics to be observed. Controlling the motion between the aircraft and object by means of specialised innerloop controllers is thus not possible. Rather an online algorithm is derived that is dependant on the relative position and velocity of the object.

If it is assumed that the object and aircraft are point masses and the relative motion between them can be described kinematically. The motion of the aircraft relative to the object can then be controlled by applying an acceleration vector to the aircraft, which will ensure the aircraft remains at the desired radius without guidance control.

7.1.2 Stability control

In order for the Dynamic Pursuit Navigation algorithm to be applied to the aircraft, the stability (innerloop) control will have to enable it to be viewed as a steerable acceleration vector. This concept has been designed and evaluated by [14].

One of the practical disadvantages of this method is that the thrust responds too slowly and should it be used as part of the steerable acceleration vector, large variations from the desired path can be observed. As a result, thrust is used solely to regulate airspeed, even when large pitch changes are made.

The main component of the acceleration vector is the lift from the main wing. This acceleration can be rotated by rolling the aircraft. Using these two in combination will allow the implementation of the Dynamic Pursuit Navigation algorithm. The aircraft's side slip is also regulated to prevent instability and reduce drag.

7.1.3 Guidance control

The purpose of the guidance controllers is not to perform Dynamic Pursuit Navigation, but rather to act as a regulator that brings the aircraft back to the desired flight path, should it deviate. These deviations will be caused by wind disturbances and delays in the generation of the aircraft's acceleration vector. As no position based kinematic guidance controllers have been designed at the ESL, this architecture will be derived in this thesis.

7.1.4 Trajectories to be flown

Since this guidance controller architecture is new, it will also be used for Waypoint navigation. This will provide insight into its performance, should the need for comparison to other architectures arise.

The path (or trajectory) that is to be flown for object following can be simplified to a 2D problem since no altitude changes will be required. Navigation will also be simplified to a 2D problem.

All these controllers will be combined to create a complete flight control system to perform waypoint- and Dynamic Pursuit Navigation. Figure 7.1 shows a block diagram representation of how the flight controllers will be implemented.

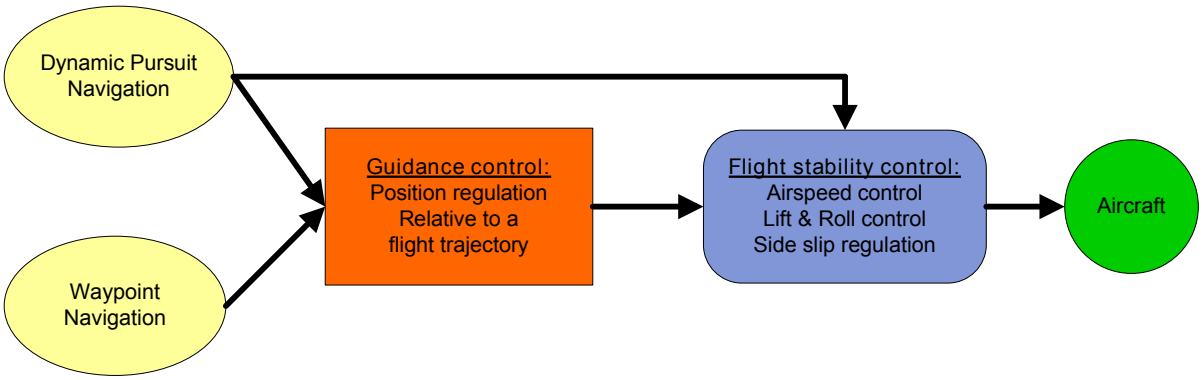

Figure 7.1: Block diagram representation of the Waypoint- and Dynamic Pursuit Navigation system

7.2 Layout

Before any controllers can be designed, a mathematical model must be derived for the aircraft in flight. Since extensive research has been done in modelling an aircraft in flight, this model is not re-derived.

Since the design strategies used for guidance is similar to the research done by [14], the model derived by [14] is used and summarised in chapter 8. By the same reasoning, some of the stability controllers designed by [14] are also used. Chapter 9 summarises these controllers and highlights redesigned elements to suit this research.

The design of position based kinematic guidance controllers is shown in chapter 10. These controllers are used to regulate the position of an aircraft about a specified trajectory. Trajectories used for Waypoint navigation and the Dynamic Pursuit Navigation algorithm are then defined in chapter 11.

All these controllers are then combined and tested in a full non-linear simulation. The results of this simulation is shown in chapter 12.

Chapter 8

Aircraft Dynamic Flight Model

The description of the axis systems, attitude descriptions and 6-DOF EOM that describe the position, motion and orientation of the aircraft has already been discussed in Chapter 3.

Before flight controllers can be designed, a model of the aircraft's interactions with the atmosphere has to be derived. This is not explicitly done in this thesis as it has been well documented in other research. The model derived by [14] is used.

8.1 Aerodynamic dynamic model [14]

The aerodynamic model derived by [14], first mathematically describes the motion of the body axis relative to the wind velocity vector (Wind axis), then proceeds to describe the motion of the wind axis relative to inertial space. The modes of motion are then decoupled to produce four decoupled systems describing the axial-, normal-, roll and lateral directional motion.

The normal motion is equivalent to the aerodynamic Short Period mode, and the lateral directional motion is equivalent to the Dutch Roll mode. These linear decoupled models are stated below for convenience, and used for the design of flight stability (innerloop) controllers in Chapter 9.

Axial dynamics:

$$\begin{aligned} \dot{T} &= \left[-\frac{1}{\tau_T}\right] T + \left[\frac{1}{\tau_T}\right] T_C \\ A_W &= \left[\frac{1}{m}\right] T + \left[-\frac{\bar{q}S}{m} C_D\right] \end{aligned} \tag{8.1.1}$$

Normal dynamics:

$$\begin{aligned} \begin{bmatrix} \dot{\alpha} \\ \dot{Q} \end{bmatrix} &= \begin{bmatrix} -\frac{\bar{q}S}{m\bar{V}_a} C_{L_\alpha} & 1 - \frac{\bar{q}S}{m\bar{V}_a}\frac{\bar{c}}{2\bar{V}_a} C_{L_Q} \\ \frac{\bar{q}S\bar{c}}{I_{yy}} C_{m_\alpha} & \frac{\bar{q}S\bar{c}}{I_{yy}}\frac{\bar{c}}{2\bar{V}_a} C_{m_Q} \end{bmatrix} \begin{bmatrix} \alpha \\ Q \end{bmatrix} + \begin{bmatrix} -\frac{\bar{q}S}{m\bar{V}} C_{L_{\delta_E}} \\ \frac{\bar{q}S\bar{c}}{I_{yy}} C_{m_{\delta_E}} \end{bmatrix} \delta_E + \begin{bmatrix} -\frac{\bar{q}S}{m\bar{V}_a} C_{L_0} + \frac{e_{33}^{WI}}{\bar{V}_a} g \\ \frac{\bar{q}S\bar{c}}{I_{yy}} \end{bmatrix} \\ \begin{bmatrix} C_W \\ Q \end{bmatrix} &= \begin{bmatrix} -\frac{\bar{q}S}{m} C_{L_\alpha} & -\frac{\bar{q}S}{m}\frac{\bar{c}}{2\bar{V}_a} C_{L_q} \\ 0 & 1 \end{bmatrix} \begin{bmatrix} \alpha \\ Q \end{bmatrix} + \begin{bmatrix} -\frac{\bar{q}S}{m} C_{L_{\delta_E}} \\ 0 \end{bmatrix} \delta_E + \begin{bmatrix} -\frac{\bar{q}S}{m} C_{L_0} \\ 0 \end{bmatrix} \end{aligned} \tag{8.1.2}$$

Roll dynamics:

$$\begin{aligned}\dot{P}_W &= \left[\frac{\bar{q}Sb^2C_{l_p}}{2\overline{V}_a I_{xx}}\right] P_W + \left[\frac{\bar{q}SbC_{l_{\delta_A}}}{I_{xx}}\right]\delta_A \\ P_W &= [1]\, P_W + [0]\,\delta_A\end{aligned} \tag{8.1.3}$$

Directional dynamics:

$$\begin{aligned}\begin{bmatrix}\dot{\beta}\\ \dot{R}\end{bmatrix} &= \begin{bmatrix}\frac{\bar{q}S}{m\overline{V}_a}C_{y_\beta} & -1+\frac{\bar{q}S}{m\overline{V}_a}\frac{b}{2\overline{V}_a}C_{y_r}\\ \frac{\bar{q}Sb}{I_{zz}}C_{n_\beta} & \frac{\bar{q}Sb}{I_{zz}}\frac{b}{2\overline{V}_a}\end{bmatrix}\begin{bmatrix}\beta\\ R\end{bmatrix} + \begin{bmatrix}\frac{\bar{q}S}{m\overline{V}_a}C_{y_{\delta_R}}\\ \frac{\bar{q}Sb}{I_{zz}}C_{n_{\delta_R}}\end{bmatrix}\delta_R + \begin{bmatrix}\frac{e_{33}^{WI}}{\overline{V}_a}g\\ 0\end{bmatrix}\\ \begin{bmatrix}B_W\\ R\end{bmatrix} &= \begin{bmatrix}\frac{\bar{q}S}{m}C_{y_\beta} & \frac{\bar{q}S}{m}\frac{b}{2\overline{V}_a}C_{y_r}\\ 0 & 1\end{bmatrix}\begin{bmatrix}\beta\\ R\end{bmatrix} + \begin{bmatrix}\frac{\bar{q}S}{m}C_{y_{\delta_R}}\\ 0\end{bmatrix}\delta_R\end{aligned} \tag{8.1.4}$$

Wind Axis Measurements

These dynamic models require measurements of the Wind axis. The sensors used are mounted to the aircraft, and measure the motion of the Body axis. Any variable related to the Wind axis is denoted with a W subscript. The conversions are shown in Equation 8.1.5.

$$\begin{aligned}\begin{bmatrix}A_W\\ B_W\\ C_W\end{bmatrix} &= \begin{bmatrix}\cos\alpha\cos\beta & \sin\beta & -\sin\alpha\cos\beta\\ -\cos\alpha\sin\beta & \cos\beta & \sin\alpha\sin\beta\\ \sin\alpha & 0 & \cos\alpha\end{bmatrix}\begin{bmatrix}a_X\\ a_Y\\ a_Z\end{bmatrix}\\ \begin{bmatrix}P_W\\ Q_W\\ R_W\end{bmatrix} &= \begin{bmatrix}\cos\alpha\cos\beta & \sin\beta & -\sin\alpha\cos\beta\\ -\cos\alpha\sin\beta & \cos\beta & \sin\alpha\sin\beta\\ \sin\alpha & 0 & \cos\alpha\end{bmatrix}\begin{bmatrix}P\\ Q\\ R\end{bmatrix}\end{aligned} \tag{8.1.5}$$

This conversion still requires α and β measurements. As these measurements are generally not available, simplifications will be made. Since α and β are small angles, small angle assumptions can be applied. Conventional aircraft are designed to have a small β angle while in flight and control is applied to ensure this. β is thus assumed to be zero. Equation 8.1.5 simplifies to,

$$\begin{aligned}\begin{bmatrix}A_W\\ B_W\\ C_W\end{bmatrix} &= \begin{bmatrix}1 & 0 & -\alpha\\ 0 & 1 & 0\\ \alpha & 0 & 1\end{bmatrix}\begin{bmatrix}a_X\\ a_Y\\ a_Z\end{bmatrix}\\ \begin{bmatrix}P_W\\ Q_W\\ R_W\end{bmatrix} &= \begin{bmatrix}1 & 0 & -\alpha\\ 0 & 1 & 0\\ \alpha & 0 & 1\end{bmatrix}\begin{bmatrix}P\\ Q\\ R\end{bmatrix}\end{aligned} \tag{8.1.6}$$

The Body axis coordinated axial acceleration (a_X) is typically much smaller than the normal acceleration (a_Z). The normal acceleration will have an effect on the Wind axis coordinated

axial acceleration. The Wind axis coordinated accelerations are approximated in Equation 8.1.7. Any rate scaled by α (a small angle) can be neglected. The Wind axis coordinated rates shown in Equation 8.1.8.

$$\begin{bmatrix} A_W \\ B_W \\ C_W \end{bmatrix} = \begin{bmatrix} 1 & 0 & -\frac{m}{\bar{q}SC_{L_\alpha}} \\ 0 & 1 & 0 \\ 0 & 0 & 1 \end{bmatrix} \begin{bmatrix} a_X \\ a_Y \\ a_Z \end{bmatrix} + \begin{bmatrix} \frac{-m}{\bar{q}S} \\ 0 \\ 0 \end{bmatrix} C_{L_0} \tag{8.1.7}$$

$$\begin{bmatrix} P_W \\ Q_W \\ R_W \end{bmatrix} = \begin{bmatrix} 1 & 0 & 0 \\ 0 & 1 & 0 \\ 0 & 0 & 1 \end{bmatrix} \begin{bmatrix} P \\ Q \\ R \end{bmatrix} \tag{8.1.8}$$

8.2 Summary

This concludes the summary of the aircraft's dynamic flight model derived in [14]. Other forces that act on the aircraft, such as gravity, have already been defined in Chapter 3. This model is used in the following chapter as the base for linear flight controller design.

Since this is a linear model, it cannot be used for full non-linear simulation. The model derived by [3] and shown in Equation 3.3.1 is used for the full non-linear simulation.

Chapter 9

Innerloop Flight Control

The innerloop flight controllers are aimed at controlling the fundamental motion of the aircraft while it is airborne. The architecture used to control the various flight modes of motion, is dependant on its interface to the outerloop controllers.

As will be discussed in detail in chapter 10, the outerloop requires a steerable acceleration vector. The lift from the main wing produces the largest force (or acceleration) by the airframe, and is the main component of the innerloop acceleration vector. The roll angle determines the direction in which the lift acts, thus it is used to steer the acceleration vector. In combination, lift and roll angle are used to produce the steerable acceleration vector.

Thrust will not be used as part of the steerable acceleration vector, due to its actuation lag. It is used solely to regulate airspeed. To ensure that the aircraft flies coordinated turns, the lateral body acceleration will be regulated to zero to ensure that the lift vector always acts in the xz_B-plane ($\therefore \beta = 0$).

A standard layout is followed for the design of each controller:

- The state space representation of the model is shown.
- The controller is designed.
- Pole placement is discussed.
- Linear simulation results of the controller are shown.

9.1 Airspeed Controller

The aircraft's airspeed needs to be controlled to keep it flying at its trim airspeed and prevent it from stalling. The desired controller criteria are thus as follows,

- Zero steady state errors (eliminating drag).
- Regulation within 10%.

The aircraft's thrust is used to control the airspeed and the linearised equation of motion derived in Equation 8.1.1 is shown below.

$$\begin{aligned} \dot{T} &= \left[-\frac{1}{\tau_T}\right] T + \left[\frac{1}{\tau_T}\right] T_c \\ A_W &= \left[\frac{1}{m}\right] T + \left[-\frac{\bar{q}S}{m} C_D\right] \sin\alpha \end{aligned} \tag{9.1.1}$$

Drag and gravity have the largest influence on the aircraft's airspeed. Since drag is not easily modelled and only changes with airspeed, it is rather dealt with as a disturbance. Gravity causes the aircraft to deviate from the desired airspeed when the aircraft's climb rate changes. Linear airspeed controllers can be designed by omitting the drag and gravity terms, which are then modelled as disturbances to the system [11, 13].

When applying this control to aggressive flight (large roll- and pitch angles), the non-linear gravity term causes a large axial acceleration disturbance. This can be countered by designing an axial acceleration controller with integral control, and closing a velocity loop around it. Practically this is not a good architecture, since the axial acceleration measurements are small and typically below the sensor's noise floor. The effect of this disturbance is pulsing of the throttle.

The error induced by gravity will then only be countered once it manifests as an airspeed error. Due to the lag in thrust response, these errors could potentially be large causing significant deviations from the commanded airspeed. An attitude independent airspeed controller design was investigated by applying feedback linearisation (also known as dynamic inversion) techniques [10, 14]. This would allow for large changes in pitch angle, without compromising the aircraft's airspeed regulation.

9.1.1 Feedback Linearisation

Feedback linearisation (FL) uses a feedforward term to the actuator (thrust), to counter the effects of a known disturbance on the state of interest (airspeed), by monitoring the rates of change of the variables that contribute towards it. This feedforward term is determined by differentiating the output of interest, until the actuator is present in the equation (allowing direct access for feedforward).

$$\begin{aligned} \dot{\overline{V}}_a &= A_W - g\sin(\theta_W) \\ &= \frac{T}{m} - g\sin(\theta_W) \end{aligned} \tag{9.1.2}$$

Differentiating the output equation of interest (airspeed, Equation 9.1.2) and assuming that angle of attack (α) is a small angle, the dynamic equation for $\overline{V}_a$ becomes,

$$\ddot{\overline{V}}_a = \frac{\dot{T}}{m} - g\cos(\theta_W)\,\dot{\theta}_W \tag{9.1.3}$$

Substituting the dynamics of the thrust (Equation 9.1.1) into Equation 9.1.3, the new dynamic equation becomes,

$$\ddot{\overline{V}}_a = -\frac{1}{\tau_T}\dot{\overline{V}}_a + \frac{1}{m\tau_T}T_c - g\cos(\theta_W)\,\dot{\theta}_W \tag{9.1.4}$$

Before the feedback linearisation is done, a control law is defined. Feedback is possible from A_W and $\overline{V}_a$. As mentioned previously, no direct feedback from the A_W measurement is implemented. Any steady state errors will be dealt with by implementing an integrator on airspeed. The control law and architecture are shown below in Figure 9.1 and Equation 9.1.5, where T' is the feedforward term used to apply the feedback linearisation.

$$\begin{aligned} T_c &= -k_v\overline{V}_a - k_e E_v + T' \\ \text{where}\quad E_v &= \overline{V}_a - \overline{V}_{a_{ref}} \end{aligned} \tag{9.1.5}$$

Substituting the control law into the dynamic equation (9.1.4) gives,

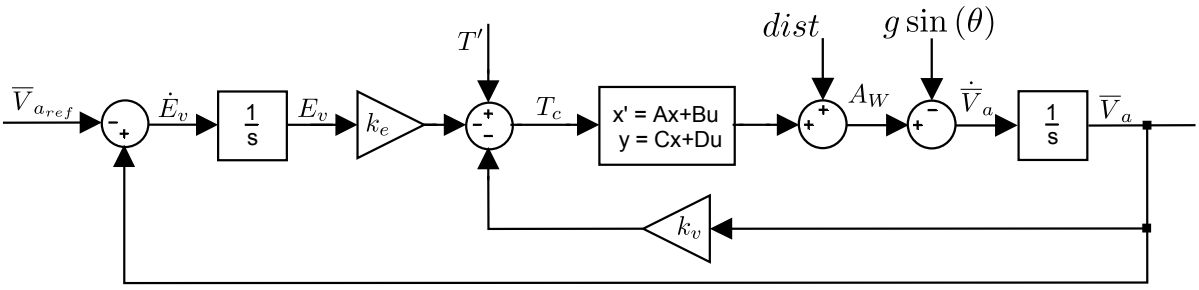

Figure 9.1: Airspeed Controller Architecture

$$\begin{aligned} \ddot{\overline{V}}_a &= -\frac{1}{\tau_T}\dot{\overline{V}}_a + \frac{1}{m\tau_T}\left(-k_v\overline{V} - k_e E_v + T'\right) - g\cos(\theta_W)\,\dot{\theta}_W \\ &= \left(\frac{-1}{\tau_T}\right)\dot{\overline{V}}_a + \left(\frac{-k_v}{m\tau_T}\right)\overline{V} + \left(\frac{-k_e}{m\tau_T}\right)E_v + \frac{1}{m\tau_T}T' - g\cos(\theta_W)\,\dot{\theta}_W \end{aligned}$$

T' is used to remove the gravity term,

$$\begin{aligned} 0 &= \frac{1}{m\tau_T}T' - g\cos(\theta_W)\,\dot{\theta}_W \\ \therefore T' &= gm\tau_T\cos(\theta_W)\,\dot{\theta}_W \\ \text{where}\quad \dot{\theta}_W &= \cos(\phi)\,Q - \sin(\phi)\,R \end{aligned} \tag{9.1.6}$$

Applying the feedback linearisation defined in Equation 9.1.6, the linearised dynamic equation that is to be used for controller design is,

$$\ddot{\overline{V}}_a = \left[\frac{-1}{\tau_T}\right]\dot{\overline{V}}_a + \left[\frac{-k_v}{m\tau_T}\right]\overline{V}_a + \left[\frac{-k_e}{m\tau_T}\right]E_v$$

This dynamic equation can be written in state space form as,

$$\begin{bmatrix} \ddot{\overline{V}}_a \\ \dot{\overline{V}}_a \\ \dot{E}_v \end{bmatrix} = \begin{bmatrix} \frac{-1}{\tau_T} & \frac{-k_v}{m\tau_T} & \frac{-k_e}{m\tau_T} \\ 1 & 0 & 0 \\ 0 & 1 & 0 \end{bmatrix} \begin{bmatrix} \dot{\overline{V}}_a \\ \overline{V}_a \\ E_v \end{bmatrix} + \begin{bmatrix} 0 \\ 0 \\ 1 \end{bmatrix} \overline{V}_{a_{ref}}$$
$$\overline{V}_a = \begin{bmatrix} 0 & 1 & 0 \end{bmatrix} \begin{bmatrix} \dot{\overline{V}}_a \\ \overline{V}_a \\ E_v \end{bmatrix} \tag{9.1.7}$$

9.1.2 Pole Placement and Controller Gains

The closed loop characteristic equation is calculated by determining the eigenvalues of the A-matrix.

$$\begin{aligned} s_{CL} &= |s\mathbf{I} - \mathbf{A}| \\ &= \begin{vmatrix} s - \left(\frac{-1}{\tau_T}\right) & -\left(\frac{-k_v}{m\tau_T}\right) & -\left(\frac{-k_e}{m\tau_T}\right) \\ -1 & s & 0 \\ 0 & -1 & s \end{vmatrix} \\ &= s^3 + \frac{(m)}{m\tau_T}s^2 + \frac{k_v}{m\tau_T}s + \frac{k_e}{m\tau_T} \\ &= s^3 + \alpha_2 s^2 + \alpha_1 s + \alpha_0 = 0 \end{aligned} \tag{9.1.8}$$

As there are only two controller gains in Equation 9.1.8, a choice has to be made about the what needs to be controlled since there will be three closed loop poles. It was decided that two complex poles will be placed (with frequency ω_V and damping ζ_V) with a third real pole at a higher frequency which is not specified. The desired characteristic equation is,

$$s_{CL} = \left(s^2 + 2\zeta_v\omega_v s + \omega_v^2\right)$$

Using long division, the controller gains can be calculated.

$$\begin{aligned} k_v &= m\tau_T\left[\left(1 - 4\zeta_V^2\right)\omega_V^2 + \frac{2\zeta_V\omega_V}{\tau_T}\right] \\ k_e &= m\tau_T\left(\frac{1}{\tau_T} - 2\zeta_V\omega_V\right)\omega_V^2 \end{aligned} \tag{9.1.9}$$

To ensure that the two complex poles are slower than the real pole, they are placed at half the open loop frequency. The damping is set to optimally damped.

$$\begin{aligned} \omega_V &= \frac{1}{2\tau_T} \\ \zeta_V &= 0.707 \end{aligned} \tag{9.1.10}$$

9.1.3 Reference and Disturbance steps

Figure 9.2 shows both the step- and disturbance response of the airspeed controller. The plots show that there is no steady state error and the disturbance rejection is within 10%, thus complying with the design requirements.

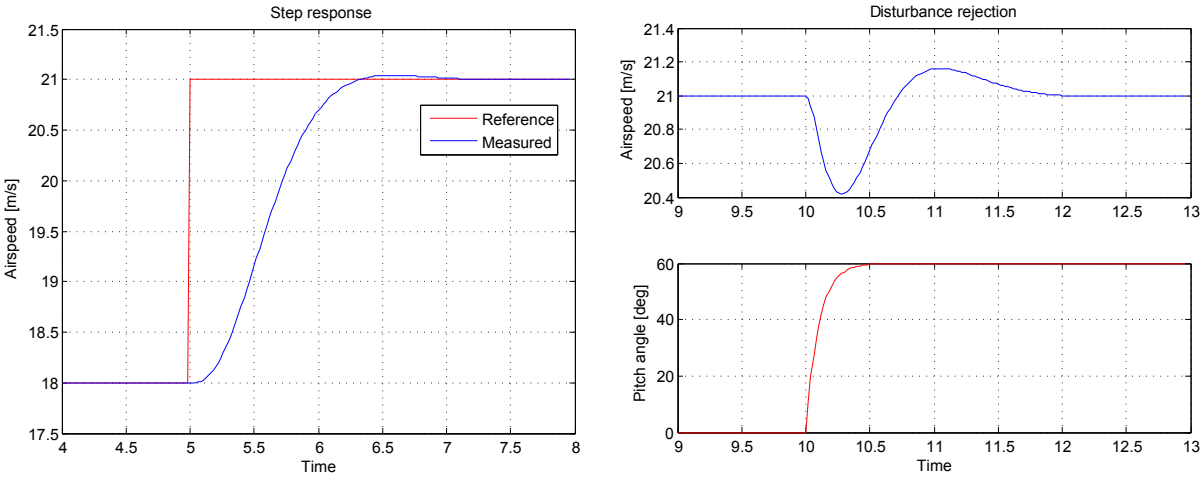

Figure 9.2: Linear airspeed step- and disturbance responses

9.2 Normal Specific Acceleration Controller [14]

Lift is the main aerodynamic force that is produced by the aircraft and generated by the main wing. The Normal Specific Acceleration (NSA) controller designed in [14], allows control over the amount of lift generated by controlling the aircraft's short period mode. This controller allows the design of simple, kinematic guidance controllers in Chapter 10 through its acceleration interface.

For the outerloop controllers to work well, the NSA controller has to meet the following requirements,

- Rise time under 1 second.
- Zero steady state error.

Feedback linearisation is implemented to linearise the model to gravity, which makes the controller orientation independent. This can only be done with conventional airframes where the lift due to pitch rate (C_{L_Q}) and elevator deflection ($C_{L_{\delta_E}}$) can be ignored. The open loop state space model from Equation 8.1.2 is written below, with C_{L_q}, $C_{L_{\delta_E}}$ and the static terms omitted.

$$\begin{aligned}
\begin{bmatrix}\dot{\alpha}\\ \dot{Q}\end{bmatrix} &= \begin{bmatrix}-\frac{\bar{q}S}{m\overline{V}_a}C_{L_\alpha} & 1\\ \frac{\bar{q}S\bar{c}}{I_{yy}}C_{m_\alpha} & \frac{\bar{q}S\bar{c}}{I_{yy}}\frac{\bar{c}}{2\overline{V}_a}C_{m_Q}\end{bmatrix}\begin{bmatrix}\alpha\\ Q\end{bmatrix} + \begin{bmatrix}0\\ \frac{\bar{q}S\bar{c}}{I_{yy}}C_{m_{\delta_E}}\end{bmatrix}\delta_E\\
&= \begin{bmatrix}a_{11} & 1\\ a_{21} & a_{22}\end{bmatrix}\begin{bmatrix}\alpha\\ Q\end{bmatrix} + \begin{bmatrix}0\\ b_2\end{bmatrix}\delta E\\
C_W &= \begin{bmatrix}-\frac{\bar{q}S}{m}C_{L_\alpha} & 0\end{bmatrix}\begin{bmatrix}\alpha\\ Q\end{bmatrix} + \begin{bmatrix}0\end{bmatrix}\delta_E\\
&= \begin{bmatrix}\overline{V}_a a_{11} & 0\end{bmatrix}\begin{bmatrix}\alpha\\ Q\end{bmatrix} + \begin{bmatrix}0\end{bmatrix}\delta_E
\end{aligned} \tag{9.2.1}$$

The control law and architecture are,

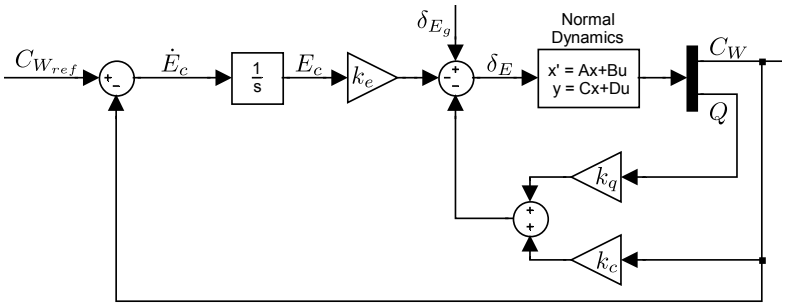

Figure 9.3: Normal Specific Acceleration controller architecture

$$\begin{aligned}
\delta_E &= -k_q Q - k_c C_W - k_e E_C + \delta_{E_G}\\
\text{with}\quad \dot{E}_C &= C_W - C_{W_{ref}}
\end{aligned} \tag{9.2.2}$$

With desired closed loop characteristic equation,

$$\alpha_c(s) = s^3 + \alpha_2 s^2 + \alpha_1 s + \alpha_0$$

The controller gains and gravity feedforward term (δ_{E_G}) are,

$$\begin{aligned}
k_q &= \tfrac{1}{b_2}\left(\alpha_2 + a_{11} + a_{22}\right) & k_c &= \tfrac{1}{\overline{V}_a a_{11} b_2}\left(\alpha_1 + a_{21} + a_{11}\alpha_2 + a_{11}^2\right)\\
k_e &= \tfrac{\alpha_0}{\overline{V}_a a_{11} b_2} & \delta_{E_G} &= \tfrac{1}{\overline{V}_a b_2}\left[\left(\alpha_2 + a_{11}\right) g_1 + \dot{g}_1\right]
\end{aligned} \tag{9.2.3}$$

where,

$$\begin{aligned}
a_{11} &= -\tfrac{\bar{q}S}{m\overline{V}_a}C_{L_\alpha} & a_{21} &= \tfrac{\bar{q}Sc}{I_{yy}}C_{m_\alpha} & a_{22} &= \tfrac{\bar{q}Sc}{I_{yy}}\tfrac{c}{2\overline{V}_a}C_{m_Q}\\
b_2 &= \tfrac{\bar{q}Sc}{I_{yy}}C_{m_{\delta_E}} & g_1 &= e_{33}^{WI} g & \dot{g}_1 &= -g\left[\left(\tfrac{C_W + e_{33}^{WI} g}{\overline{V}_a}\right) e_{13}^{WI} + P_W e_{23}^{WI}\right]
\end{aligned}$$

The feedback linearised closed loop state space model is,

$$\begin{bmatrix} \ddot{C}_W \\ \dot{C}_W \\ \dot{E}_C \end{bmatrix} = \begin{bmatrix} \begin{pmatrix} a_{11}+a_{22} \\ -b_2 k_q \end{pmatrix} & \begin{pmatrix} a_{21}-a_{11}a_{22} \\ -\overline{V}_a a_{11} b_2 k_c + a_{11} b_2 k_q \end{pmatrix} & \begin{pmatrix} -\overline{V}_a a_{11} b_2 k_e \end{pmatrix} \\ 1 & 0 & 0 \\ 0 & 1 & 0 \end{bmatrix} \begin{bmatrix} \dot{C}_W \\ C_W \\ E_C \end{bmatrix} + \begin{bmatrix} 0 \\ 0 \\ -1 \end{bmatrix} C_{W_R} \tag{9.2.4}$$

Pole placement

The above architecture allows control over all three closed loop poles. Since this NSA controller is not aimed at changing the short period mode behaviour of the aircraft (which is represented by two complex poles), the frequency of the open loop poles are not changed. Their damping is altered to ensure reduced overshoot. The integrator's frequency is then set to be the dominant closed loop frequency. It is not set above 6 rad/s to avoid inducing unmodelled modes that the airframe has due to flex.

This results in the desired closed loop characteristic equation shown in Equation 9.2.5 (where the complex poles have a frequency = ω_c and damping = ζ_c, with the integrator frequency = ω_I).

$$\begin{aligned} s_{CL} &= (s+\omega_I)\left(s^2 + 2\zeta_c\omega_c s + \omega_c^2\right) \\ &= s^3 + (2\zeta_c\omega_c + \omega_I)\, s^2 + \left(2\zeta_c\omega_c\omega_I + \omega_c^2\right) s + \omega_c^2 \end{aligned} \tag{9.2.5}$$

where,

$$\begin{aligned} \omega_n = \omega_c &= \begin{vmatrix} a_{11} & 1 \\ a_{21} & a_{22} \end{vmatrix} \qquad \omega_I = 6 \ \ rad/s \\ \zeta_c &= 0.707 \end{aligned}$$

Step response

The linear step response in Figure 9.4, shows that the NSA controller meets its requirements.

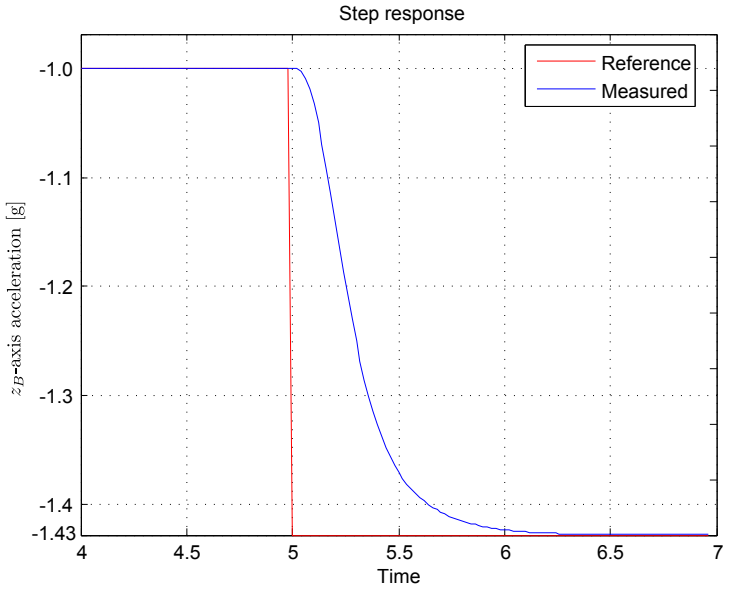

Figure 9.4: Linear Normal Specific Acceleration step response

9.3 Roll Angle Controller

An aircraft's direction of travel is changed by directing the main wing lift vector. This direction is controlled by rolling the aircraft to a certain angle, which changes the lateral inertial acceleration component.

The requirements for the controller are,

- Rise time within 1 second.
- Zero steady state error.

The aircraft's roll control is designed by incorporating both the rate and angle. As the specific angle that the aircraft is rolled controls the amount of lateral acceleration, an integrator is implemented on roll angle to eliminate any steady state errors. A feedforward term ($\overline{N}$) is used to eliminate the effect of the integrator from the input. By adding this term, the integrator dynamics can be ignored by the outerloop controllers. Using the linear open loop plant from Equation 8.1.3, the control law and is defined below and architecture is shown in Figure 9.5.

$$\begin{aligned} & & \delta_A &= -k_p P_W - k_\phi \phi - k_e E_\phi + \overline{N}\phi_{ref} \\ \text{where,} & & \dot{E}_\phi &= \phi - \phi_{ref} \end{aligned} \tag{9.3.1}$$

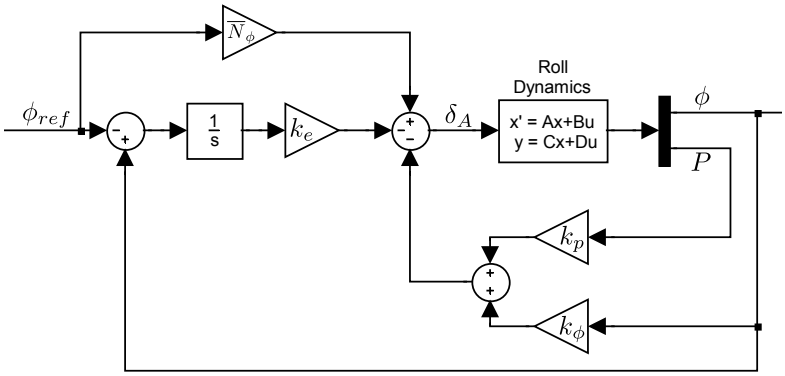

Figure 9.5: Roll Angle Controller Architecture

Implementing the control law, the closed loop state space representation is,

$$\begin{bmatrix} \dot{P}_W \\ \dot{\phi} \\ \dot{E}_\phi \end{bmatrix} = \begin{bmatrix} (a_{11} - b_{11}k_p) & -b_{11}k_\phi & -b_{11}k_e \\ 1 & 0 & 0 \\ 0 & 1 & 0 \end{bmatrix} \begin{bmatrix} P_W \\ \phi \\ E_\phi \end{bmatrix} + \begin{bmatrix} \overline{N} \\ 0 \\ -1 \end{bmatrix} \phi_{ref} \tag{9.3.2}$$

with,

$$a_{11} = \frac{\overline{q}Sb^2C_{l_p}}{2\overline{V}_a I_{xx}} \quad \text{and} \quad b_{11} = \frac{\overline{q}SbC_{l_{\delta_A}}}{I_{xx}}$$

The closed loop characteristic equation is determined,

$$\begin{aligned} s_{CL} &= \begin{vmatrix} s - (a_{11} - b_{11}k_p) & -(-b_{11}k_\phi) & -(-b_{11}k_e) \\ -1 & s & 0 \\ 0 & -1 & s \end{vmatrix} \\ &= s^3 + (b_{11}k_p - a_{11})\, s^2 + b_{11}k_\phi s + b_{11}k_e \\ &= s^3 + \alpha_2 s^2 + \alpha_1 s + \alpha_0 = 0 \end{aligned} \tag{9.3.3}$$

The controller gains are calculated from Equation 9.3.3 as,

$$\begin{aligned} k_p &= \tfrac{\alpha_2 + a_{11}}{b_{11}} & k_\phi &= \tfrac{\alpha_1}{b_{11}} \\ k_e &= \tfrac{\alpha_0}{b_{11}} & \overline{N} &= \tfrac{k_e}{\omega_{\overline{N}}} \end{aligned} \tag{9.3.4}$$

Pole placement

As with the NSA controller, there are three closed loop poles that can be placed. When a controller is designed by using this method, it is critical to ensure that the controller gains make sense. In this case, all gains should be negative to produce correct roll rate and -angle disturbance rejection. If two complex poles are placed faster than the real pole, the roll angle disturbance rejection would be under damped. If the complex poles are placed slower than the real pole, the $\overline{N}$ term would not cancel out the effect of the integrator.

Three real poles (ω_R, ω_ϕ and ω_I) are thus placed to ensure good disturbance rejection. ω_R is placed faster than the open loop pole (a_{11}), while ω_ϕ is placed slower to ensure that both

controller gains (k_P and k_ϕ) are negative. The integrator pole ω_I is placed much slower than ω_ϕ. The effect of this pole will however be eliminated by the $\overline{N}$ term.

The closed loop characteristic equation and specific closed loop pole locations are shown in Equation 9.3.5.

$$\begin{aligned} s_{CL} &= (s+\omega_R)(s+\omega_\phi)(s+\omega_I) \\ &= s^3 + (\omega_R+\omega_\phi+\omega_I)s^2 + [\omega_\phi\omega_I + \omega_R(\omega_\phi+\omega_I)]s + (\omega_R\omega_\phi\omega_I) \end{aligned}$$

$$\omega_R = 1.5|a_{11}| \qquad \omega_\phi = \frac{1}{2}|a_{11}| = \frac{1}{3}\omega_R \qquad \omega_I = \frac{1}{4}\omega_\phi \tag{9.3.5}$$

Disturbance and Step response

A 10°/s roll rate disturbance is introduced into the system in Figure 9.6. The disturbance is rejected very quickly allowing for minimal angle deviation.

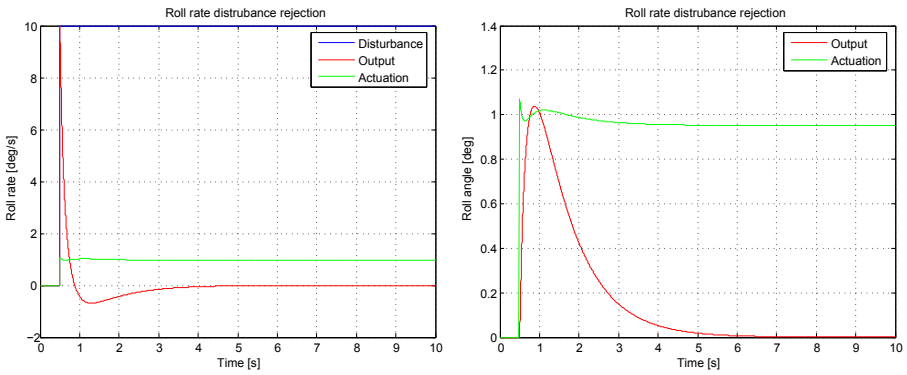

Figure 9.6: Linear 10°/s roll rate disturbance rejection

The effect of the $\overline{N}$ is clear, as the step response has the characteristics of the faster complex pole pair. The integrator's effect is seen as there is no steady state error. The design requirements are thus met.

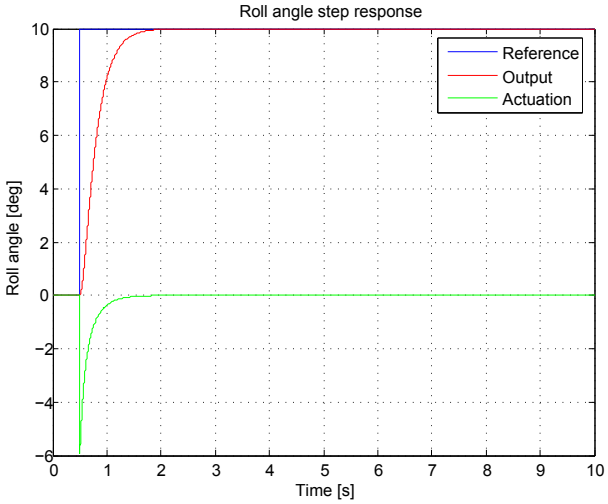

Figure 9.7: Linear roll angle controller step response

9.4 Lateral Specific Acceleration Controller [14]

During flight, it is required that the Dutch Roll mode of the aircraft be dampened and the side slip angle β be regulated to zero to ensure the aircraft flies in a coordinated manner. The Lateral Specific Acceleration (LSA) controller designed in [14] is used to both dampen the high frequency Dutch Roll mode and ensure $\beta = 0$. The control law and architecture are shown below.

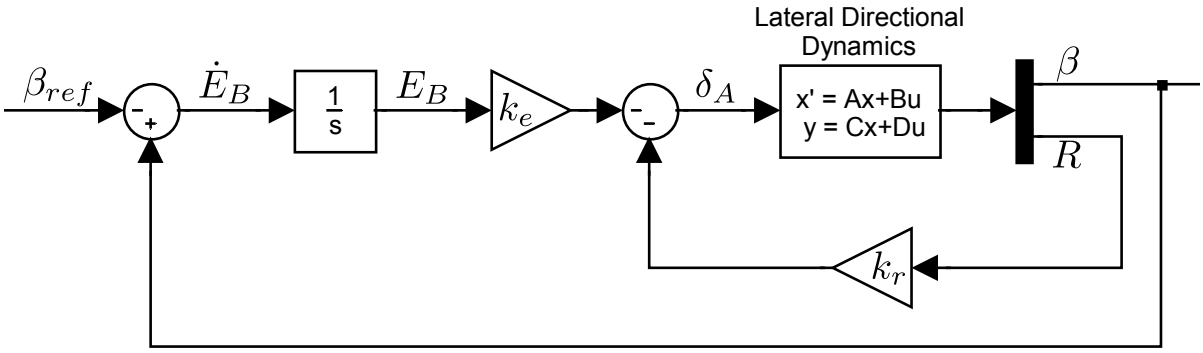

Figure 9.8: Lateral Specific Acceleration Controller Architecture

$$\begin{aligned} \delta_R &= -k_r R - k_e E_B \\ \dot{E}_B &= B_W - B_{W_{ref}} \end{aligned} \tag{9.4.1}$$

The yaw rate damping (ζ_R) and integrator frequency (ω_B) will be set. The controller gains are,

$$
\begin{aligned}
k_r &= \frac{I_{zz}}{N_{\delta_R}}\left(\frac{Y_\beta}{m\overline{V}_a} + \frac{N_R}{I_{zz}} + 2\zeta_R\omega_n\right) \\
k_e &= \frac{\omega_B}{K_{ss}}
\end{aligned}
\qquad \text{where} \qquad
\begin{aligned}
\omega_n &= \sqrt{\frac{Y_\beta \overline{N}_R}{m\overline{V}_a I_{zz}} + \frac{\overline{N}_\beta}{I_{zz}}} \\
K_{ss} &= \frac{Y_{\delta_R} Y_\beta}{m I_{zz}\omega_n^2}\left(\frac{\overline{N}_\beta}{Y_\beta} - \frac{\overline{N}_{\delta_R}}{Y_{\delta_R}}\right) \\
Y_\beta &= \overline{q}SC_{y_\beta} \\
Y_{\delta_R} &= \overline{q}SC_{y_{\delta_R}} \\
\overline{N}_\beta &= \overline{q}SbC_{n_\beta} \\
\overline{N}_R &= \frac{\overline{q}Sb^2C_{n_R}}{2\overline{V}_a} \\
\overline{N}_{\delta_R} &= \overline{q}SbC_{n_{\delta_R}}
\end{aligned}
\tag{9.4.2}
$$

The integrator gain has been calculated by applying TSS, thus

$$\omega_B < \frac{\omega_n}{6}$$

9.5 Summary

The innerloop flight controllers allow control over the aircraft's generated acceleration vector. Due to the robust nature of feedback control, any uncertainties in the aircraft model will not cause these controllers to become unstable or deviate much from the desired response. These controllers will be used as the core of the kinematic guidance controllers designed in the next chapter.

Chapter 10

Outerloop Controllers

Before the aircraft can fly a specific path (like navigate between various waypoints[1] and tracking objects), it has to be able to regulate its position relative to a path. The outerloop controllers make use of the innerloop controllers designed in Chapter 9 and is described in this chapter.

10.1 Guidance method

Guidance (outerloop) controllers designed in [13] use a small bank angle approximation which allows the controller to operate without the use of a kinematic state estimator. Small bank angles relate to a large turning circle, which is undesirable. The kinematic state estimator developed by [25] was used to avoid this limitation. The guidance architecture developed by [14] (called Specific Acceleration Matching) is not limited by small bank angles and was used as the basis for the guidance architecture used in this research.

10.1.1 Specific Acceleration Matching [14]

The Specific Acceleration Matching (SAM) controller was designed to allow an aircraft to fly any kinematically feasible trajectory. It starts off assuming the aircraft can be modelled as a kinematic point in space, that has a three dimensional (3D) steerable acceleration vector that can be commanded instantaneously (using TSS assumptions). A kinematically feasible trajectory is then defined and the aircraft's 3D acceleration vector is matched to this trajectory's acceleration vector.

This architecture defines the inertial position of the aircraft at every time step making the trajectory time dependent. Ideally the trajectory is defined such that the aircraft will travel at its trim airspeed. Should the aircraft's actual airspeed vary from the desired, the aircraft will have to alter its speed to "chase" the desired position along the trajectory. This is not a good practical guidance method. Rather, it is desired to regulate the airspeed independently of a predefined time variable.

The 3D steerable acceleration vector can be achieved by the aircraft's thrust (axial body acceleration), and rolling the lift vector of the main wing (acceleration in the yz_W-plane). Due

[1] A point in inertial space that needs to be flown through

to the thrust lag, the axial acceleration cannot be commanded instantaneously, which makes the practical implementation difficult.

Both the above mentioned problems can be overcome by simplifying the SAM controller so that no acceleration along the trajectory is required, thus using the aircraft's axial acceleration solely for airspeed regulation. This simplifies the 3D acceleration vector to a 2D commandable acceleration vector which is always perpendicular to the trajectory. This plane that remains perpendicular to the trajectory and passes through the aircraft's current position, will be called the Trajectory plane. The control then reduces to regulating the aircraft's position on the Trajectory plane and the aircraft's airspeed. The Trajectory plane will move along the trajectory as the aircraft travels along it. This makes the architecture position dependent and will be called Position-based Kinematic Guidance (PKG).

Before PKG can be designed, the Trajectory axis must be defined.

10.1.2 Trajectory Axis

A new orthogonal right handed axis system is defined that is used to describe the Trajectory plane, and called the Trajectory axis. The x_T-axis is defined along the trajectory, in the forward flight direction. The y_T-axis is perpendicular to the x_T-axis and points out to the right of the trajectory (when looking along the x_T-axis). The y_T-axis is always parallel to any vector that lies in the xy_E-axis. The z_T-axis completes the axis system and is perpendicular to the x_T-axis (and the trajectory). The y_T- and z_T-axes span the Trajectory plane. The origin of the Trajectory axis is the point on the trajectory that places the aircraft in the Trajectory plane.

The Euler angles that describe the orientation of the Trajectory axis are pitch (θ_T) and yaw (ψ_T), it has no roll angle. The Trajectory axis accelerations are A_T, B_T and C_T. A pictorial representation is shown in Figure 10.1.

10.1.3 Position-based Kinematic Guidance

PKG may be a better practical implementation, but it will still requires complicated computations to determine the Trajectory plane's position along an arbitrary trajectory. If the trajectories that are to be flown are geometric, the PKG will be greatly simplified. This research is not aimed at aerobatic flight, but rather tracking moving ground objects. The only trajectories required to fulfil this type of flight are straight lines and circles (or arcs), in the xy_E-plane. The aircraft's altitude changes need not to be gradual, thus discrete altitudes will be commanded.

Due to the above simplifications of the required flight trajectories, the Trajectory plane does not have to pitch to accommodate sloping altitude changes (thus $\theta_T = 0$). This causes the z_T-axis to be equal to the z_E-axis. Since the y_T- and z_T-axis are independent, the PKG controller can be split into control along these axes. Using TSS assumptions, the plant for the y_T-axis controller is a unity gain B_T acceleration. The plant for the z_T-axis controller is a unity gain C_T acceleration.

The combination of B_T and C_T accelerations will create the 2D acceleration vector required to regulate the aircraft's position on the Trajectory plane. These accelerations will be converted to innerloop commands in Section 10.2.3.

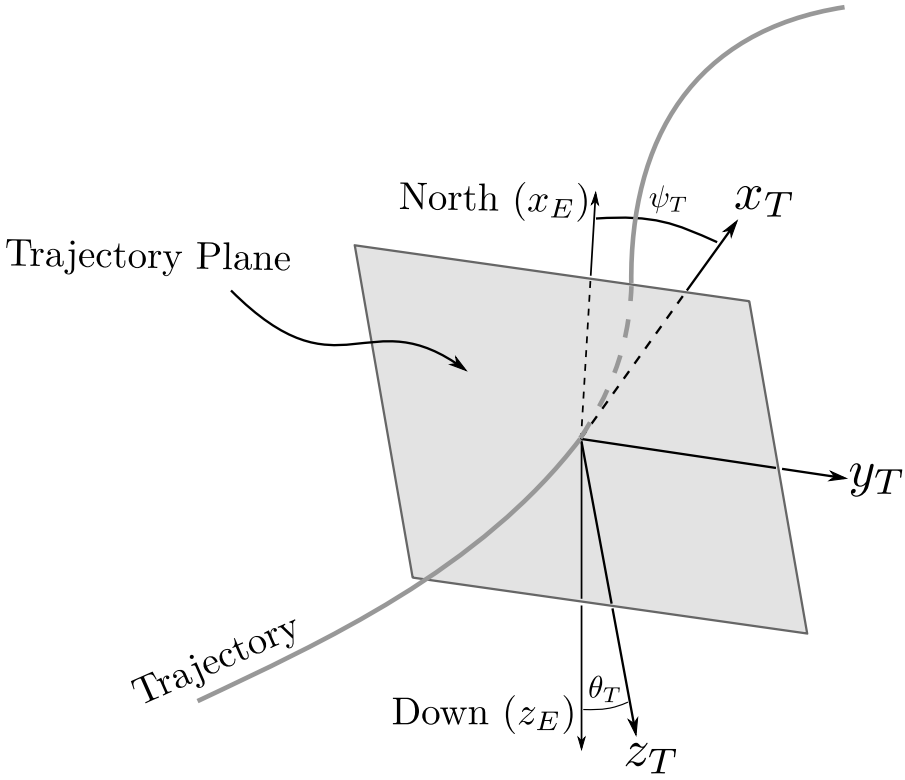

Figure 10.1: The Trajectory plane and -axis

10.2 Flight Trajectory Position Controllers

Using the PKG architecture described in Section 10.1.3, two sets of identical controllers are designed to regulate the aircraft's altitude and Cross Track Error while in flight. The most significant disturbance that will be present is wind. Since wind is the movement of the air that the aircraft flies in, a constant wind will cause an inertial velocity error, while gusts will cause a force disturbance on the aircraft. Constant winds will be compensated for by including integral control on the Trajectory axis velocity controllers. Gusts will be rejected by the innerloop controllers.

10.2.1 Altitude Controller

Controller Design

The control law is defined as,

$$\begin{aligned} C_{T_{ref}} &= -k_1 \dot{z}_T + k_2 E_{z_T} + C_{T_{FF}} \\ \dot{E}_{z_T} &= k_3 \left(z_{T_{ref}} - z_T \right) \end{aligned} \tag{10.2.1}$$

$C_{T_{FF}}$ is the Trajectory axis acceleration feedforward term, which is used to counter the effect of gravity ($\because C_{T_{FF}} = -\mathrm{g} = -9.81$). The control architecture is shown in Figure 10.2 and the closed loop state space form of the system in Equation 10.2.2

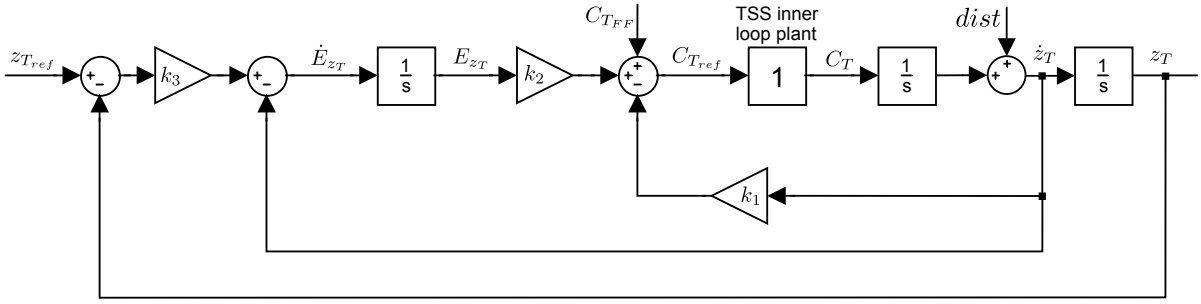

Figure 10.2: Altitude Control Architecture

$$\begin{bmatrix} \ddot{z}_T \\ \dot{E}_{z_T} \\ \dot{z}_T \end{bmatrix} = \begin{bmatrix} -k_1 & k_2 & 0 \\ -1 & 0 & -k_3 \\ 1 & 0 & 0 \end{bmatrix} \begin{bmatrix} \dot{z}_T \\ E_{z_T} \\ z_T \end{bmatrix} + \begin{bmatrix} 0 \\ k_3 \\ 0 \end{bmatrix} z_{T_{ref}}$$
$$z_T = \begin{bmatrix} 0 & 0 & 1 \end{bmatrix} \tag{10.2.2}$$

The closed loop characteristic equation is calculated as,

$$\begin{aligned} s_{CL} &= \begin{vmatrix} s-k_1 & -k_2 & 0 \\ 1 & s & k_3 \\ -1 & 0 & s \end{vmatrix} \\ &= s^3 + k_1 s^2 + k_2 s + k_2 k_3 \\ &= s^3 + \alpha_2 s^2 + \alpha_1 s + \alpha_0 = 0 \end{aligned} \tag{10.2.3}$$

The controller gains are thus,

$$\begin{aligned} k_1 &= \alpha_2 \\ k_2 &= \alpha_1 \\ k_3 &= \frac{\alpha_0}{\alpha_1} \end{aligned} \tag{10.2.4}$$

Pole Placement

The control architecture shown in Figure 10.2 allows the freedom to place three poles. A complex pole pair (frequency = ω_c, damping = ζ_c) and a real pole (frequency = ω_r) are placed. The characteristic equation of the desired closed loop poles is,

$$\begin{aligned} s_{CL} &= \left(s^2 + 2\zeta_c\omega_c s + \omega_c^2\right)(s + \omega_r) \\ &= s^3 + \left(2\zeta_c\omega_c + \omega_r\right)s^2 + \left(\omega_c^2 + 2\zeta_c\omega_c\omega_r\right)s + \omega_c^2\omega_r \end{aligned} \tag{10.2.5}$$

In order not to violate TSS, the closed loop poles must be placed at least five times slower than the innerloop poles. Practically, the closed loop poles were all placed at the same frequency and shown in Equation 10.2.6.

$$\begin{aligned} \omega_c &= \omega_r = 0.5 \quad \left[\frac{rad}{s}\right] \\ \zeta_c &= 0.8 \end{aligned} \tag{10.2.6}$$

Simulated response

Figure 10.3 shows a linear step response of the Trajectory axis altitude controller. The innerloop dynamics are not taken into account. It is clear that the controller performs well, with no steady state errors.

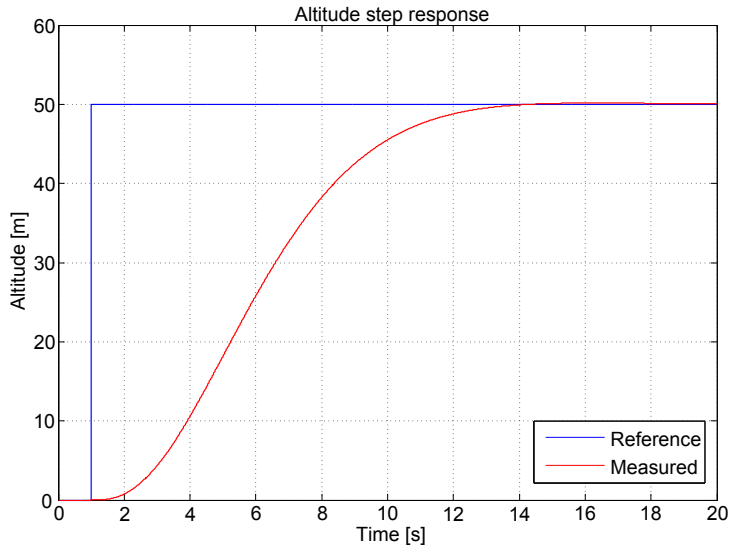

Figure 10.3: Trajectory axis altitude linear step response

10.2.2 Cross Track Error Controller

The Cross Track Error controller architecture is identical to the Altitude controller, as both plants are assumed to be identical. The only difference is the pole placement.

Controller Design

The control law is defined as,

$$\begin{aligned} B_{T_{ref}} &= -k_1 \dot{y}_T + k_2 E_{y_T} + B_{T_{FF}} \\ \dot{E}_{y_T} &= k_3 \left(y_{T_{ref}} - y_T \right) \end{aligned} \tag{10.2.7}$$

$B_{T_{FF}}$ is the Trajectory axis acceleration feedforward term and will be discussed in Chapter 11. When circles or arcs are flown, the steady state centripetal acceleration is fed forward. This

improves the tracking of the aircraft by eliminating the need for the velocity integrator (E_{y_T}) to first build up to this value.

The control architecture is shown in Figure 10.4.

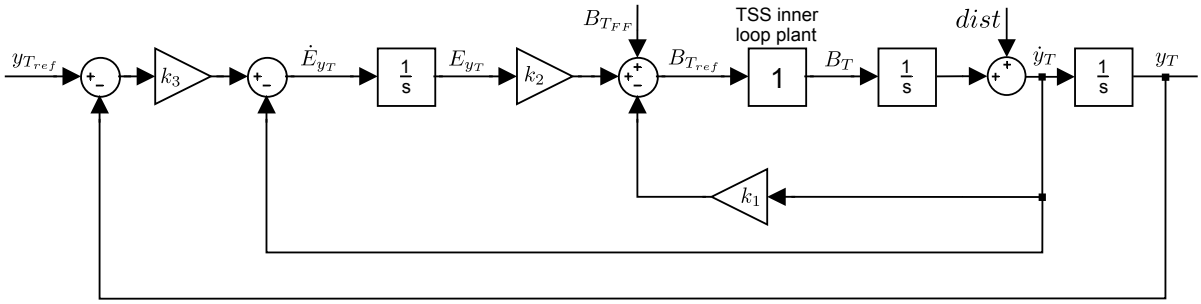

Figure 10.4: Cross Track Error Control Architecture

The closed loop state space form, characteristic equation and controller gains are the same as for the altitude controller. See equations 10.2.2, 10.2.3 and 10.2.4.

Pole Placement

The desired closed loop characteristic equation is identical to the altitude controller (Equation 10.2.5). The desired closed loop poles were all placed at the same frequency and the closed loop pole locations are,

$$\begin{aligned} \omega_c &= \omega_r = 0.4 \quad \left[\frac{rad}{s}\right] \\ \zeta_c &= 0.8 \end{aligned} \tag{10.2.8}$$

Simulated response

A linear step response of this controller is shown in Figure 10.5, with the zero steady state criteria is observed.

10.2.3 Mapping Body Accelerations onto the Trajectory Plane (during flight)

The Trajectory axis accelerations (B_T and C_T) that will be commanded by the position controllers in Section 10.2 now have to be mapped to the innerloop references. For this it is assumed that the aircraft flies at a constant airspeed (no axial accelerations) and the aircraft's side slip angle is regulated to zero ($B_W = 0$). The aircraft's NSA- and roll angle controllers will be used to generate the required 2D Trajectory plane acceleration vector.

This system can be modelled as a MIMO system, but an intuitive method is used to decouple the system into two SISO systems. The NSA controller is used to control the component of acceleration along the z_T-axis (C_T), independent of orientation. There are however

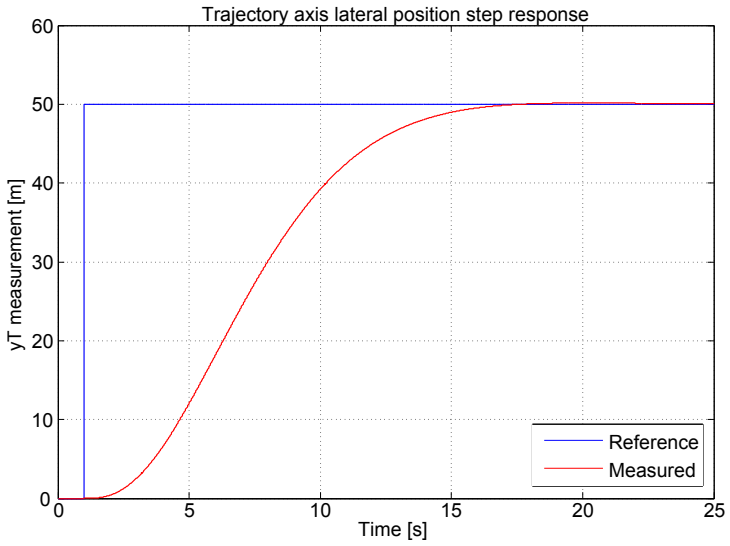

Figure 10.5: Trajectory axis lateral position linear step response

singularities at 90° pitch and roll, when the desired C_T acceleration cannot be achieved. But, as aerobatic flight will not be performed, these singularities will not be reached.

When the aircraft's roll angle changes, the component of NSA along the y_T-axis (B_T) changes while C_T is kept constant (with the controller). The B_T acceleration can thus be controlled by controlling the aircraft's roll angle.

The required Trajectory accelerations are coordinated into the Wind axis, but this might cause axial Wind acceleration to be required to fulfil the Trajectory accelerations. Instead, this method is used inversely by coordinating the Wind NSA in Trajectory axis, as axial Trajectory accelerations do not affect the PKG controller.

Coordinating Wind accelerations in Trajectory axis

An "intermediate" Wind axis (denoted with the subscript W') is used where the Wind axis has no roll angle ($\phi_W = 0$). This allows the NSA and roll angle to control the 2D acceleration vector in this "intermediate" Wind axis. The Euler angles for the DCM used for this coordination are yaw ($\psi_{W'T} = \psi_W - \psi_T$) and pitch ($\theta_{W'T} = \theta_W - \theta_T = \theta_W$).

$$\begin{bmatrix} A_T \\ B_T \\ C_T \end{bmatrix} = \left[DCM^{TW'}\right] \begin{bmatrix} 0 \\ B_{W'} \\ C_{W'} \end{bmatrix}$$
$$= \begin{bmatrix} \cos\psi_{W'T}\cos\theta_{W'T} & -\sin\psi_{W'T} & \cos\psi_{W'T}\sin\theta_{W'T} \\ \sin\psi_{W'T}\cos\theta_{W'T} & \cos\psi_{W'T} & \sin\psi_{W'T}\sin\theta_{W'T} \\ -\sin\theta_{W'T} & 0 & \cos\theta_{W'T} \end{bmatrix} \begin{bmatrix} 0 \\ B_{W'} \\ C_{W'} \end{bmatrix} \tag{10.2.9}$$

Rewriting Equation 10.2.9 to make the "intermediate" Wind accelerations the subject of the equation yields,

$$\begin{aligned} C_{W'} &= \frac{C_W}{\cos\theta_{W'T}} \\ B_{W'} &= \frac{B_W - \sin\psi_{W'T}\sin\theta_{W'T}\frac{C_W}{\cos\theta_{W'T}}}{\cos\psi_{W'T}} \\ &= \frac{B_W - \sin\psi_{W'T}\tan\theta_{W'T}C_W}{\cos\psi_{W'T}} \end{aligned} \tag{10.2.10}$$

The Wind accelerations required to realise the Intermediate-Wind accelerations can be generated by the NSA and roll angle controller. To keep the altitude dynamics separate from the Cross Track Error dynamics, the NSA is commanded taking the current roll angle (ϕ_W) into consideration.

$$\begin{aligned} C_{W'} &= C_{W_{ref}}\cos\phi_W \\ C_{W_{ref}} &= \frac{C_{W'}}{\cos\phi_W} \end{aligned} \tag{10.2.11}$$

Using the dot product of the two "intermediate" Wind accelerations to determine the roll angle required to produce a certain lateral acceleration ($B_{W'}$), is shown in Equation 10.2.12 (where $\mathbf{a}_{W'} = B_{W'}\mathbf{j}^{W'} + C_{W'}\mathbf{k}^{W'}$).

$$\begin{aligned} \mathbf{a}_{W'}\cdot(-C_{W'}) &= |\mathbf{a}_{W'}||-C_{W'}|\cos\phi_{W_{ref}} \\ \left(B_{W'}\mathbf{j}^{W'} + C_{W'}\mathbf{k}^{W'}\right)\cdot\left(-C_{W'}\mathbf{k}^{W'}\right) &= |\mathbf{a}_{W'}|\,(C_{W'})\cos\phi_{W_{ref}} \\ \therefore \phi_{W_{ref}} &= \arccos\left(\frac{-C'_W}{|\mathbf{a}_{W'}|}\right) \end{aligned} \tag{10.2.12}$$

The sign is lost when the dot product is calculated, and using the lateral acceleration (B'_W) the reference roll angle is commanded as,

$$\phi_{W_{ref}} = \arccos\left(\frac{-C_{W'}}{|\mathbf{a}_{W'}|}\right)\mathrm{sgn}\,(B_{W'}) \tag{10.2.13}$$

The controllers require measurements in Trajectory axis. These measurement conversions will be discussed next.

10.3 Trajectory Axis Measurements

The only measurements required for the PKG controller are velocity and position. These measurements are made by a GPS which gives orientation independent Earth axis readings. The velocity measurements are only dependant on the Trajectory axis orientation. Coordinating these measurements into the Trajectory axis,

$$\begin{bmatrix} \dot{x}_T \\ \dot{y}_T \\ \dot{z}_T \end{bmatrix} = \begin{bmatrix} \cos\psi_T & \sin\psi_T & 0 \\ -\sin\psi_T & \cos\psi_T & 0 \\ 0 & 0 & 1 \end{bmatrix} \begin{bmatrix} \dot{N} \\ \dot{E} \\ \dot{D} \end{bmatrix} \tag{10.3.1}$$

The position measurements are trajectory specific, where displacement along the y_T-axis is the cross track position and z_T-axis is the down displacement (or negative altitude).

10.4 Summary

This concludes the flight guidance controller designs. These controllers allow the aircraft to be flown along a specified 2D flight trajectory. The definition of these trajectories will be discussed in the following chapter, to achieve Waypoint- and Dynamic Pursuit Navigation.

Chapter 11

Waypoint- and Dynamic Pursuit Navigation

The guidance level controllers designed up to now allow the aircraft to be controlled relative to a trajectory. This chapter discusses the definition of trajectories which will enable Waypoint navigation and following of moving ground objects. The PKG controllers are used to implement all the navigation algorithms.

As discussed in Chapter 10, the guidance controllers are not designed to fly any kinematically feasible trajectory, but rather geometric trajectories that are restricted to the xy_E-plane. Since circles and straight lines are both geometric and easily calculated, the desired trajectories will be constructed from these shapes.

11.1 Flight

While the aircraft is in flight, it is guided in the Earth's reference frame by defining 3D waypoints that are to be flown through. Each waypoint is defined with a North-, East-, and Down position. This altitude is commanded to the flight guidance controller.

Navigation in the 2D xy_E plane is done by using the algorithm developed by the late professor G. Milne and implemented in [13]. Firstly two points are defined that describe the aircraft's current position and heading, and the next waypoint with its heading. Two departure circles and two arrival circles are connected with a series of straight lines, after which the shortest path is determined. This is shown in Figure 11.1. The resulting flight path is thus defined by first the departure circle, then a straight line and finally the arrival circle. The guidance of the aircraft is then simplified to circle- and straight line tracking.

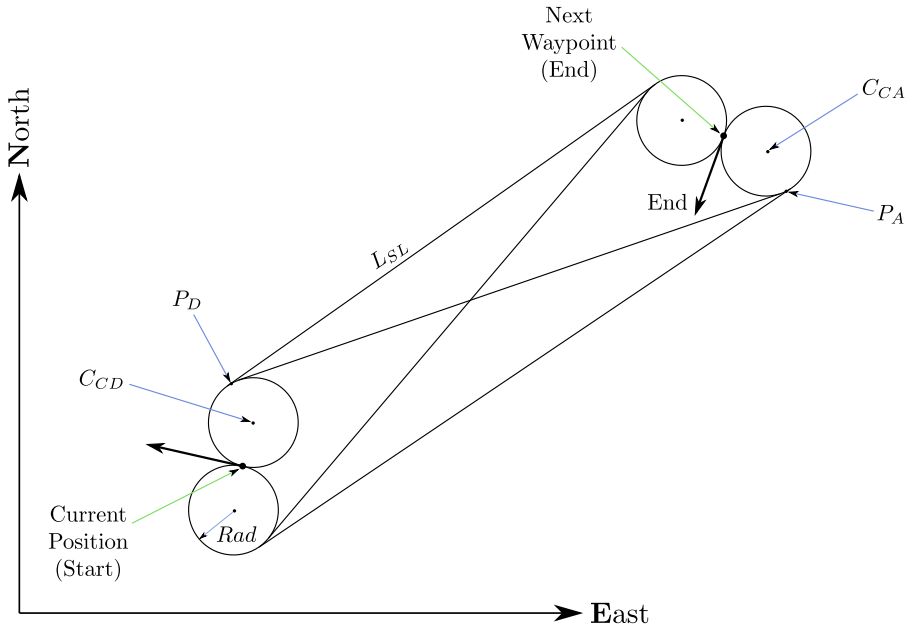

Figure 11.1: Path Planning

The waypoint navigation algorithm defines a couple of points that are used to define the two circles and the straight line. These are shown in Figure 11.1 and listed below.

- C_{CD}: 2D Departure circle centre
- C_{CA}: 2D Arrival circle centre
- *Rad*: Circle radius
- P_D: 2D Point of departure from initial circle to straight line
- P_A: 2D Point of arrival from straight line to final circle
- L_{SL}: Length of straight line
- H_{SL}: Heading of straight line, unit vector
- H_F: Final heading, unit vector

11.1.1 Straight Lines

The cross track position control is done by regulating the perpendicular distance from the trajectory to the aircraft. The departure- (P_D) and arrival points (P_A) are used to define the desired trajectory. The straight line section is deemed completed when the distance travelled from the departure point (P_D) is larger than the length of the straight line (L_{SL}).

11.1.2 Circles

When a circle is flown, the trajectory is defined around the circle's centre at the desired radius. The Trajectory axis is positioned by constructing a straight line from the circle's centre thought the aircraft's current position. The x_T-axis is then perpendicular to this line in the desired direction of rotation. The cross track position (or y_T displacement) is then calculated by comparing the aircraft's current distance to the circle's centre and the desired radius [1].

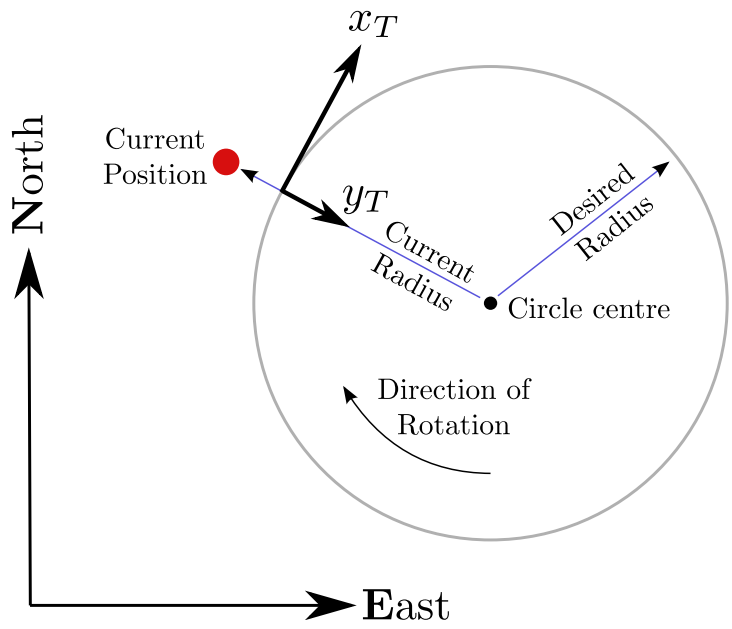

Figure 11.2: Circle Navigation

The circle is considered completed when the aircraft's current heading is within 10° of the departure heading (straight line heading (H_{SL}) in the case of the departure circle, final heading (H_F) in the case of the arrival heading).

Centripetal acceleration

Ignoring any disturbances, the aircraft will experience a centripetal acceleration while flying a constant circle. Since the Trajectory axis moves with the aircraft while flying a circle, there is no implicitly commanded acceleration. To avoid increasing the closed loop frequency of the lateral velocity ($\dot{y}_T$) and decreasing the settling time after transition, a lateral acceleration is fed forward to the lateral Trajectory acceleration ($B_{T_{FF}}$).

[1] This method does not include the correct sign for the y_T measurement, and must be corrected.

Since the radius and y_T-axis are along the same line, the lateral Trajectory acceleration is identical to the desired centripetal acceleration. It is a function of velocity and desired radius, and calculated in Equation 11.1.1. The value of this feedforward term does not contain the required sign. When circling left (looking from above) this term must be negative.

$$|B_{T_{FF}}| = \frac{(\text{Commanded } \overline{V}_a)^2}{\text{Desired } Rad} \tag{11.1.1}$$

11.2 Dynamic Pursuit Navigation

When using a UAV as a surveillance platform equipped with a camera, it would be desirable for the UAV to follow a land- sea based object for extended periods of time. Since conventional fixed wing UAV's are not capable of hovering, it would need to circle the object in order to accomplish this goal. The two main requirements while following an object are:

- The object is to be circled at a constant radius as it aids visual recognition.
- The UAV's airspeed will be assumed constant, since this is how aircraft are practically flown.

11.2.1 Stationary Object

The case where the object is stationary is identical to flying a circle of constant radius, described in Section 11.1.2. The desired path is always tangential to the radius and the lateral acceleration feedforward (described in Equation 11.1.1) is also constant.

11.2.2 Mobile Object

As soon as the object starts moving, the kinematic relationship of Equation 11.1.1 is no longer valid. This is clear through inspection. For example:

When an UAV is travelling in the same direction as the object it is following, and the object is travelling at the same speed as the UAV. Assuming the UAV is abreast the object and at the desired radius, the UAV would simply have to continue flying a straight line to preserve the constant radius criteria. The kinematic relationship of the desired path in this example is one of zero lateral acceleration. Since the required centripetal acceleration is also the lateral feedforward term, this kinematic relationship needs to be investigated.

Figure 11.3 and 11.4 shows a representation of the desired flight path (a constant distance from the object) while the object is travelling a various speeds.

Kinematic Relationship

The kinematic relationship of a point mass circling a moving object at a constant radius is unknown but calculated from the equation describing the position of the aircraft relative to the object. To simplify the derivation the Tracking Plane is defined. It is orientated such that N_{track} is always directed in the direction the object being tracked is moving. In other words, it is the inertial North-East plane rotated through the heading angle of the object (or Tracking Plane's angle (Ψ_{track})).

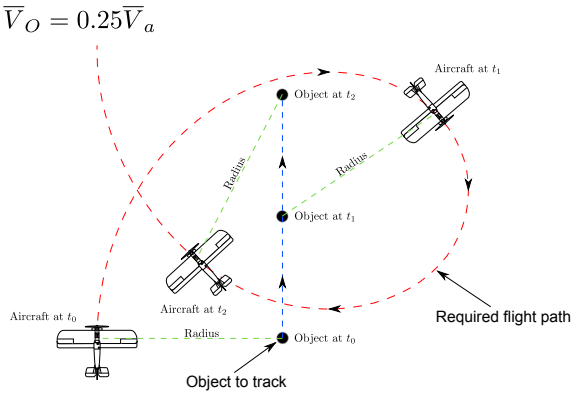

Figure 11.3: The desired path when the object's speed is a quarter of the aircraft's airspeed ($\overline{V}_O = 0.25\overline{V}_a$)

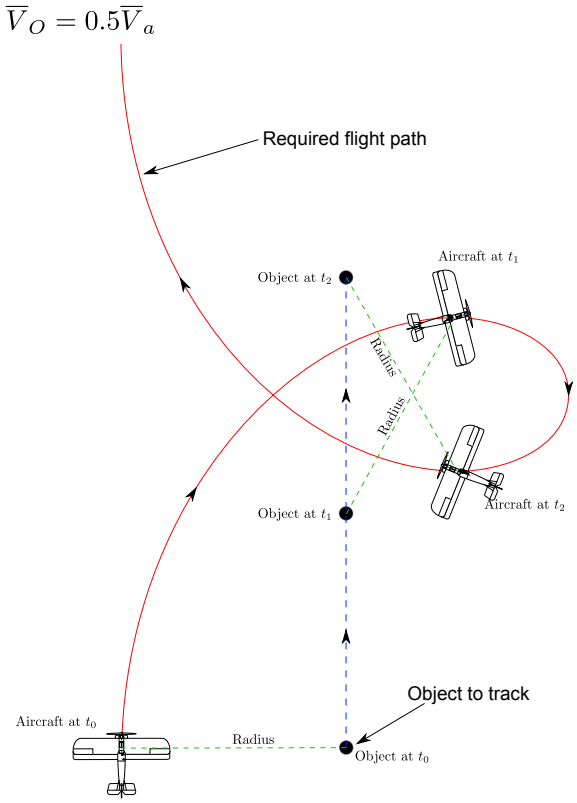

Figure 11.4: The desired path when the object's speed is half that of the aircraft's airspeed ($\overline{V}_O = 0.5\overline{V}_a$)

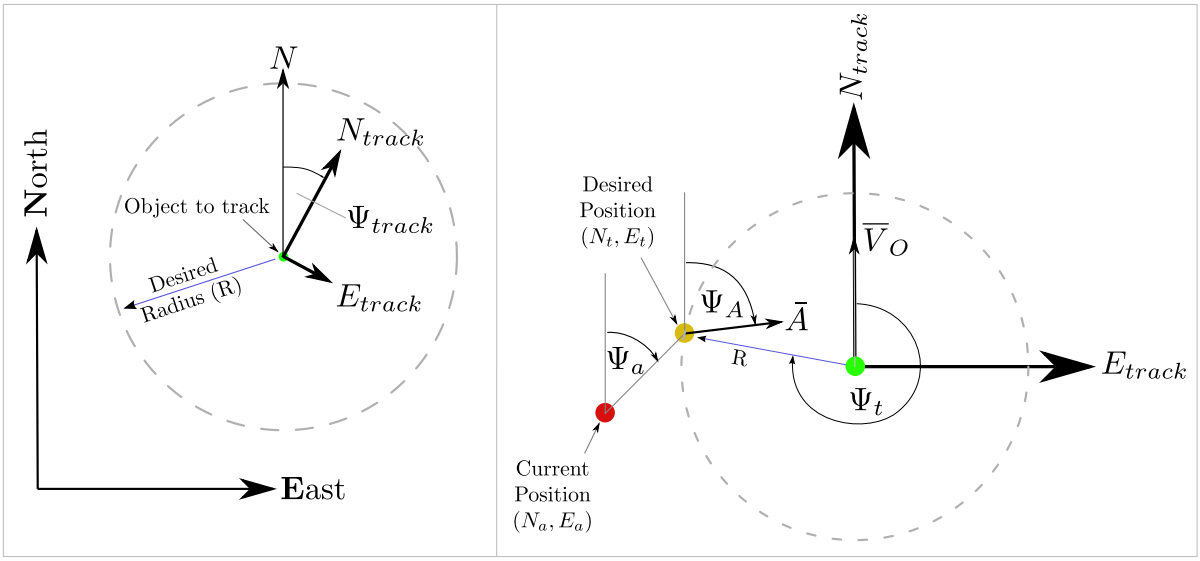

Figure 11.5: Definition of Tracking axis

The desired path on the Tracking Plane is a constant circle around a point which is simple and shown in Equation 11.2.1. The position relationship has been split into scalar equations for ease of understanding and calculation. The equations describing the point mass's accelerations circling the object, is calculated by differentiating the position equation twice. The velocity- and acceleration equations are shown in equations 11.2.2 and 11.2.3 respectively. The derivation of these equations is shown in detail in appendix D.

$$\begin{aligned} P(t) &= P_x(t) + P_y(t) \\ &= [N(t) + R\cos\Psi(t)] + [R\sin\Psi(t)] \qquad (11.2.1) \\ V(t) &= \dot{P}(t) = V_x(t) + V_y(t) \\ &= \left[\dot{N}(t) - R\dot{\Psi}(t)\sin\Psi(t)\right] + \left[R\dot{\Psi}(t)\cos\Psi(t)\right] \qquad (11.2.2) \\ A(t) &= \dot{V}(t) = A_x(t) + A_y(t) \\ &= -R\left[\ddot{\Psi}(t)\sin\Psi(t) + \dot{\Psi}(t)^2\cos\Psi(t)\right] \\ &\quad +R\left[\ddot{\Psi}(t)\cos\Psi(t) - \dot{\Psi}(t)^2\sin\Psi(t)\right] \qquad (11.2.3) \end{aligned}$$

Equations 11.2.1, 11.2.2 and 11.2.3 are all dependant on the desired position of the UAV on the constant radius around the object (N_t, E_t). Another, more desirable, way of describing this position is the heading angle to the desired point on the radius (Ψ_t), from the object.

Figure 11.6 shows the acceleration angle (Ψ_A) variations relative to the radius, while varying Ψ_t. The object is travelling at a constant velocity $(\overline{V}_O)$.

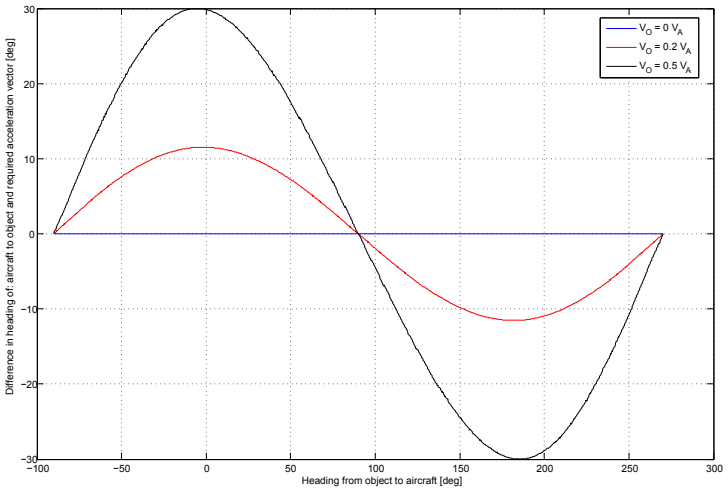

Figure 11.6: Required acceleration vector direction vs. heading from object to point on desired radius.

According to the definition of the Trajectory axis and the outerloop controllers (Chapter 10), x_T is always perpendicular to the required acceleration vector of the trajectory. It is thus clear that x_T is not perpendicular to the tracking circle's radius.

When the UAV is off of the desired radius, it is required that the angle from the UAV to the desired position on the circle (Ψ_a) be equal to the heading of the acceleration vector (Ψ_A) to fulfil the Trajectory axis definition. Equation 11.2.4 describes this criteria mathematically in terms of the UAV's position (N_a, E_a), desired position (N_t, E_t), UAV's velocity $(\overline{V}_a)$ and object

velocity ($\overline{V}_O$). Unfortunately an analytical solution was not found.

$$\begin{aligned}
\Psi_A &= \arctan\left(\frac{E_A - E_t}{N_A - N_t}\right) = \arctan\left(\frac{E_A - R\sin\Psi_t}{N_A - R\cos\Psi_t}\right) \\
\Psi_a &= \arctan\left(\frac{A_y}{A_x}\right) \\
\therefore f_{error}(\Psi_t) &= (E_A - R\sin\Psi_t)\,A_x - (N_A - R\cos\Psi_t)\,A_y \\
&= (E_A - R\sin\Psi_t)\left(\ddot{\Psi}(t)\sin\Psi(t) + \dot{\Psi}(t)^2\cos\Psi(t)\right) \\
&\quad + (N_A - R\cos\Psi_t)\left(\ddot{\Psi}(t)\cos\Psi(t) - \dot{\Psi}(t)^2\sin\Psi(t)\right) \\
&= 0
\end{aligned} \tag{11.2.4}$$

Iterative solution (Newton-Raphson)

The Newton-Raphson iterative method was used[2] to solve for ψ_t. This method aims to minimise the error function (Equation 11.2.4) by varying the value of Ψ_t. The rest of the variables are assumed constant for each solving process. A resulting error function is shown in Figure 11.7. Newton-Raphson uses the current value and the slope of the error function at that point, to propagate where the zero position could be (first order approximation, Equation 11.2.5). It then adjusts the value of Ψ_t with the estimated amount. This process is repeated until the error function reaches a value sufficiently close to zero.

$$\Psi_t[n+1] = \Psi_t[n] \pm \frac{f_{error}(\Psi_t[n])}{\dot{f}_{error}(\Psi_t[n])} \tag{11.2.5}$$

The Newton-Raphson method needs a start value and to ensure convergence, it should be as close to the answer as possible. A good starting value has been found to be the heading from the object to the UAV. This method does however, not always converge. The error function displayed in Figure 11.7 is such an example. This is because the calculated step sizes are hundreds of degrees, causing multiple wrappings of Ψ_t. A limit in step size is introduced to ensure that a solution is found (20° was used).

Due to the small slope of the error function's derivative ($\dot{f}_{error}$) near to the zero crossing, this method may take more time to converge as it jumps between answers on both sides of the zero crossing.

A second constraint is placed on the iteration steps. The step size is halved each time the step direction is changed, which ensures convergence. The corrected angle would still jump around (but in small increments) as the error function approaches zero. However, a sufficiently accurate solution was available after much less time.

A third constraint was placed on the iterative steps. Should the step size fall below a specified value (0.5° was used), it was assumed that Ψ_t was accurate enough. These three constraints cause a significant reduction in iterations, without sacrificing accuracy.

Through inspection it was found that this method only works when the object travels slower than 75% of the UAV's speed. Once this boundary is exceeded, the initial step direction

[2]This might not be the best method, but since this thesis is not aimed at optimal design of the Dynamic Pursuit Navigation algorithm it was deemed sufficient.

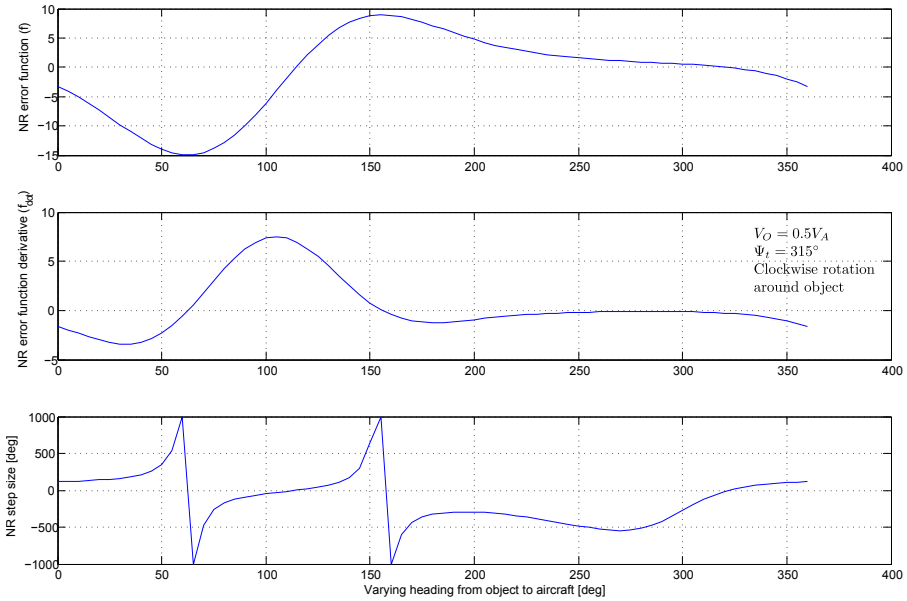

Figure 11.7: Newton-Raphson error functions and corresponding step sizes.

Table 11.1: Reduction in iterations per valid solution (for one specific case), by applying step size constraints

Constraint applied	**Number of iterations**
Constraint 1: Limiting step size	Does not converge
Constraint 2: Halving of step size	51
Constraint 3: Specifying minimum step size	10

is calculated incorrectly and the absolute minimum of the error equation is not found.

In practice, when the object is travelling that fast, the UAV will need to bank at high angles when Ψ_t is in the region of $\pm 90°$ (depending on the direction of rotation). When surveillance is the goal, such high bank angles could cause the camera's view to be obscured by the airframe. In such a case, it is advisable to match the object's speed and fly abreast to it.

11.3 Simulation

In order to validate the Dynamic Pursuit Navigation algorithm, a linear simulation is run where the aircraft is modelled as a kinematic point mass (no dynamics). No guidance controllers are used and an open loop implementation of the algorithm is tested. The results of this simulation is shown in Figure 11.8 and 11.9. Both the desired and actual paths are plotted, and it is clear that the algorithm performs well.

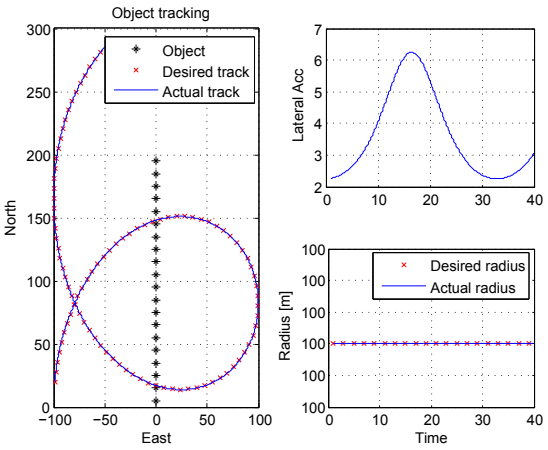

Figure 11.8: Simulation of Dynamic Pursuit Navigation algorithm. This is an open loop implementation, thus no guidance control ($\overline{V}_O = 0.25\overline{V}_a$)

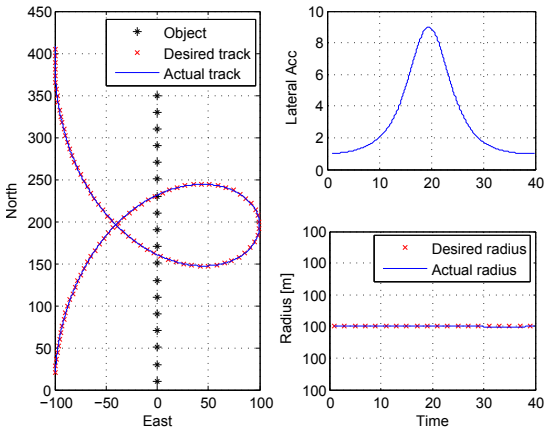

Figure 11.9: Simulation of Dynamic Pursuit Navigation algorithm. This is an open loop implementation, thus no guidance control ($\overline{V}_O = 0.5\overline{V}_a$)

11.4 Summary

This chapter concludes the use of the outerloop controllers designed in Chapter 10 to allow a UAV to fly between specified waypoints and follow a moving object. The performance results of these controllers in a full non-linear simulation environment is shown in the following chapter.

Chapter 12

Flight Control Simulation

All the flight controllers designed in the chapters leading up to this one, are now combined to produce a system that is capable of achieving autonomous Waypoint- and Dynamic Pursuit Navigation. To reduce risk to hardware, a full non-linear 6-DOF HIL simulation is set up in MATLAB®, which includes practical sensor noise and wind disturbances. This chapter discusses these simulated results.

12.1 Waypoint Navigation

Three waypoints are flown with the aircraft staring at a random position. During waypoint flight, the aircraft's airspeed, altitude and 2D position (xy_E-plane) must be regulated. All data on the figures below are plotted from the moment the navigation autopilot is engaged.

12.1.1 Airspeed

Figure 12.1 shows that the airspeed of the aircraft is above the desired value when navigation starts. The airspeed is reduced and reaches its target when the aircraft reaches the desired altitude. The deviations in airspeed are caused by the wind disturbances. During an altitude step (83-96 seconds) the airspeed does not deviate drastically, proving that the airspeed controller will prevent the aircraft from stalling.

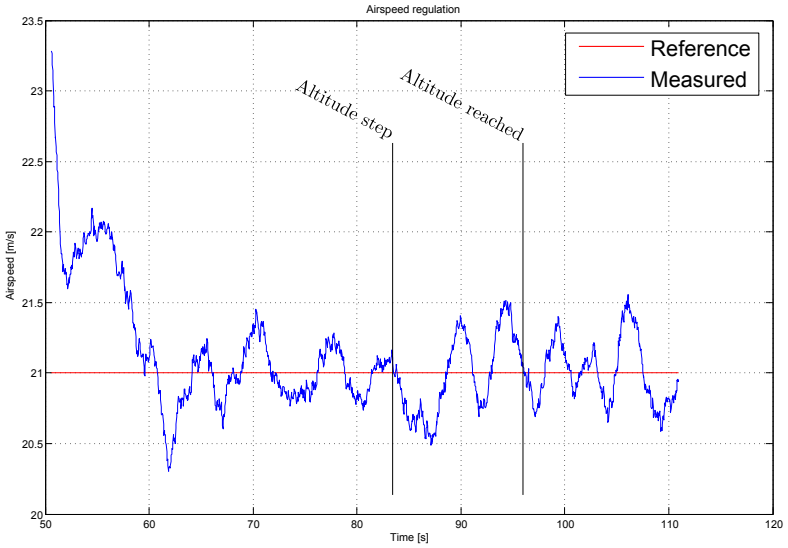

Figure 12.1: Simulated airspeed regulation during navigation

12.1.2 Altitude

Figure 12.2 shows the aircraft's altitude profile. There is a slight steady state error, as the altitude controller does not have integral control. Since this error is small, it is tolerable. The rise time is slower than designed for. This is a result of the climb rate being limited, preventing the aircraft from stalling.

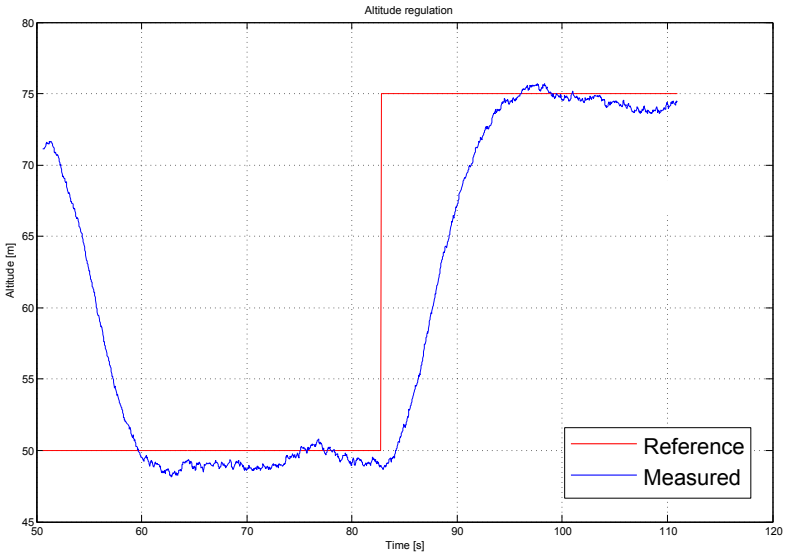

Figure 12.2: Simulated altitude regulation during navigation

12.1.3 Lateral Specific Acceleration regulation

Figure 12.3 shows the regulation of the Lateral Specific Acceleration (B_W during navigation. At 176 seconds, a turn is entered and at 193 seconds it is exited. It is clear that B_W is regulated well around zero.

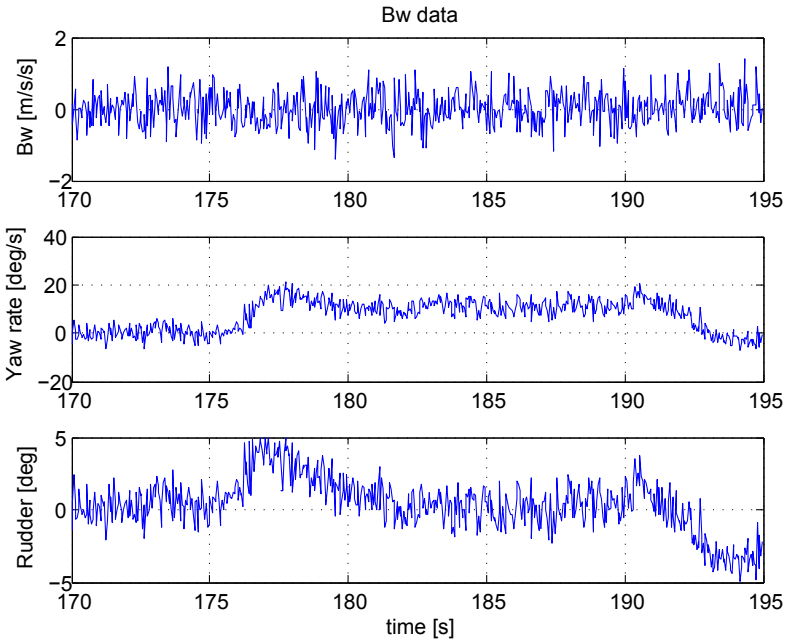

Figure 12.3: Simulated Lateral Specific Acceleration regulation

12.1.4 Position and Cross Track Error

The waypoints, desired flight path and aircraft position during navigation is shown in Figure 12.4. The aircraft tracks the desired path well, even with the presence of wind. Figure 12.5 shows the lateral position deviations off the path. The largest deviations are found when the aircraft transitions into or out of turns.

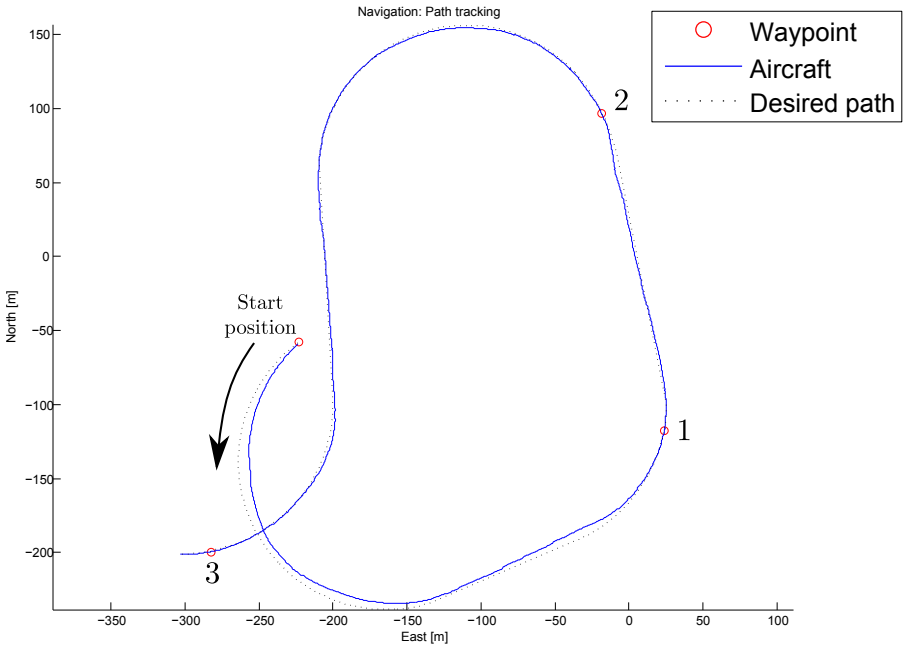

Figure 12.4: Simulated Waypoint navigation

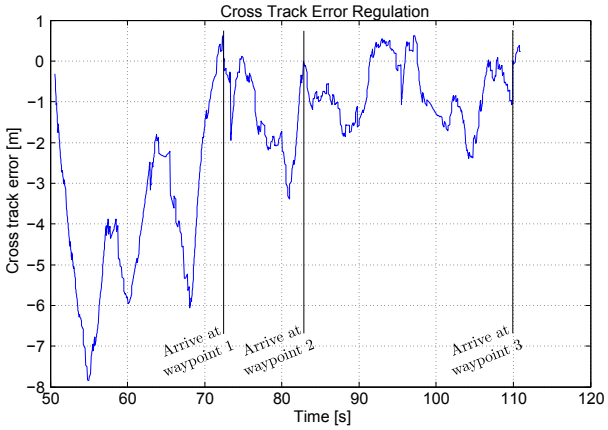

Figure 12.5: Simulated cross track errors during Waypoint navigation

12.2 Dynamic Pursuit Navigation

Since all the controllers used for Dynamic Pursuit Navigation are also used for Waypoint navigation, it serves no purpose in showing them again. The only difference is the lateral acceleration feedforward term ($B_{T_{FF}}$), which influences cross track regulation.

Two simulations are shown of the UAV following a moving object travelling at 50% of the UAV's airspeed. The first simulation uses a constant $B_{T_{FF}}$, while the second uses the iterative method described in Section 11.2.2.

The iterative method drastically improved the effectiveness of the UAV to keep the desired radius. The CTE was reduced from a maximum of 50% to 8%. CTE cannot be eliminated completely as the roll rate dynamics cause lags in the innerloop acceleration vector response.

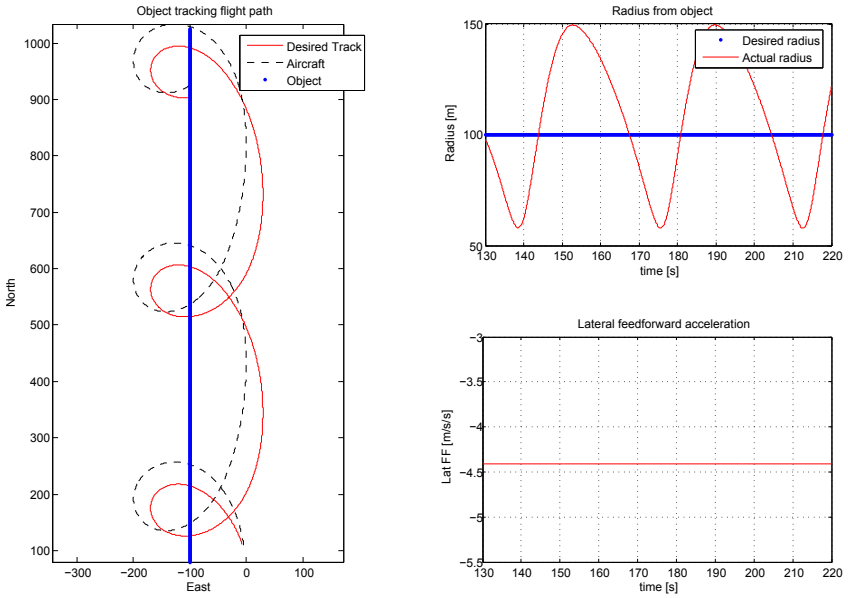

Figure 12.6: Non-linear simulation plot of UAV following a moving object. The object is travelling at $0.5\overline{V}_A$. The lateral acceleration feedforward ($B_{T_{FF}}$) is kept constant.

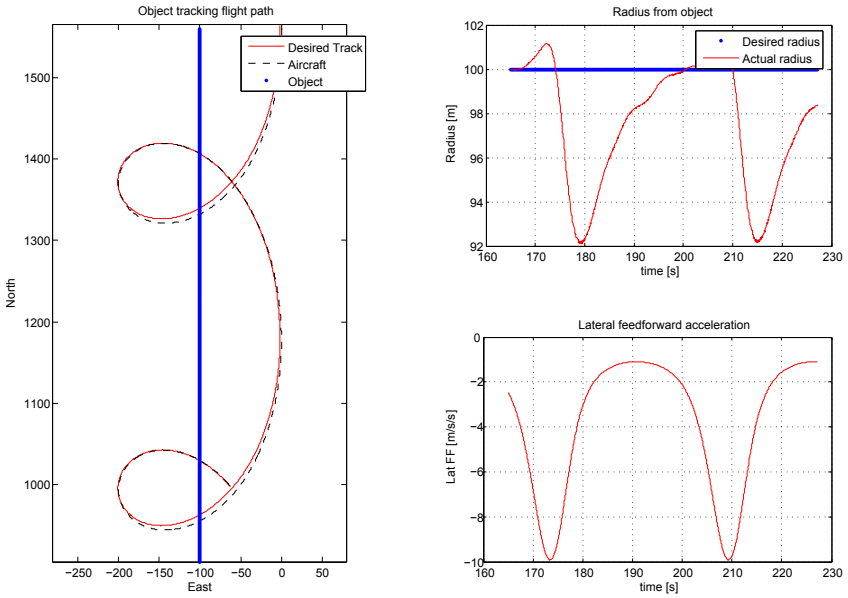

Figure 12.7: Non-linear simulation plot of UAV following a moving object. The object is travelling at $0.5\overline{V}_A$. The lateral acceleration feedforward ($B_{T_{FF}}$) is calculated using the iterative method described in Section 11.2.2.

12.3 Summary

These non-linear simulations have shown that the PKG control architecture performs well when used to implement Waypoint- and Dynamic Pursuit Navigation. The simulations show that the navigation is performed with satisfactory results.

Chapter 13

Conclusion and Recommendations

This concludes the research in this thesis. One of the goals of this thesis has not been achieved, as no practical results of the controllers are available. This is due to a crash during flight preliminary testing (the crash was not caused by the controllers). The remaining time was not sufficient to repair the damage and allow for further test flights.

Despite this setback, a large contribution has been made toward Take-off, flight control (stability and guidance) and object following. Even though these controllers have not been tested practically, the results of the non-linear HIL simulation are encouraging.

13.1 Conclusions

13.1.1 Take-off

Analysis

One of the main goals of the Take-off research was to fully analyse the runway model. This analysis (chapter 5) has given much insight into the transient response of the runway model, as well as the coupling between the undercarriage- and aerodynamic effects during Take-off. Most notably would be the effect of the actuators on the system during the various stages of Take-off.

As seen from the analysis, acceleration based control is difficult to implement due to the plant's complexity. The position and movement of the open loop zeros are not conducive to improving the damping or frequency of the plant through direct feedback from acceleration. Instead, direct feedback of rate was seen to give a far more desirable closed loop response.

Control

Even though the analysis indicated that acceleration based control was not ideal, it was implemented to test its feasibility. The implementation proved very intricate due to the complexity of the plant. This also resulted in limited response rates.

If a controller is required to have an acceleration interface, this can be accomplished by using the steady state relationship between acceleration and rate ($a_Y = UR$). However, there are still limitations.

Low speed The measured accelerations are in the noise floor of low cost accelerometers. Using the steady state relationship, large yaw rates (R) will be required to get the desired accelerations. This will cause large changes in heading to achieve the desired acceleration, which is not ideal.

Medium speed Due to the nature of the system, the closed loop frequency at medium speeds (when the aerodynamic effects become dominant) is fairly low when compared with other speeds. This make control more sluggish at these speeds. This could be critical, as gusts will have a larger effect.

High speed Acceleration control does give satisfactory control over the system at higher speeds. Unfortunately the aircraft will no be able to use this control for very long, as the aircraft will almost be airborne.

The augmented damping provided by the pitch- and roll rate regulators seemed to work well, however this is very difficult to verify while on the runway. Their performance was also tested while in flight, where they gave satisfactory results.

Ramping the throttle during the Groundroll phase eliminated the possibility of noisy sensors corrupting the throttle command and possibly preventing maximum thrust. This also ensures the shortest possible Groundroll.

13.1.2 Waypoint- and Dynamic Pursuit Navigation

The main reason for developing the Dynamic Pursuit Navigation algorithm is to be able to continue surveillance of surface objects, even when they are moving. The algorithm developed in chapter 11 has satisfactory results even though it is not computationally efficient. Its performance degrades when very large bank angles are required, which causes a delay in the production of the required acceleration vector by the aircraft.

The Dynamic Pursuit Navigation algorithm required a position based kinematic flight guidance controller (PKG control) to be successful. This architecture was designed and its implementation enabled the guidance to be independent from a specific airspeed or thrust command. This is particularly useful, as aircraft are generally flown by keeping their airspeed constant.

A new airspeed controller was designed by using the technique of feedback linearisation. It allows regulation (and control) of airspeed to within a small deviation, even when large pitch changes were made. Even though not required for this research, this controller is well suited to aggressive flight control.

13.2 Recommendations

13.2.1 Take-off

- When designing Take-off controllers, it is advised that rate based control is used for three reasons:
  - Rate measurements are less susceptible to noise than accelerometer measurements.
  - Rate based control gives superior results when being used to control the Groundroll of an aircraft due to the shape of the root locus.
  - At low speeds, large accelerations are required to achieve heading changes.
- Even though acceleration based control is not suited to the Take-off problem, the analysis of the undercarriage can be used for other ground based vehicles. These vehicles should travel quite fast in order for the kinematic relationship between lateral acceleration and yaw rate to be viable. This control would also suit navigation around corners better than straight line tracking.

13.2.2 Waypoint- and Dynamic Pursuit Navigation

- The Dynamic Pursuit Navigation algorithm gave good results, but is not very computationally efficient due to the iterative solver employed. Since the control strategy defines this algorithm, further research could be done to find a more efficient control strategy with which to accomplish Dynamic Pursuit Navigation.
- Tracking was done by commanding an arbitrary trim airspeed. The endurance of the aircraft can be extended by flying at a loiter airspeed[1]. Alternatively, the object to be tracked can be approached at cruise airspeed[2].
- The trajectory used for the object following can be investigated. In this research a circle of constant radius is flown around the object, but this is not necessarily the ideal path when a camera is mounted on the aircraft. Flying abreast or behind the object might be more suitable.
- Airspeed is kept constant during tracking in this research. The change in airspeed can be used to form part of the tracking algorithm.

[1] The airspeed that allows maximum flight time
[2] The airspeed that covers the most distance with the least amount of fuel

Appendices

Appendix A

Direction Cosine Matrix

The derivation of the DCM is done in [13] and only stated here. This DCM is based on the Euler 321 attitude description [8]. It is used to coordinate a 3D vector into another axis system.

Assuming a vector coordinated (described) in the axes system 1 ($\mathbf{V}_1$), it can be coordinated in axis system 2 that is rotated through yaw (ψ), pitch (θ) and roll (ϕ), as the vector $\mathbf{V}_2$.

$$\mathbf{V}_2 = \left[\mathbf{DCM}^{21}\right] \mathbf{V}_1$$

where,

$$\mathbf{DCM}^{21} = \begin{bmatrix} (\cos\psi\cos\theta) & (\sin\psi\cos\theta) & (-\sin\theta) \\ \begin{pmatrix} \cos\psi\sin\theta\sin\phi \\ -\sin\psi\cos\phi \end{pmatrix} & \begin{pmatrix} \sin\psi\sin\theta\sin\phi \\ +\cos\psi\cos\phi \end{pmatrix} & (\cos\theta\sin\phi) \\ \begin{pmatrix} \cos\psi\sin\theta\cos\phi \\ +\sin\psi\sin\phi \end{pmatrix} & \begin{pmatrix} \sin\psi\sin\theta\cos\phi \\ -\cos\psi\sin\phi \end{pmatrix} & (\cos\theta\cos\phi) \end{bmatrix}$$

The inverse is also true,

$$\mathbf{V}_1 = \left[\mathbf{DCM}^{21}\right]^{-1} \mathbf{V}_2$$

But the DCM is orthogonal [13], thus the inverse is simply the transposed.

$$\mathbf{V}_1 = \left[\mathbf{DCM}^{21}\right]^{-1} \mathbf{V}_2 = \left[\mathbf{DCM}^{21}\right]^{T} \mathbf{V}_2 = \left[\mathbf{DCM}^{12}\right] \mathbf{V}_2$$

where,

$$\left[\mathbf{DCM}^{21}\right]^{T} = \begin{bmatrix} (\cos\psi\cos\theta) & \begin{pmatrix} \cos\psi\sin\theta\sin\phi \\ -\sin\psi\cos\phi \end{pmatrix} & \begin{pmatrix} \cos\psi\sin\theta\cos\phi \\ +\sin\psi\sin\phi \end{pmatrix} \\ (\sin\psi\cos\theta) & \begin{pmatrix} \sin\psi\sin\theta\sin\phi \\ +\cos\psi\cos\phi \end{pmatrix} & \begin{pmatrix} \sin\psi\sin\theta\cos\phi \\ -\cos\psi\sin\phi \end{pmatrix} \\ (-\sin\theta) & (\cos\theta\sin\phi) & (\cos\theta\cos\phi) \end{bmatrix}$$

Appendix B

Super Frontier Senior 46 physical data

All the physical data that describes the physical properties of the Super Frontier Senior 46 is listed here. This includes mass, moment of inertia, main wing- and undercarriage measurements and stability and control derivatives.

Table B.1: Mass and Moment of Inertia data

m (mass)	5.12	$[kg]$
I_{XX} (x_B-axis moment of inertia)	0.57	$[kg.m^2]$
I_{YY} (y_B-axis moment of inertia)	0.4	$[kg.m^2]$
I_{ZZ} (z_B-axis moment of inertia)	0.992	$[kg.m^2]$

Table B.2: Main wing measurements

S (wing area)	0.78	$[m^2]$
b (wing span)	2.0	$[m]$
c (wing chord length)	0.39	$[m]$

Table B.3: Undercarriage data (all measurements are taken from the CG)

l_s (distance to steering wheel, along x_B)	0.365	$[m]$
l_m (distance to main wheels, along x_B)	0.02	$[m]$
l_l (distance to left wheel, along y_B)	0.26	$[m]$
l_r (distance to right wheel, along y_B)	0.26	$[m]$
$C_{\alpha\alpha}$ (tire cornering coefficient)	0.25	$[\frac{1}{rad}]$

Stability and control derivatives of an airframe give a mathematical description of the forces and moments created by the airframe and control surfaces of an aircraft. These derivatives that describe the Super Frontier Senior 46 airframe are listed below. The unit of all derivatives are $\frac{1}{rad}$.

Table B.4: Stability and control derivatives

Output due to:	α		β	
Z force	C_{L_α} =	3.326826	C_{L_β} =	0.000000
Y force	C_{Y_α} =	0.000000	C_{Y_β} =	-0.200573
P (rolling moment)	C_{l_α} =	0.000000	C_{l_β} =	-0.041078
Q (pitching moment)	C_{m_α} =	-0.978701	C_{m_β} =	0.000000
R (yawing moment)	C_{n_α} =	0.000000	C_{n_β} =	0.081422

Output due to:	P (roll rate)		Q (pitch rate)		R (yaw rate)	
Z force	C_{L_p} =	0.000000	C_{L_q} =	6.852467	C_{L_r} =	0.000000
Y force	C_{Y_p} =	-0.069309	C_{Y_q} =	0.000000	C_{Y_r} =	0.188733
P (rolling moment)	C_{l_p} =	-0.316317	C_{l_q} =	0.000000	C_{l_r} =	0.018895
Q (pitching moment)	C_{m_p} =	0.000000	C_{m_q} =	-10.593742	C_{m_r} =	0.000000
R (yawing moment)	C_{n_p} =	0.005306	C_{n_q} =	0.000000	C_{n_r} =	-0.079365

Output due to:	δ_A (aileron)		δ_E (elevator)		δ_R (rudder)	
Z force	$C_{L_{\delta_A}}$ =	0.000000	$C_{L_{\delta_E}}$ =	0.531288	$C_{L_{\delta_R}}$ =	0.000000
Y force	$C_{Y_{\delta_A}}$ =	-0.015387	$C_{Y_{\delta_E}}$ =	0.000000	$C_{Y_{\delta_R}}$ =	0.125860
P (rolling moment)	$C_{l_{\delta_A}}$ =	-0.136923	$C_{l_{\delta_E}}$ =	0.000000	$C_{l_{\delta_R}}$ =	0.010171
Q (pitching moment)	$C_{m_{\delta_A}}$ =	0.000000	$C_{m_{\delta_E}}$ =	-1.280891	$C_{m_{\delta_R}}$ =	0.000000
R (yawing moment)	$C_{n_{\delta_A}}$ =	-0.001181	$C_{n_{\delta_E}}$ =	0.000000	$C_{n_{\delta_R}}$ =	-0.057615

Appendix C

Linearising the Runway Model

Dynamic Equations

The mathematical model of the lateral runway mode is derived in chapter 3, and converted to contain β and R states. This appendix goes through the mathematical detail of linearising this model.

$$\begin{aligned} \dot{\beta} &= \frac{Y_U + Y_a}{mU} - R \\ \dot{R} &= \frac{N_U + N_a}{I_z} \end{aligned} \tag{C.0.1}$$

The dynamic equations for the lateral runway model (Equation 5.2.3) are stated here for convenience. First step is to expanded and simplify the forces and moments. As the aerodynamic forces and moments are already in linear form, the undercarriage forces will be linearised first.

$$\begin{aligned} Y_U =& Y_s + Y_l + Y_r \\ =& N_S C_{\alpha\alpha} \left[\arctan\left(\frac{V + l_s R}{U} \right) + \delta_S \right] \cos\left(-\delta_S\right) - N_S \cdot \mu_f \sin\left(-\delta_S\right) \\ &+ N_L C_{\alpha\alpha} \left[\arctan\left(\frac{V - l_m R}{U + \frac{l_w}{2} R} \right) \right] + N_R C_{\alpha\alpha} \left[\arctan\left(\frac{V - l_m R}{U - \frac{l_w}{2} R} \right) \right] \end{aligned} \tag{C.0.2}$$

Applying the β conversion (Equation 5.2.2), and ignoring friction,

$$\begin{aligned} Y_U =& N_S C_{\alpha\alpha} \left[\arctan\left(\frac{\overline{V} \sin(\beta) + l_s R}{U} \right) + \delta_S \right] \cos\left(-\delta_S\right) \\ &+ N_L C_{\alpha\alpha} \left[\arctan\left(\frac{\overline{V} \sin(\beta) - l_m R}{U + \frac{l_w}{2} R} \right) \right] + N_R C_{\alpha\alpha} \left[\arctan\left(\frac{\overline{V} \sin(\beta) - l_m R}{U - \frac{l_w}{2} R} \right) \right] \end{aligned} \tag{C.0.3}$$

Applying small angle assumptions,

$$\begin{aligned} Y_U =& N_S C_{\alpha\alpha}\left(\frac{\overline{V}\beta + l_s R}{U} + \delta_S\right) \\ &+ N_L C_{\alpha\alpha}\left(\frac{\overline{V}\beta - l_m R}{U + \frac{l_w}{2}R}\right) + N_R C_{\alpha\alpha}\left(\frac{\overline{V}\beta - l_m R}{U - \frac{l_w}{2}R}\right) \end{aligned} \tag{C.0.4}$$

As discussed in chapter 5,

$$\begin{aligned} \overline{V} &\approx U \\ \text{And} \quad U &\gg \frac{l_w}{2}R \\ \therefore U \pm \frac{l_w}{2}R &\approx U \end{aligned}$$

$$\begin{aligned} Y_U =& N_S C_{\alpha\alpha}\left(\beta + \frac{l_s}{U}R + \delta_S\right) \\ &+ N_L C_{\alpha\alpha}\left(\frac{U}{U}\beta - \frac{l_m}{U}R\right) + N_R C_{\alpha\alpha}\left(\frac{U}{U}\beta - \frac{l_m}{U}R\right) \end{aligned} \tag{C.0.5}$$

The undercarriage moments are the forces that act on a moment arm. The undercarriage moments are thus,

$$\begin{aligned} M_U =& l_s Y_s - l_m Y_l - l_m Y_r \\ =& l_s N_s C_{\alpha\alpha}\left(\beta + \frac{l_s}{U}R + \delta_s\right) \\ &- l_m N_s C_{\alpha\alpha}\left(\beta - \frac{l_m}{U}R\right) - l_m N_s C_{\alpha\alpha}\left(\beta - \frac{l_m}{U}R\right) \end{aligned} \tag{C.0.6}$$

Substituting the undercarriage- and aerodynamic forces, the $\dot{\beta}$ equation expands to,

$$\begin{aligned} \dot{\beta} =& \frac{N_s C_{\alpha\alpha}}{mU}\left(\beta + \frac{l_s}{U}R + \delta_s\right) + \frac{N_l C_{\alpha\alpha}}{mU}\left(\beta - \frac{l_m}{U}R\right) + \frac{N_r C_{\alpha\alpha}}{mU}\left(\beta - \frac{l_m}{U}R\right) \\ &+ \frac{\bar{q}S}{m\overline{V}_a}\left(C_{y_\beta}\beta + \frac{b}{2\overline{V}_a}C_{y_r}R + C_{y_{\delta_R}}\delta_R\right) - R \end{aligned} \tag{C.0.7}$$

Expanding the $\dot{R}$ equation in the same way,

$$\begin{aligned} \dot{R} =& \frac{l_s N_s C_{\alpha\alpha}}{I_z}\left(\beta + \frac{l_s}{U}R + \delta_s\right) - \frac{l_m N_l C_{\alpha\alpha}}{I_z}\left(\beta - \frac{l_m}{U}R\right) - \frac{l_m N_r C_{\alpha\alpha}}{I_z}\left(\beta - \frac{l_m}{U}R\right) \\ &+ \frac{\bar{q}Sb}{I_z}\left(C_{n_\beta}\beta + \frac{b}{2\overline{V}_a}C_{n_r}R + C_{n_{\delta_R}}\delta_R\right) \end{aligned} \tag{C.0.8}$$

Isolating the effect of each state to the dynamic equation, can be done by determining the partial derivative of the dynamic equation with respect to the state. The system is linearised about a certain work point, by substituting the parameters of the work point into the derivative. As the aircraft will be travelling down a straight runway, this will become the work point

(with $\beta = R = 0$). The state space representation of this coupled system is thus,

$$\begin{bmatrix} \dot{\beta} \\ \dot{R} \end{bmatrix} = \begin{bmatrix} \frac{\partial \dot{\beta}}{\partial \beta} & \frac{\partial \dot{\beta}}{\partial R} \\ \frac{\partial \dot{R}}{\partial \beta} & \frac{\partial \dot{R}}{\partial R} \end{bmatrix} \begin{bmatrix} \beta \\ R \end{bmatrix} + \begin{bmatrix} \frac{\partial \dot{\beta}}{\partial \delta_s} & \frac{\partial \dot{\beta}}{\partial \delta_R} \\ \frac{\partial \dot{R}}{\partial \delta_s} & \frac{\partial \dot{R}}{\partial \delta_R} \end{bmatrix} \begin{bmatrix} \delta_s \\ \delta_R \end{bmatrix} \tag{C.0.9}$$

The partial derivatives with respect to the states are,

$$\begin{aligned} \frac{\partial \dot{\beta}}{\partial \beta} &= \frac{NC_{\alpha\alpha}}{mU} + \frac{\bar{q}SC_{y_\beta}}{m\overline{V}_a} & \frac{\partial \dot{\beta}}{\partial R} &= \frac{\bar{q}SbC_{y_r}}{2m\overline{V}_a^2} - 1 \\ \frac{\partial \dot{R}}{\partial \beta} &= \frac{\bar{q}SbC_{n_\beta}}{I_z} & \frac{\partial \dot{R}}{\partial R} &= \frac{l_s l_m NC_{\alpha\alpha}}{I_z U} + \frac{\bar{q}Sb^2C_{n_r}}{2I_z\overline{V}_a} \end{aligned}$$

$$\begin{aligned} \frac{\partial \dot{\beta}}{\partial \delta_s} &= \frac{l_m}{l_s + l_m}\frac{NC_{\alpha\alpha}}{mU} & \frac{\partial \dot{\beta}}{\partial \delta_R} &= \frac{\bar{q}SC_{y_{\delta_R}}}{m\overline{V}_a} \\ \frac{\partial \dot{R}}{\partial \delta_s} &= \frac{l_s l_m}{l_s + l_m}\frac{NC_{\alpha\alpha}}{I_z} & \frac{\partial \dot{R}}{\partial \delta_R} &= \frac{\bar{q}SbC_{n_{\delta_R}}}{I_z} \end{aligned} \tag{C.0.10}$$

Output Equations

The two states are β and R. R is directly measurable from the z_B-axis rate gyro sensor. It is not possible to measure β with conventional inertial sensors or GPS. a_Y is an inertial measurement that is a function of the forces applied to the body, scaled with its mass. As the forces are directly related to β, the a_Y measurement will contain information of β. The kinematic relationship between a_Y and Y is used to define the output equation for the state space model.

$$\begin{aligned} a_Y &= \frac{Y_U + Y_a}{m} \\ &= \frac{N_s C_{\alpha\alpha}}{m}\left(\beta + \frac{l_s}{U}R + \delta_s\right) + \frac{N_l C_{\alpha\alpha}}{m}\left(\beta - \frac{l_m}{U}R\right) \\ &+ \frac{N_r C_{\alpha\alpha}}{m}\left(\beta - \frac{l_m}{U}R\right) + \frac{\bar{q}S}{m}\left(C_{y_\beta}\beta + \frac{b}{2\overline{V}_a}C_{y_r}R + C_{y_{\delta_R}}\delta_R\right) \\ &= \left(\frac{NC_{\alpha\alpha}}{m} + \frac{\bar{q}SC_{y_\beta}}{m}\right)\beta + \left(\frac{\bar{q}S}{m}\frac{b}{2U}C_{y_r}\right)R \\ &+ \left(\frac{l_m}{l_s + l_m}\frac{NC_{\alpha\alpha}}{m}\right)\delta_s + \left(\frac{\bar{q}SC_{y_{\delta_R}}}{m}\right)\delta_R \end{aligned} \tag{C.0.11}$$

Applying the same techniques as for the dynamic equations, the output equations are a function of the partial derivatives. R is a linear combination of the states, thus no derivative need to be calculated.

$$\begin{bmatrix} a_Y \\ R \end{bmatrix} = \begin{bmatrix} \frac{\partial a_Y}{\partial \beta} & \frac{\partial a_Y}{\partial R} \\ 0 & 1 \end{bmatrix} \begin{bmatrix} \beta \\ R \end{bmatrix} + \begin{bmatrix} \frac{\partial a_Y}{\partial \delta_s} & \frac{\partial a_Y}{\partial \delta_R} \\ 0 & 0 \end{bmatrix} \begin{bmatrix} \delta_s \\ \delta_R \end{bmatrix} \tag{C.0.12}$$

The partial derivatives with respect to the a_Y output is,

$$\begin{aligned} \frac{\partial a_Y}{\partial \beta} &= \frac{NC_{\alpha\alpha}}{m} + \frac{\bar{q}SC_{y_\beta}}{m} & \frac{\partial a_Y}{\partial R} &= \frac{\bar{q}S}{m}\frac{bC_{y_r}}{2\overline{V}_a} \\ \frac{\partial a_Y}{\partial \delta_s} &= \frac{l_m}{l_s + l_m}\frac{NC_{\alpha\alpha}}{m} & \frac{\partial a_Y}{\partial \delta_R} &= \frac{\bar{q}SC_{y_{\delta_R}}}{m} \end{aligned} \tag{C.0.13}$$

Appendix D

Derivation of acceleration vector required for Dynamic Pursuit Navigation

This appendix serves to explain the mathematical derivation of the kinematic position, velocity and acceleration equations (11.2.1, 11.2.2, 11.2.3). The required acceleration is derived from the position equation by differentiating it twice. All the measurements in this appendix are relative to the Tracking Plane.

D.1 Position

The inertial position vector of the aircraft can be described using object as the centre of the desired circle, which is described as,

$$\begin{aligned} \mathbf{P}(t) &= \mathbf{P}^C(t) + R\mathbf{r}^C(t) \\ &= \mathbf{P}_x(t) + \mathbf{P}_y(t) \end{aligned} \tag{D.1.1}$$

where

$$\begin{aligned} \mathbf{P}^C(t) &= N(t)\,\mathbf{i} + E(t)\,\mathbf{j} \\ \mathbf{r}^C(t) &= \cos\psi(t)\,\mathbf{i} + \sin\psi(t)\,\mathbf{j} \end{aligned} \tag{D.1.2}$$

and

$$\begin{aligned} P_x(t) &= N(t) + R\cos\psi(t) \\ P_y(t) &= R\sin\psi(t) \end{aligned} \tag{D.1.3}$$

D.2 Velocity

The velocity vector is the derivative of the position vector.

$$\begin{aligned}
\mathbf{V}(t) &= \frac{d}{dt}\left[\mathbf{P}_x(t)\,\mathbf{i} + \mathbf{P}_y(t)\,\mathbf{j}\right] \\
&= \frac{d}{dt}\left\{\left[N(t) + R\cos\psi(t)\right]\mathbf{i} + \left[R\sin\psi(t)\right]\mathbf{j}\right\} \\
&= \left[\dot{N}(t) + R\dot{\psi}(t)\sin\psi(t)\right]\mathbf{i} + \left[R\dot{\psi}(t)\cos\psi(t)\right]\mathbf{j} \\
&= V_x(t)\,\mathbf{i} + V_y(t)\,\mathbf{j} \qquad \text{(D.2.1)}
\end{aligned}$$

but,

$$\begin{aligned}
\overline{V}_g &= \sqrt{V_x^2(t) + V_y^2(t)} \\
\overline{V}_g^2 &= V_x^2(t) + V_y^2(t) \\
&= \left[\dot{N}(t) + R\dot{\psi}(t)\sin\psi(t)\right]^2 + \left[R\dot{\psi}(t)\cos\psi(t)\right]^2 \\
&= \dot{N}^2(t) - 2R\dot{N}(t)\,\dot{\psi}(t)\sin\psi(t) + R^2\dot{\psi}^2(t)\sin^2\psi(t) + R^2\dot{\psi}^2(t)\cos^2\psi(t)
\end{aligned}$$

$$\begin{aligned}
\therefore 0 &= \dot{N}^2(t) - 2R\dot{N}(t)\,\dot{\psi}(t)\sin\psi(t) + R^2\dot{\psi}^2(t) - \overline{V}_g^2 \\
&= \left[R^2\right]\dot{\psi}^2(t) - \left[2R\dot{N}(t)\sin\psi(t)\right]\dot{\psi}(t) + \left[\dot{N}^2(t) - \overline{V}_g^2\right] \qquad \text{(D.2.2)}
\end{aligned}$$

and the only unknown is $\dot{\psi}(t)$.

$$\begin{aligned}
\psi(t) &= \frac{2R\dot{N}(t)\sin\psi(t) \pm \sqrt{\left(-2R\dot{N}(t)\sin\psi(t)\right)^2 - 4R^2\left(\dot{N}(t) - \overline{V}_g^2\right)}}{2R^2} \\
&= \frac{\dot{N}(t)\sin\psi(t) \pm \sqrt{\dot{N}^2(t)\sin^2\psi(t) - \dot{N}^2(t) + \overline{V}_g^2}}{R} \\
&= \frac{\dot{N}(t)\sin\psi(t) \pm \sqrt{\overline{V}_g^2 - \dot{N}^2(t)\cos^2\psi(t)}}{R} \qquad \text{(D.2.3)}
\end{aligned}$$

$$\begin{aligned}
\text{where} \quad \psi(t) &= \frac{\dot{N}(t)\sin\psi(t) + \sqrt{\overline{V}_g^2 - \dot{N}^2(t)\cos^2\psi(t)}}{R} \quad \text{for clockwise circling} \\
\text{and} \quad \psi(t) &= \frac{\dot{N}(t)\sin\psi(t) - \sqrt{\overline{V}_g^2 - \dot{N}^2(t)\cos^2\psi(t)}}{R} \quad \text{for anti-clockwise circling} \qquad \text{(D.2.4)}
\end{aligned}$$

D.3 Acceleration

The forward speed of the object (centre of the circle) is assumed constant.

$$\begin{aligned}
\mathbf{A}(t) &= \frac{d}{dt}\left[\mathbf{V}_x(t)\,\mathbf{i} + \mathbf{V}_y(t)\,\mathbf{j}\right] \\
&= \frac{d}{dt}\left\{\left[\dot{N}(t) + R\dot{\psi}(t)\sin\psi(t)\right]\mathbf{i} + \left[R\dot{\psi}(t)\cos\psi(t)\right]\mathbf{j}\right\} \\
&= -R\left[\ddot{\psi}(t)\sin\psi(t) + \dot{\psi}^2(t)\cos\psi(t)\right]\mathbf{i} + R\left[\ddot{\psi}(t)\cos\psi(t) - \dot{\psi}^2(t)\sin\psi(t)\right]\mathbf{j} \\
&= A_x(t)\,\mathbf{i} + A_y(t)\,\mathbf{j} \qquad \text{(D.3.1)}
\end{aligned}$$

D.3.1 Trajectory axis relationship (clockwise relationship)

Analysing clockwise rotation.

$$\begin{aligned}
\psi_T(t) &= \psi(t) + 90^\circ \\
\therefore \psi(t) &= \psi_T(t) - 90^\circ \\
\sin\psi_T(t) &= \sin(\psi(t) + 90^\circ) = \cos\psi(t) \\
\cos\psi_T(t) &= \cos(\psi(t) + 90^\circ) = -\sin\psi(t)
\end{aligned}$$

Transforming from inertial- ($\mathbf{A}^I$) to Trajectory axis accelerations ($\mathbf{A}^T$),

$$\begin{aligned}
\mathbf{A}^T &= \begin{bmatrix} \cos\psi_T(t) & \sin\psi_T(t) \\ -\sin\psi_T(t) & \cos\psi_T(t) \end{bmatrix} \mathbf{A}^I \\
\begin{bmatrix} A_T \\ B_T \end{bmatrix} &= \begin{bmatrix} \cos\psi_T(t) & \sin\psi_T(t) \\ -\sin\psi_T(t) & \cos\psi_T(t) \end{bmatrix} \begin{bmatrix} A_x \\ B_x \end{bmatrix} \\
&= \begin{bmatrix} \cos\psi_T(t) & \sin\psi_T(t) \\ -\sin\psi_T(t) & \cos\psi_T(t) \end{bmatrix} \begin{bmatrix} -R\ddot{\psi}(t)\sin\psi(t) - R\dot{\psi}^2(t)\cos\psi(t) \\ R\ddot{\psi}(t)\cos\psi(t) - R\dot{\psi}^2(t)\sin\psi(t) \end{bmatrix}
\end{aligned} \qquad \text{(D.3.2)}$$

The required lateral acceleration is B_T.

$$\begin{aligned}
B_T &= -\sin\psi_T(t)\left[-R\ddot{\psi}(t)\sin\psi(t) - R\dot{\psi}^2(t)\cos\psi(t)\right] \\
&\quad + \cos\psi_T(t)\left[R\ddot{\psi}(t)\cos\psi(t) - R\dot{\psi}^2(t)\sin\psi(t)\right] \\
&= -\cos\psi(t)\left[-R\ddot{\psi}(t)\sin\psi(t) - R\dot{\psi}^2(t)\cos\psi(t)\right] \\
&\quad - \sin\psi(t)\left[R\ddot{\psi}(t)\cos\psi(t) - R\dot{\psi}^2(t)\sin\psi(t)\right] \\
&= R\ddot{\psi}(t)\sin\psi(t)\cos\psi(t) + R\dot{\psi}^2(t)\cos^2\psi(t) \\
&\quad - R\ddot{\psi}(t)\cos\psi(t)\sin\psi(t) + R\dot{\psi}^2(t)\sin^2\psi(t) \\
&= R\dot{\psi}^2(t) \qquad \text{(D.3.3)}
\end{aligned}$$

But since $\dot{\psi}(t)$ is known,

$$\begin{aligned}
\dot{\psi}^2(t) &= \left[\frac{\dot{N}(t)\sin\psi(t) + \sqrt{\overline{V}_g^2 - \dot{N}^2(t)\cos^2\psi(t)}}{R}\right]^2 \\
&= \frac{1}{R^2}\left[\dot{N}(t)\sin\psi(t) + \sqrt{\overline{V}_g^2 - \dot{N}^2(t)\cos^2\psi(t)}\right]^2 \\
&= \frac{1}{R^2}\left[\begin{array}{c}\dot{N}^2(t)\sin^2\psi(t) + \overline{V}_g^2 - \dot{N}^2(t)\cos^2\psi(t) \\ +2\dot{N}(t)\sin\psi(t)\sqrt{\overline{V}_g^2 - \dot{N}^2(t)\cos^2\psi(t)}\end{array}\right] \\
&= \frac{1}{R^2}\left[\begin{array}{c}\overline{V}_g^2 - \dot{N}^2(t)\left(\cos^2\psi(t) - \sin^2\psi(t)\right) \\ +2\dot{N}(t)\sin\psi(t)\sqrt{\overline{V}_g^2 - \dot{N}^2(t)\cos^2\psi(t)}\end{array}\right] \\
&= \frac{1}{R^2}\left\{\overline{V}_g^2 + \dot{N}(t)\left[2\sin\psi(t)\sqrt{\overline{V}_g^2 - \dot{N}^2(t)\cos^2\psi(t)} - \dot{N}(t)\cos 2\psi(t)\right]\right\}
\end{aligned} \tag{D.3.4}$$

Therefore B_T for clockwise rotation is,

$$B_T = \frac{1}{R}\left\{\overline{V}_g^2 + \dot{N}(t)\left[2\sin\psi(t)\sqrt{\overline{V}_g^2 - \dot{N}^2(t)\cos^2\psi(t)} - \dot{N}(t)\cos 2\psi(t)\right]\right\} \tag{D.3.5}$$

The second derivative of $\psi(t)$ is,

$$\begin{aligned}
\ddot{\psi}(t) &= \frac{d}{dt}\left[\frac{\dot{N}(t)\sin\psi(t) + \sqrt{\overline{V}_g^2 - \dot{N}^2(t)\cos^2\psi(t)}}{R}\right] \\
&= \frac{1}{R}\left[\dot{N}(t)\dot{\psi}(t)\cos\psi(t) + \frac{\dot{N}^2(t)\dot{\psi}(t)\cos\psi(t)\sin\psi(t)}{\sqrt{\overline{V}_g^2 - \dot{N}^2(t)\cos^2\psi(t)}}\right] \\
&= \frac{\dot{N}(t)\dot{\psi}(t)\cos\psi(t)}{R}\left[1 + \frac{\dot{N}^2(t)\sin\psi(t)}{\sqrt{\overline{V}_g^2 - \dot{N}^2(t)\cos^2\psi(t)}}\right]
\end{aligned} \tag{D.3.6}$$

D.3.2 Trajectory axis relationship (anti-clockwise relationship)

Analysing anti-clockwise rotation.

$$\begin{aligned}
\psi_T(t) &= \psi(t) - 90^\circ \\
\therefore \psi(t) &= \psi_T(t) + 90^\circ \\
\sin\psi_T(t) &= \sin(\psi(t) - 90^\circ) = -\cos\psi(t) \\
\cos\psi_T(t) &= \cos(\psi(t) - 90^\circ) = \sin\psi(t)
\end{aligned} \tag{D.3.7}$$

The required lateral acceleration, B_T

$$\begin{aligned} B_T &= -\sin\psi_T(t)\left[-R\ddot{\psi}(t)\sin\psi(t) - R\dot{\psi}^2(t)\cos\psi(t)\right] \\ &\quad +\cos\psi_T(t)\left[R\ddot{\psi}(t)\cos\psi(t) - R\dot{\psi}^2(t)\sin\psi(t)\right] \\ &= \cos\psi(t)\left[-R\ddot{\psi}(t)\sin\psi(t) - R\dot{\psi}^2(t)\cos\psi(t)\right] \\ &\quad +\sin\psi(t)\left[R\ddot{\psi}(t)\cos\psi(t) - R\dot{\psi}^2(t)\sin\psi(t)\right] \\ &= -R\ddot{\psi}(t)\sin\psi(t)\cos\psi(t) - R\dot{\psi}^2(t)\cos^2\psi(t) \\ &\quad +R\ddot{\psi}(t)\cos\psi(t)\sin\psi(t) - R\dot{\psi}^2(t)\sin^2\psi(t) \\ &= -R\dot{\psi}^2(t) \end{aligned} \tag{D.3.8}$$

But since $\dot{\psi}(t)$ is known,

$$\begin{aligned} \dot{\psi}^2(t) &= \left[\frac{\dot{N}(t)\sin\psi(t) - \sqrt{\overline{V}_g^2 - \dot{N}^2(t)\cos^2\psi(t)}}{R}\right]^2 \\ &= \frac{1}{R^2}\left[\dot{N}(t)\sin\psi(t) - \sqrt{\overline{V}_g^2 - \dot{N}^2(t)\cos^2\psi(t)}\right]^2 \\ &= \frac{1}{R^2}\left[\begin{array}{c} \dot{N}^2(t)\sin^2\psi(t) + \overline{V}_g^2 - \dot{N}^2(t)\cos^2\psi(t) \\ -2\dot{N}(t)\sin\psi(t)\sqrt{\overline{V}_g^2 - \dot{N}^2(t)\cos^2\psi(t)} \end{array}\right] \\ &= \frac{1}{R^2}\left[\begin{array}{c} \overline{V}_g^2 - \dot{N}^2(t)\left(\cos^2\psi(t) - \sin^2\psi(t)\right) \\ -2\dot{N}(t)\sin\psi(t)\sqrt{\overline{V}_g^2 - \dot{N}^2(t)\cos^2\psi(t)} \end{array}\right] \\ &= \frac{1}{R^2}\left\{\overline{V}_g^2 + \dot{N}(t)\left[-2\sin\psi(t)\sqrt{\overline{V}_g^2 - \dot{N}^2(t)\cos^2\psi(t)} - \dot{N}(t)\cos 2\psi(t)\right]\right\} \end{aligned} \tag{D.3.9}$$

Therefore B_T for anti-clockwise rotation is,

$$B_T = \frac{-1}{R}\left\{\overline{V}_g^2 + \dot{N}(t)\left[-2\sin\psi(t)\sqrt{\overline{V}_g^2 - \dot{N}^2(t)\cos^2\psi(t)} - \dot{N}(t)\cos 2\psi(t)\right]\right\} \tag{D.3.10}$$

The second derivative of $\psi(t)$ is,

$$\begin{aligned} \ddot{\psi}(t) &= \frac{d}{dt}\left[\frac{\dot{N}(t)\sin\psi(t) - \sqrt{\overline{V}_g^2 - \dot{N}^2(t)\cos^2\psi(t)}}{R}\right] \\ &= \frac{1}{R}\left[\dot{N}(t)\dot{\psi}(t)\cos\psi(t) - \frac{\dot{N}^2(t)\dot{\psi}(t)\cos\psi(t)\sin\psi(t)}{\sqrt{\overline{V}_g^2 - \dot{N}^2(t)\cos^2\psi(t)}}\right] \\ &= \frac{\dot{N}(t)\dot{\psi}(t)\cos\psi(t)}{R}\left[1 - \frac{\dot{N}^2(t)\sin\psi(t)}{\sqrt{\overline{V}_g^2 - \dot{N}^2(t)\cos^2\psi(t)}}\right] \end{aligned} \tag{D.3.11}$$

Bibliography

[1] M.V. Cook, *Flight Dynamics Principles*. Elsevier Butterworth-Heinemann, 1997.

[2] J.H. Blakelock, *Automatic Control of Aircraft and Missiles, 2nd ed*. Wiley-Interscience, 1991.

[3] M.C. Koen, *Modelling and Simulation of an RPV for Flight Control System Design Purposes*. University of Pretoria, 2006.

[4] G.F. Franklin, J.D. Powell, A. Emami-Naeini, *Feedback Control of Dynamic Systems, 4th ed*. Pearson Educational International, 2002.

[5] Hans B. Pacejka, *Tire and Vehicle Dynamics*, Society of Automotive Engineers, 2002.

[6] John C. Dixon, *Tires, Suspension and Handling, 2nd ed*, Society of Automotive Engineers, 1996.

[7] J. Y. Wong, *Theory of Ground Vehicles*, John Wiley & Sons, 1978.

[8] J. Diebel, *Representing Attitude: Euler Angles, Unit Quaternions and Rotation Vector*. Stanford University, 2006.

[9] M. Drela, *AVL 3.14 User Primer*. MIT Aero & Astro, 2004.

[10] Jean-Jacuqes E. Slotine & Weiping Li, *Applied Nonlinear Control*, Prentice Hall, 1991.

[11] Jan-Cor Roos, *Autonomous Take-Off and Landing of a Fixed Wing Unmanned Aerial Vehicle*, University of Stellenbosch, 2006.

[12] Jan-Cor Roos and I.K. Peddle, *Autonomous take-off and landing of a low cost unmanned aerial vehicle*, University of Stellenbosch, 2007.

[13] I.K. Peddle, *Autonomous Flight of a Model Aircraft*, University of Stellenbosch, 2004.

[14] I.K. Peddle, *Acceleration Based Manoeuvre Flight Control System for Unmanned Aerial Vehicles*, University of Stellenbosch, 2007.

[15] I.K. Peddle, T. Jones, *Acceleration Based 3D Maneuver Flight Control System for UAVs: Strategy and Longitudinal Design*, Submitted to Automatica, January 2008.

[16] S. Park, *Avionics and Control System Development for Mid-Air Rendezvous of Two Unmanned Aerial Vehicles*, Massachusetts Institute OF Technology, 2004

[17] S.C. Kriel, *A Comparison of Control Systems for the Flight Transition of VTOL Unmanned Aerial Vehicles*, University of Stellenbosch, 2008.

[18] W. J. Hough, *Autonomous Aerobatic Flight of a Fixed Wing Unmanned Aerial Vehicle*, University of Stellenbosch 2007.

[19] D.R. Gaum, *Aggressive Flight Control Techniques for a Fixed-Wing Unmanned Aerial Vehicle*, University of Stellenbosch, March 2009.

[20] D.R. Gaum, *Longitudinal Autopilot for a Navion Aircraft*, University of Stellenbosch, October 2006.

[21] J. Venter, *Development of an experimental Tilt-Wing VTOL Unmanned Aerial Vehicle*, University of Stellenbosch, 2005.

[22] M.M. Basson, *Aircraft Dynamics Tutor Software Design*, University of Stellenbosch, 2007.

[23] M.C. Silberbauer, *Simulation Visualisation System*, Undergraduate Final Year Project, University of Stellenbosch, 2005.

[24] D. Blaauw, *Flight Control System for a Variable Stability Blended-Wing-Body Unmanned Aerial Vehicle*, Masters Dissertation, University of Stellenbosch, 2008.

[25] B. Visser, *The precision landing of an UAV*, Masters Dissertation, University of Stellenbosch, 2008.

[26] J. E. Wilson, *Hover control for a vertical take-off and landing vehicle*, Masters Dissertation, University of Stellenbosch, 2009.

[27] M. M. Basson, *Stall prevention control of fixed-wing unmanned aerial vehicles*, Masters Dissertation, University of Stellenbosch, 2010.

[28] NASA History web page, `http://history.nasa.gov/SP-367/appendc.htm`. 2006.

[29] Wikimedia Commons web page, `http://commons.wikimedia.org/wiki/Main_Page`. 2008. (a source of images)